https://lib.uliege.be https://matheo.uliege.be

Identification of pedestrian loads on a very flexible footbridge

Auteur : Cancelinha Da Costa, Veronica
Promoteur(s) : Denoel, Vincent
Faculté : Faculté des Sciences appliquées
Diplôme : Master en ingénieur civil des constructions, à finalité spécialisée en "civil engineering"
Année académique : 2020-2021
URI/URL : http://hdl.handle.net/2268.2/11528

Avertissement à l'attention des usagers :

Tous les documents placés en accès ouvert sur le site le site MatheO sont protégés par le droit d'auteur. Conformément aux principes énoncés par la "Budapest Open Access Initiative"(BOAI, 2002), l'utilisateur du site peut lire, télécharger, copier, transmettre, imprimer, chercher ou faire un lien vers le texte intégral de ces documents, les disséquer pour les indexer, s'en servir de données pour un logiciel, ou s'en servir à toute autre fin légale (ou prévue par la réglementation relative au droit d'auteur). Toute utilisation du document à des fins commerciales est strictement interdite.

Par ailleurs, l'utilisateur s'engage à respecter les droits moraux de l'auteur, principalement le droit à l'intégrité de l'oeuvre et le droit de paternité et ce dans toute utilisation que l'utilisateur entreprend. Ainsi, à titre d'exemple, lorsqu'il reproduira un document par extrait ou dans son intégralité, l'utilisateur citera de manière complète les sources telles que mentionnées ci-dessus. Toute utilisation non explicitement autorisée ci-avant (telle que par exemple, la modification du document ou son résumé) nécessite l'autorisation préalable et expresse des auteurs ou de leurs ayants droit.

FACULTÉ DES SCIENCES APPLIQUÉES
Ecole d'ingénieurs et d'informaticiens

University of Liège
Faculty of Applied Sciences

Identification of pedestrian loads on a very flexible footbridge

---

Thesis submitted in partial fulfillment of the requirements for the degree of Master in Civil Engineering

Supervisor
Vincent Denoël

Author
Veronica Cancelinha da Costa

Jury members
Vincent de Ville de Goyet
Olivier Brüls
Cédric Schwartz

Academic year 2020-2021

Acknowledgments

Je souhaite particulièrement remercier le professeur Vincent Denoël, le promoteur de ce travail de fin d'études de m'avoir proposé ce sujet très intéressant. Je le remercie également pour son aide tout le long de ce travail, ses explications, remarques et ses conseils.

Je remercie Monsieur Vincent de Ville de Goyet, le professeur Olivier Brüls et Monsieur Cédric Schartz d'avoir accepté de faire partie du jury, ainsi que pour les conseils qu'ils ont pu me donner lors de la présentation intermédiaire.

Vielen Dank an Herrn Norman Kratz vom Stadt-Land-plus GmbH, der sich die Zeit genommen hat, mehrere Fragen zur Hängeseilbrücke Geierlay zu beantworten.

I also thank Katrien Van Nimmen, who personally send me some of her journal papers.

Je souhaite remercier Armin Bosten, qui s'est pris le temps de relire en profondeur mon travail et de m'avoir motivée lors des moments moins faciles.

Je remercie également ma famille et amis, pour leur soutien tout le long de mes études et d'avoir toujours cru en moi.

Finalement, je tiens à remercier l'Université de Liège et en particulier la faculté des sciences appliquées, ainsi que tous les professeurs qui m'ont donné cours le long de mon parcours universitaire. Même si ce n'était pas toujours facile, je suis contente d'avoir achevé des études d'ingénieur civil des constructions.

Abstract

The pedestrian loading on civil engineering structures is usually determined by using equivalent load models or by directly measuring the imposed forces on a rigid floor. Direct measurements are however costly and often only feasible in the laboratory. Additionally, a pedestrian that moves on a flexible bridge tends to adapt to the bridge motion and the load models currently available are therefore no longer valid. The objective of this thesis is to use an inverse dynamic technique to identify the actual loading based on measured vibrations.

The acceleration measurements are carried out on the Geierlay footbridge in Germany. These are then analysed to determine the modal properties of the structure, such as the natural frequencies and the damping ratios.

A joint input-state estimation algorithm is used to identify the pedestrian load, knowing the output accelerations. Before applying this inverse force identification technique to the real-world example, it is validated by two academic test cases. The first one is a 7m long, simply-supported concrete slab, such as in K. Van Nimmen et al. 'Inverse identification of pedestrian-induced loads' (ISMA, 2016), where the modal properties are already given as well as the resulting modal load. The influence of different parameters is also analysed. The second example is the extension of the former, by using the Geierlays length and its modal properties.

The method is then applied to the Geierlay footbridge using the measured accelerations. Finally, the results are compared to existing load models with the goal to propose improvements.

Résumé

Les charges piétonnes sur les ouvrages du génie civil sont généralement déterminées en utilisant des modèles de chargement équivalents ou en mesurant directement les efforts imposés sur un sol rigide. Cependant, les mesures directes sont souvent coûteuses et uniquement réalisables en laboratoire. De plus, un piéton qui se déplace sur un pont flexible a tendance à s'adapter au mouvement du pont et les modèles de chargement actuellement disponibles ne sont donc plus valables. L'objectif de cette thèse est d'utiliser une méthode d'analyse dynamique inverse afin d'identifier les charges réelles en se basant sur des vibrations mesurées.

Les mesures d'accélération sont réalisées sur la passerelle Geierlay en Allemagne. Celles-ci sont ensuite analysées pour déterminer les propriétés modales de la structure, telles que les fréquences propres et l'amortissement.

Un algorithme appelé 'Joint input-estimation algorithm' est ensuite utilisé. Celui-ci permet d'identifier les états et l'entrée du système en connaissant les accélérations sortantes. Avant d'appliquer cette technique d'identification inverse à un exemple du monde réel, celle-ci est d'abord validée à travers deux cas tests. Pour le premier, il s'agit d'une dalle en béton sur deux appuis simples, qui fait 7m de long, comme celle dans K. Van Nimmen et al. «Inverse identification of pedestrian-induced loads» (ISMA, 2016), où les propriétés modales sont données, ainsi que la charge modale obtenue. L'influence de différents paramètres est également analysée. Le deuxième cas test est l'extension du premier, en utilisant la longueur du Geierlay et ses propriétés modales.

La méthode est ensuite appliquée à la passerelle Geierlay à partir des accélérations mesurées sur site. Enfin, les résultats sont comparés aux valeurs données par les modèles de chargement existants dans le but de proposer des améliorations.

Contents

Nomenclature

n_d	Number of outputs (equal to the sum of n_{dd}, n_{dv} and n_{da})
n_m	Number of modes taken into account
n_p	Number of forces
n_s	Number of system states (equal to $2n_m$)
$n_{d,a}$	Number of acceleration measurements
$n_{d,d}$	Number of displacement or strain measurements
$n_{d,v}$	Number of velocity measurements
n_{dof}	Number of degrees of freedom

$\ddot{\boldsymbol{q}}$	Acceleration vector in modal coordinates
$\ddot{\boldsymbol{u}}$	Acceleration vector in a nodal basis
$\dot{\boldsymbol{q}}$	Velocity vector in modal coordinates
$\dot{\boldsymbol{u}}$	Velocity vector in a nodal basis
$\boldsymbol{\Gamma}$	Matrix containing the terms '$2\xi_i\omega_i$' corresponding to mode i on its diagonal (of dimensions n_m by n_m for a reduced order model)
$\boldsymbol{\Omega}$	Matrix containing the natural frequency ω_i corresponding to mode i on its diagonal (of dimensions n_m by n_m for a reduced order model)
$\boldsymbol{\omega}_i$	Natural frequency corresponding to mode i
$\boldsymbol{\Phi}$	Matrix containing the mode shapes $\boldsymbol{\varphi}_i$ corresponding to mode i as columns (of dimensions n_{dof} by n_m)
$\boldsymbol{\xi}_i$	Damping ratio corresponding to mode i
$\boldsymbol{q}$	Displacement vector in modal coordinates
$\boldsymbol{u}$	Displacement vector in a nodal basis
$\hat{\mathbf{p}}$	Input/forces vector estimate (of length n_p)

$\hat{\mathbf{x}}$	State vector estimate (of length n_s)
$\tilde{\mathbf{p}}$	Input/forces vector error (of length n_p)
$\tilde{\mathbf{x}}$	State vector error (of length n_s)
$\mathbf{A}$	State matrix (of dimensions n_s by n_s)
$\mathbf{B}$	Input matrix (of dimensions n_s by n_p)
$\mathbf{C}$	Damping matrix
$\mathbf{C}^*$	Generalized damping matrix (equal to $\mathbf{\Phi}^T\mathbf{C}\mathbf{\Phi}$ or $\mathbf{M}^*\mathbf{\Omega}^2$)
$\mathbf{d}$	Measurement/output vector (of length n_d)
$\mathbf{G}$	Measurement/output matrix (of dimensions n_d by n_s)
$\mathbf{I}$	Identity matrix
$\mathbf{J}$	Feedthrough matrix (of dimensions n_d by n_p)
$\mathbf{K}$	Stiffness matrix
$\mathbf{K}^*$	Generalized stiffness matrix (equal to $\mathbf{\Phi}^T\mathbf{K}\mathbf{\Phi}$ or $\mathbf{M}^*\mathbf{\Gamma}$)
$\mathbf{M}$	Mass matrix (of dimensions n_m by n_m for a reduced order model)
$\mathbf{M}^*$	Generalized mass matrix (of dimensions n_m by n_m for a reduced order model)
$\mathbf{P_p}$	Covariance matrix of the force error (of dimensions n_p by n_m)
$\mathbf{P_x}$	Covariance matrix of the state estimate error (of dimensions n_s by n_s)
$\mathbf{P_{xp}}$	Covariance matrix of the force and state estimate error (of dimensions n_s by n_m)
$\mathbf{p}$	Input/forces vector (of length n_p)
$\mathbf{Q}$	Covariance matrix of the process noise vector $\mathbf{w}$(of dimensions n_s by n_s)
$\mathbf{R}$	Covariance matrix of the measurement noise vector $\mathbf{v}$ (of dimensions n_d by n_d)
$\mathbf{S_a}$	Matrix relating the measured accelerations to the degrees of freedom of the model (of dimensions n_d by n_{dof})
$\mathbf{S_d}$	Matrix relating the measured displacement or strains to the degrees of freedom of the model (of dimensions n_d by n_{dof})
$\mathbf{S_v}$	Matrix relating the measured velocities to the degrees of freedom of the model (of dimensions n_d by n_{dof})
$\mathbf{S}$	Covariance matrix of the process and measurement noise vectors $\mathbf{w}$ and $\mathbf{v}$ (of dimensions n_s by n_d)
$\mathbf{v}$	Measurement noise vector (of length n_d)
$\mathbf{w}$	Process noise vector (of length n_s)
$\mathbf{x}$	State vector (of length n_s)

Specific to the joint input-state estimation algorithm

$\mathbf{K}$	Gain matrix (of dimensions n_s by n_d)

$\mathbf{M}$	Gain matrix (of dimensions n_m by n_d)
$\mathbf{N}$	Gain matrix (of dimensions n_s by n_d)

Symbols

$\delta_{[k]}$	Kronecker delta (equal to 1 for k=0 and to 0 otherwise)
$\mathbb{E}$	Expectation operator

Abbreviations

CDF	Cumulative distribution function
DLF	Dynamical load factor
FFT	Fast Fourier transform
GRF	Ground reaction force
HPBWM	Half-power bandwidth method
MDOF	Multi-degree of freedom
MVUE	Minimum variance and unbiased estimator
ODE	Ordinary differential equation
PP	Peak picking
RMS	Root mean square
SDOF	Single-degree of freedom
SSI-COV	Covariance-driven stochastic subspace identification method

Introduction

For several years now, it has become a trend to build slender and elegant bridges with lighter materials. These are more likely to vibrate than other types of bridges. In particular, one may see the emergence of footbridges. These fulfil their main purpose of linking two points often separated by a stream or a valley but are only dedicated to pedestrians.

This work will mainly focus on very flexible footbridges, also called simple suspension bridges. These are made of various cables which follow the shape of a catenary arc. The earliest bridges were of this type but made out of vines or ropes. The most recent example is the new *516 Arouca* footbridge in Portugal, named according to its length and location. It opened on the 29th of April 2021, is suspended at 175m above the Paiva river and is currently the longest footbridge in the world. The footbridge that will be dealt with here, is the *Geierlay* in Germany. Which opened in October 2015 and was at the time the longest footbridge in the country with a span of 360m.

These footbridges are mainly subjected to wind and pedestrian loads. The latter one is well defined for a single pedestrian crossing a rigid footbridge. The load is considered periodic in time and is defined by a Fourier series. For a flexible one, however, the pedestrian tends to adapt to the bridge motion and the existing loading models may be no longer valid. When a group or crowd of pedestrians crosses the footbridge it is even more complicated, as some phenomena of synchronisation between the pedestrians or with the bridge may occur. Examples in the past already showed lateral synchronisation. These cause discomfort for pedestrians. Some research has been done on this topic, but it is far from being a solved problem.

To gain a better understanding of pedestrian loads, the most straightforward way, would be to directly measure them on the existing footbridges and analyse them. However, this is rather difficult, such methods exist but are often costly, not very accurate and only feasible in the laboratory. Luckily, it is well known that measuring accelerations is easy and accurate. By using a dynamic inverse technique it is possible to identify the loads from which the measured accelerations originated. One example is the joint input-state estimation algorithm, which is an extension of the well known Kalman filter and will be used in this work.

Thus, the purpose of this work is:

- to familiarise with an inverse force identification technique by analysing it on the basis of two simple test cases,
- to carry out an experimental campaign on site, in order to measure accelerations when

groups of pedestrian cross the footbridge, as well as identify its modal properties, i.e. natural frequencies and damping ratios,

- to identify the pedestrian loads by applying the inverse force identification technique to the real footbridge,
- and to compare the identified pedestrian loads to existing loading models to check if they are realistic or if they need to be improved.

This is a step towards a better understanding of loads due to a group or crowd of pedestrians and improving the design of footbridges.

This work has the following structure:

Chapter 1 introduces briefly existing pedestrian loads identification methods. These are classified into direct and indirect approaches and their applicability to flexible footbridges is discussed. The reasons why the joint input-state estimation algorithm is chosen in this work are also stated.

Chapter 2 presents the inverse force identification technique chosen for this work. Starting from the continuous-time equation of motion and the definition of the measurement data vector, a discrete-time state-space model is derived in the modal basis, which is more convenient for the study of vibrations. The system matrices, i.e. state matrix, input matrix, measurement/output matrix and the feedthrough matrix are also defined. Since a reverse method and a modally reduced-order system are used, some applicability conditions have to be verified. Thus a section is dedicated to a brief recall of these conditions.

Chapter 3 starts by describing the Geierlay footbridge which is chosen for the experimental campaign of this work. Since information about the exact geometry of the footbridge is missing, various assumptions need to be made. For a better understanding of the measurements, the observations and conditions on site, when these were carried out, are described. An example of one of the accelerations in the three directions is given and analysed. The accelerations are then used to extract the modal properties of the footbridge. The natural frequencies are identified by using the peak-picking method and the damping ratio by using the covariance-driven stochastic subspace identification method.

Chapter 4 is dedicated to the validation and analysis of the joint input-state estimation algorithm. This is done through two simple, one-dimensional test cases. The influence of various parameters is analysed. These include the number of measurement data taken into account, the sampling step, the influence of noise and the number of modes taken into account. By comparing both test cases, the influence of two ratios is noticed. These are the structure's period divided by the sampling step and the time necessary to cross the structure divided by its period. Since in the last chapter the algorithm is applied to the Geierlay footbridge and its modal properties are used, it is reasonable to quantify the impact on the identified modal forces due to an error on the natural frequency or damping ratio.

Finally, in chapter 5 the algorithm is applied to the Geierlay footbridge in order to identify the load corresponding to the groups of pedestrians crossing the footbridge at the instant of measurement. These are compared to the maximum values given by existing loading models which are recalled in the first section. Improvements based on the results of this work are then suggested.

Chapter 1

Existing pedestrian loads identification methods

Several studies and experiments aim to identify the loads produced by pedestrians in order to better understand and model them. There already exist several methods to identify pedestrians loads, that one may class into direct or indirect approaches. The literature review in [50] and [51] gives a fairly complete list of methods. Some of them and others are applied in various papers which are referred to in the text. In this first chapter, a summary of pedestrian loads identification techniques is given and their applicability to flexible footbridges is assessed.

1.1 Direct approaches

Some approaches allow the direct measurement of contact forces induced by a pedestrian's feet on the structure. These are also called the ground reaction forces (GRF). Early research in this area consisted in analysing a standing feet impression in a plaster or analysing a printed pressure foot image of a walking person by using an inked fabric and a layer of paper.

Later the first force plates were invented. An example is shown in figure 1 (b). These can be integrated into the floor. In order to increase the data acquisition, several force plates can be placed one after the other. However, force plates create motion constraints for the pedestrian, who has to target them. This may have an influence on the identified forces, as the person does not move naturally. In [14] a similar concept is used, but here a large instrumented force platform is installed. Thus several people are able to walk on it which allows the derivation of a model for loads induced by a group of pedestrians. In [23] a long instrumented platform with load cells at the supports is used to study the lateral forces created by a pedestrian on a rigid footbridge. This is important in the context of footbridges since these loads already caused some discomfort problems in the past. Due to the high weight of the platform, inertial effects are predominant over the variation in the pedestrian-induced lateral forces. Besides, by using load cells at the supports the identified forces may be influenced by vibrations of the structure.

Instrumented treadmills with force sensors are also often used to identify the GRF. They have a single belt or a double as in the example shown in figure 1 (c). These allow the measurement of a large number of step cycles and therefore the possibility to observe stride to stride variations. However, the treadmill imposes a walking velocity which influences human motion. Such equipment is used in [8] and [43]. By using a treadmill that moves laterally it is possible to study the pedestrian's response to that motion and to measure the induced lateral loads [23].

Another possibility to measure directly pedestrian loads is to use instrumented shoes with force sensors or pressure insoles. An example is shown in figure 1 (a). The force amplitudes are obtained by integrating the distributed pressure over the insole area, which decreases the precision. This method applied in [10] and [17], avoids any motion constraints for the pedestrian, unlike the previous two approaches.

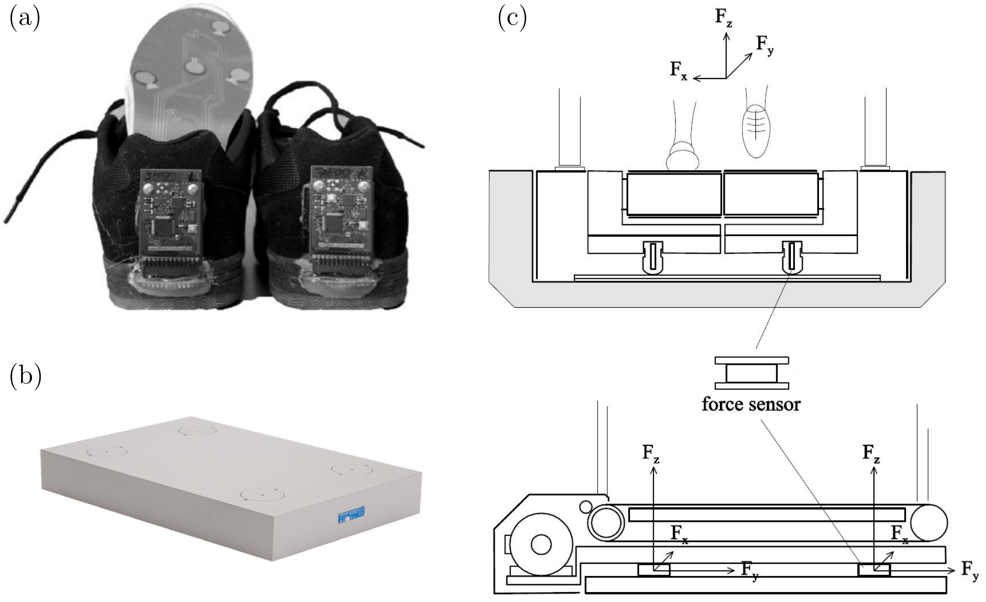

Figure 1: Examples of equipment for direct measurements of pedestrian load: instrumented shoes (a) [58], force plate (b) [28] and instrumented treadmill with force sensors (c) [51]

These direct measurement approaches are able to record the three pedestrian load components, i.e. in the vertical, longitudinal and lateral direction [1]. However, they have mostly been tested on rigid surfaces and the observations may slightly differ for a flexible footbridge. Except for the instrumented shoes, the force plates and instrumented treadmill should not be applied on a flexible surface. Since if the underlying floor vibrates, the measured forces are not simply equal to the GRF. There is an additional component which is the inertial force due to the mass of the force plate or treadmill. Additionally, these approaches are often only feasible in a laboratory and costly.

1.2 Indirect approaches

Among the indirect approaches, there is three-dimensional body motion tracking, which can be optical or non-optical. By assuming a distribution of the body mass and based on the Newton's second law of motion, the pedestrian induced load can be identified. The optical motion tracking is done with a marker-based optoelectronic system. If passive markers are

---

[1] More details about single pedestrian induced GRF are given in the first section of chapter 4.

used, infrared LED's illuminate the markers and the reflections are then recorded by several cameras. If active markers are used, they are self-illuminated, an example of equipment based on active markers is shown in figure 2. The optical motion tracking with markers can however only be done in a laboratory or another closed environment. It is also possible to analyse human motion simply by using a camera without any markers. However, this method is much more complicated and more elaborate software is needed for the post-processing. The non-optical three-dimensional motion tracking is based on inertial sensors, as for example the Xsens sensors, shown in figure 2 and which are used in [43]. The advantage of this latter technique is the possibility to use them outside on real structures like footbridges for example.

Figure 2: Examples of equipment used for indirect measurements (left: CODA gait analysis system based on active markers [58]/ right: Inertial Xsens sensors [40])

Other indirect approaches involve solving an inverse problem. From a recorded vibrational response of a structure, i.e. accelerations, velocities and/or displacements time histories, these are able to identify the pedestrian loads that were applied on a structure during the measurements. The main advantage of these methods is that the vibrational response of a structure can easily be recorded and with high precision. The difficulty is to find an adequate inversion technique. Several have already been suggested one may distinguish between methods applied in the frequency domain or in the time domain. One example of an inverse technique in the frequency domain is given in [60], which is able to identify the forces from measured stresses or strains. A method in the time domain is the gradient-based optimization algorithm presented in [16]. This method seeks to find the optimal time-dependent force that minimises the difference between simulated and measured accelerations and displacements, by knowing the coordinates of the applied force at each time step. Another, is the joint-input state estimation algorithm, which is based on a recursive three-step filter. It is able to identify the external loads and only requires the vibrational response of the structure. It has already been tested on several rigid footbridges as in [32], [33] and [35].

The indirect approaches have the advantage to impose no constraints on human motion. However, the optical three-dimensional body motion tracking can only be used under certain light conditions and thus can not be used on real footbridges, which is of interest here. The non-optical technique on the other hand, in addition to being cheaper, can be used anywhere. Just like the inverse techniques, which are based on the knowledge of the accurately measurable vibrational response of the structure. These approaches need a software or algorithm to post-process the measurements, this is why they are called indirect. The accuracy of the identified GRF depends thus on the accuracy of the measurement equipment and the post-processing technique. As the vibrational response can be measured the most precisely relative to the cost, this work will concentrate on an inverse technique. The joint-input state estimation algorithm is a robust method that works well even in presence of noise, which is important when working on measurements taken on real-world structures. This is not always the case for other methods like the gradient-based optimization algorithm. Therefore, it is the method of choice in this work and it will be applied to the flexible Geierlay footbridge.

Chapter 2

Joint input-state estimation algorithm

The joint input-state estimation algorithm is an inverse force identification technique. By knowing the vibrational response of the structure, it enables one to estimate recursively the pedestrian loads at the origin and the states. The developments done in section 2.1 to obtain the expressions of the system matrices are based on [32] and on the theory of dynamic analysis [6]. The algorithm is given in [44]. More details may be found in [19] and [34].

2.1 Definition of the system matrices

The vibrational response of any structure can be described by a differential equation, called the equation of motion. For a multi-degree of freedom (MDOF) and linear system with an external excitation $\mathbf{p}(t)$, the continuous-time governing equation discretized in space is given by:

$$\mathbf{M}\ddot{\boldsymbol{u}}(t) + \mathbf{C}\dot{\boldsymbol{u}}(t) + \mathbf{K}\boldsymbol{u}(t) = \mathbf{p}(t) \tag{2.1}$$

where $\mathbf{M}$, $\mathbf{C}$ and $\mathbf{K}$ are the mass matrix, the damping matrix and the stiffness matrix respectively. $\boldsymbol{u}(t)$ is the displacement vector. This equation describes the equilibrium between the inertia ($\mathbf{M}\ddot{\boldsymbol{u}}$), the dissipation ($\mathbf{C}\dot{\boldsymbol{u}}$), the potential energy ($\mathbf{K}\boldsymbol{u}$) and the external excitation $\mathbf{p}(t)$.

In order to see the system matrices appear, i.e. state matrix, input matrix, measurement/output matrix and the feedthrough matrix, a continuous-time state-space model is deduced from equation (2.1) and the definition of the measurement data vector given below. After passing to modal coordinates, the system is discretized in time, since it is this form that is interesting here.

2.1.1 Continuous-time state-space model

The continuous-time state-space form of the equation of motion is developed by introducing the state vector:

$$\mathbf{z}(\mathbf{t}) = \begin{pmatrix} \boldsymbol{u}(t) \\ \dot{\boldsymbol{u}}(t) \end{pmatrix} \tag{2.2}$$

and the trivial identity $\mathbf{M}\dot{\boldsymbol{u}} - \mathbf{M}\dot{\boldsymbol{u}} = \mathbf{0}$, so that equation (2.1) becomes:

$$\underbrace{\begin{pmatrix}\dot{\boldsymbol{u}}(t)\\ \ddot{\boldsymbol{u}}(t)\end{pmatrix}}_{\dot{\mathbf{z}}(t)} = \underbrace{\begin{bmatrix}\mathbf{0} & \mathbf{I}\\ -\mathbf{M}^{-1}\mathbf{K} & -\mathbf{M}^{-1}\mathbf{C}\end{bmatrix}}_{\mathbf{A_{c,n}}}\underbrace{\begin{pmatrix}\boldsymbol{u}(t)\\ \dot{\boldsymbol{u}}(t)\end{pmatrix}}_{\mathbf{z}(t)} + \underbrace{\begin{bmatrix}\mathbf{0}\\ \mathbf{M}^{-1}\end{bmatrix}}_{\mathbf{B_{c,n}}}\mathbf{p}(t) \tag{2.3}$$

Where $\mathbf{A_{c,n}}$ and $\mathbf{B_{c,n}}$ are two system matrices.

The model is completed by a second state-space equation established from the definition of the measurement data vector $\mathbf{d}(t)$. Which is defined as a linear combination of the displacement, velocity and acceleration vectors, such as:

$$\mathbf{d}(t) = \mathbf{S_a}\ddot{\boldsymbol{u}}(t) + \mathbf{S_v}\dot{\boldsymbol{u}}(t) + \mathbf{S_d}\boldsymbol{u}(t) \tag{2.4}$$

Where, $\mathbf{S_a}$, $\mathbf{S_v}$ and $\mathbf{S_d}$ are selection matrices.

The state-space form of equation (2.4) is given by using the equation of motion (2.1) and introducing the state vector:

$$\begin{aligned}\boldsymbol{d}(t) &= \mathbf{S_a}\left(-\mathbf{M^{-1}C}\dot{\boldsymbol{u}}(t) - \mathbf{M^{-1}K}\boldsymbol{u}(t) + \mathbf{M^{-1}p}(t)\right) + \mathbf{S_v}\dot{\boldsymbol{u}}(t) + \mathbf{S_d}\boldsymbol{u}(t)\\ &= \underbrace{\begin{bmatrix}\mathbf{S_d} - \mathbf{S_a M^{-1}K} & \mathbf{S_v} - \mathbf{S_a M^{-1}C}\end{bmatrix}}_{\mathbf{G_{c,n}}}\underbrace{\begin{pmatrix}\boldsymbol{u}(t)\\ \dot{\boldsymbol{u}}(t)\end{pmatrix}}_{\mathbf{z}(t)} + \underbrace{\begin{bmatrix}\mathbf{S_a M^{-1}}\end{bmatrix}}_{\mathbf{J_{c,n}}}\mathbf{p}(t)\end{aligned} \tag{2.5}$$

Together, equations (2.3) and (2.5) form the continuous-time state-space model for a full order system:

$$\boxed{\begin{aligned}\dot{\mathbf{z}}(t) &= \mathbf{A_{c,n}}\mathbf{z}(t) + \mathbf{B_{c,n}}\mathbf{p}(t)\\ \mathbf{d}(t) &= \mathbf{G_{c,n}}\mathbf{z}(t) + \mathbf{J_{c,n}}\mathbf{p}(t)\end{aligned}}$$

2.1.2 In modal coordinates

A modal analysis is more convenient for the study of vibrations. As it allows reducing the number of unknowns and decoupling the MDOF system into independent single-degree of freedom (SDOF) differential equations of motion. The change to modal coordinates is done by the following coordinate transformation:

$$\boldsymbol{u}(t) = \mathbf{\Phi}\mathbf{q}(t) \tag{2.6}$$

Where, $\mathbf{q}(t)$ is the vector of modal coordinates and $\mathbf{\Phi}$ contains the mode shapes as columns, which are normalized to a unit maximum absolute value, such that for mode i at the degree of freedom j:

$$\max_j |\Phi_{ji}| = 1$$

This is different from the definition used in the scientific papers [19] [34] [44], where mass normalized mode shapes are used.

Transforming the state vector accordingly yields:

$$\mathbf{z}(t) = \begin{bmatrix}\mathbf{\Phi} & \mathbf{0}\\ \mathbf{0} & \mathbf{\Phi}\end{bmatrix}\mathbf{x}(t) \quad \text{with } \mathbf{x}(t) = \begin{pmatrix}\mathbf{q}(t)\\ \dot{\mathbf{q}}(t)\end{pmatrix} \tag{2.7}$$

Consequently, by introducing (2.7) into (2.3):

$$\begin{bmatrix} \mathbf{\Phi} & \mathbf{0} \\ \mathbf{0} & \mathbf{\Phi} \end{bmatrix} \begin{pmatrix} \dot{\mathbf{q}}(t) \\ \ddot{\mathbf{q}}(t) \end{pmatrix} = \begin{bmatrix} \mathbf{0} & \mathbf{I} \\ -\mathbf{M}^{-1}\mathbf{K} & -\mathbf{M}^{-1}\mathbf{C} \end{bmatrix} \begin{bmatrix} \mathbf{\Phi} & \mathbf{0} \\ \mathbf{0} & \mathbf{\Phi} \end{bmatrix} \begin{pmatrix} \mathbf{q}(t) \\ \dot{\mathbf{q}}(t) \end{pmatrix} + \begin{bmatrix} \mathbf{0} \\ \mathbf{M}^{-1} \end{bmatrix} \mathbf{p}(t) \tag{2.8}$$

Equation (2.8) is now projected into the modal basis by left multiplication with $\begin{bmatrix} \mathbf{\Phi} & \mathbf{0} \\ \mathbf{0} & \mathbf{\Phi} \end{bmatrix}^T \mathbf{M}$. The left-hand side becomes

$$\begin{bmatrix} \mathbf{\Phi} & \mathbf{0} \\ \mathbf{0} & \mathbf{\Phi} \end{bmatrix}^T \mathbf{M} \begin{bmatrix} \mathbf{\Phi} & \mathbf{0} \\ \mathbf{0} & \mathbf{\Phi} \end{bmatrix} \begin{pmatrix} \dot{\mathbf{q}}(t) \\ \ddot{\mathbf{q}}(t) \end{pmatrix} = \begin{bmatrix} \mathbf{M}^* & \mathbf{0} \\ \mathbf{0} & \mathbf{M}^* \end{bmatrix} \dot{\mathbf{x}}(t) \tag{2.9}$$

where the generalized mass matrix is defined as $\mathbf{M}^* = \mathbf{\Phi}^T\mathbf{M}\mathbf{\Phi}$ which is diagonal. The time derivative of the state vector is then isolated, which yields the following equation

$$\dot{\mathbf{x}}(t) = \mathbf{A_c}\mathbf{x}(t) + \mathbf{B_c}\mathbf{p}^*(t) \tag{2.10}$$

where the system matrix $\mathbf{A}_c$ is obtained as

$$\begin{aligned} \mathbf{A}_c &= \begin{bmatrix} \mathbf{M}^* & \mathbf{0} \\ \mathbf{0} & \mathbf{M}^* \end{bmatrix}^{-1} \begin{bmatrix} \mathbf{\Phi} & \mathbf{0} \\ \mathbf{0} & \mathbf{\Phi} \end{bmatrix}^T \mathbf{M} \begin{bmatrix} \mathbf{0} & \mathbf{I} \\ -\mathbf{M}^{-1}\mathbf{K} & -\mathbf{M}^{-1}\mathbf{C} \end{bmatrix} \begin{bmatrix} \mathbf{\Phi} & \mathbf{0} \\ \mathbf{0} & \mathbf{\Phi} \end{bmatrix} \\ &= \begin{bmatrix} \mathbf{0} & \mathbf{M}^{*-1}\mathbf{\Phi}^T\mathbf{M}\mathbf{\Phi} \\ -\mathbf{M}^{*-1}\mathbf{\Phi}^T\mathbf{K}\mathbf{\Phi} & -\mathbf{M}^{*-1}\mathbf{\Phi}^T\mathbf{C}\mathbf{\Phi} \end{bmatrix} \\ &= \begin{bmatrix} \mathbf{0} & \mathbf{I} \\ -\mathbf{M}^{*-1}\mathbf{K}^* & -\mathbf{M}^{*-1}\mathbf{C}^* \end{bmatrix} \\ &= \begin{bmatrix} \mathbf{0} & \mathbf{I} \\ -\mathbf{\Omega}^2 & -\mathbf{\Gamma} \end{bmatrix} \end{aligned} \tag{2.11}$$

In (2.11) the generalized stiffness matrix $\mathbf{K}^* = \mathbf{\Phi}^T\mathbf{K}\mathbf{\Phi}$ is defined, which is diagonal. The generalized damping matrix $\mathbf{C}^* = \mathbf{\Phi}^T\mathbf{C}\mathbf{\Phi}$ is also assumed diagonal.

Moreover, the stiffness and damping matrices are related to the generalized mass matrix and the modal properties of the structure through $\mathbf{K}^* = \mathbf{M}^*\mathbf{\Omega}^2$ and $\mathbf{C}^* = \mathbf{M}^*\mathbf{\Gamma}$. The matrix $\mathbf{\Omega}$ contains the natural frequencies ω_i on its diagonal and $\mathbf{\Gamma}$ contains the terms '$2\xi_i\omega_i$' on its diagonal, where ξ_i is the damping ratio related to mode i. The three matrices $\mathbf{M}^*$, $\mathbf{C}^*$ and $\mathbf{K}^*$ contain the structural properties expressed in the basis of the normal modes.

The term related to external excitation takes the form

$$\begin{aligned} &\begin{bmatrix} \mathbf{M}^* & \mathbf{0} \\ \mathbf{0} & \mathbf{M}^* \end{bmatrix}^{-1} \begin{bmatrix} \mathbf{\Phi} & \mathbf{0} \\ \mathbf{0} & \mathbf{\Phi} \end{bmatrix}^T \mathbf{M} \begin{bmatrix} \mathbf{0} \\ \mathbf{M}^{-1} \end{bmatrix} \mathbf{p}(t) \\ &= \begin{bmatrix} \mathbf{0} \\ \mathbf{M}^{*-1}\mathbf{\Phi}^T\mathbf{M}\mathbf{M}^{-1} \end{bmatrix} \mathbf{p}(t) = \begin{bmatrix} \mathbf{0} \\ \mathbf{M}^{*-1} \end{bmatrix} \mathbf{\Phi}^T\mathbf{p}(t) = \mathbf{B_c}\mathbf{p}^*(t) \end{aligned} \tag{2.12}$$

where $\mathbf{p}^*(t) = \mathbf{\Phi}^T\mathbf{p}(t)$ represent the generalized forces.

The same coordinate transformation can be done for the measurement data vector:

$$\begin{aligned}\mathbf{d}(t) &= \begin{bmatrix}\mathbf{S_d} - \mathbf{S_a M^{-1} K} & \mathbf{S_v} - \mathbf{S_a M^{-1} C}\end{bmatrix} \begin{pmatrix}\boldsymbol{u}(t) \\ \dot{\boldsymbol{u}}(t)\end{pmatrix} + \begin{bmatrix}\mathbf{S_a M^{-1}}\end{bmatrix} \mathbf{p}(t) \\ &= \underbrace{\begin{bmatrix}\mathbf{S_d} - \mathbf{S_a M^{-1} K} & \mathbf{S_v} - \mathbf{S_a M^{-1} C}\end{bmatrix} \begin{bmatrix}\boldsymbol{\Phi} & \mathbf{0} \\ \mathbf{0} & \boldsymbol{\Phi}\end{bmatrix}}_{i} \begin{pmatrix}\boldsymbol{z}(t) \\ \dot{\boldsymbol{z}}(t)\end{pmatrix} + \underbrace{\begin{bmatrix}\mathbf{S_a M^{-1}}\end{bmatrix} \mathbf{p}(t)}_{ii} \end{aligned} \tag{2.13}$$

Where inverse mass matrix is evaluated as

$$\begin{aligned}\boldsymbol{\Phi}^{\boldsymbol{T}}\mathbf{M}\boldsymbol{\Phi} &= \mathbf{M}^{*} \\ \boldsymbol{\Phi}\boldsymbol{\Phi}^{\boldsymbol{T}}\mathbf{M}\boldsymbol{\Phi}\boldsymbol{\Phi}^{\boldsymbol{T}} &= \boldsymbol{\Phi}\mathbf{M}^{*}\boldsymbol{\Phi}^{\boldsymbol{T}} \\ \mathbf{M} &= \left(\boldsymbol{\Phi}\boldsymbol{\Phi}^{\boldsymbol{T}}\right)^{-1} \boldsymbol{\Phi}\mathbf{M}^{*}\boldsymbol{\Phi}^{\boldsymbol{T}} \left(\boldsymbol{\Phi}\boldsymbol{\Phi}^{\boldsymbol{T}}\right)^{-1} \\ \mathbf{M}^{-1} &= \boldsymbol{\Phi}\boldsymbol{\Phi}^{\boldsymbol{T}} \left(\boldsymbol{\Phi}\mathbf{M}^{*}\boldsymbol{\Phi}^{\boldsymbol{T}}\right)^{-1} \boldsymbol{\Phi}\boldsymbol{\Phi}^{\boldsymbol{T}}\end{aligned}$$

In order to simplify this expression, it is temporary assumed that all modes are taken into account, such that:

$$\begin{aligned}\mathbf{M}^{-1} &= \boldsymbol{\Phi}\boldsymbol{\Phi}^{\boldsymbol{T}}\boldsymbol{\Phi}^{\boldsymbol{T}^{-1}}\mathbf{M}^{*^{-1}}\boldsymbol{\Phi}^{-1}\boldsymbol{\Phi}\boldsymbol{\Phi}^{\boldsymbol{T}} \\ &= \boldsymbol{\Phi}\mathbf{M}^{*^{-1}}\boldsymbol{\Phi}^{\boldsymbol{T}}\end{aligned}$$

The two terms on the right hand side in (2.13) become:
(i)

$$\begin{aligned}&\begin{bmatrix}\mathbf{S_d} - \mathbf{S_a M^{-1} K} & \mathbf{S_v} - \mathbf{S_a M^{-1} C}\end{bmatrix} \begin{bmatrix}\boldsymbol{\Phi} & \mathbf{0} \\ \mathbf{0} & \boldsymbol{\Phi}\end{bmatrix} \\ &= \begin{bmatrix}\mathbf{S_d}\boldsymbol{\Phi} - \mathbf{S_a}\boldsymbol{\Phi}\mathbf{M}^{*^{-1}}\boldsymbol{\Phi}^{\boldsymbol{T}}\mathbf{K}\boldsymbol{\Phi} & \mathbf{S_v}\boldsymbol{\Phi} - \mathbf{S_a}\boldsymbol{\Phi}\mathbf{M}^{*^{-1}}\boldsymbol{\Phi}^{\boldsymbol{T}}\mathbf{C}\boldsymbol{\Phi}\end{bmatrix} \\ &= \begin{bmatrix}\mathbf{S_d}\boldsymbol{\Phi} - \mathbf{S_a}\boldsymbol{\Phi}\mathbf{M}^{*^{-1}}\mathbf{K}^{*} & \mathbf{S_v}\boldsymbol{\Phi} - \mathbf{S_a}\boldsymbol{\Phi}\mathbf{M}^{*^{-1}}\mathbf{C}^{*}\end{bmatrix} \\ &= \begin{bmatrix}\mathbf{S_d}\boldsymbol{\Phi} - \mathbf{S_a}\boldsymbol{\Phi}\mathbf{M}^{*^{-1}}\mathbf{M}^{*}\boldsymbol{\Omega}^{2} & \mathbf{S_v}\boldsymbol{\Phi} - \mathbf{S_a}\boldsymbol{\Phi}\mathbf{M}^{*^{-1}}\mathbf{M}^{*}\boldsymbol{\Gamma}\end{bmatrix} \\ &= \begin{bmatrix}\mathbf{S_d}\boldsymbol{\Phi} - \mathbf{S_a}\boldsymbol{\Phi}\boldsymbol{\Omega}^{2} & \mathbf{S_v}\boldsymbol{\Phi} - \mathbf{S_a}\boldsymbol{\Phi}\boldsymbol{\Gamma}\end{bmatrix} \\ &= \mathbf{G_c}\end{aligned}$$

(ii)

$$\begin{bmatrix}\mathbf{S_a M^{-1}}\end{bmatrix} \mathbf{p}(t) = \begin{bmatrix}\mathbf{S_a}\boldsymbol{\Phi}\mathbf{M}^{*^{-1}}\boldsymbol{\Phi}^{\boldsymbol{T}}\end{bmatrix} = \begin{bmatrix}\mathbf{S_a}\boldsymbol{\Phi}\mathbf{M}^{*^{-1}}\end{bmatrix} \boldsymbol{\Phi}^{\boldsymbol{T}}\mathbf{p}(t) = \mathbf{J_c}\mathbf{p}^{*}(t)$$

Thus the data vector writes

$$\boldsymbol{d}(t) = \mathbf{G_c}\mathbf{x}(t) + \mathbf{J_c}\mathbf{p}^{*}(t) \tag{2.14}$$

Equations (2.10) and (2.14) form the continuous-time state-space model with modal coordinates:

$$\boxed{\begin{aligned}\dot{\mathbf{x}}(t) &= \mathbf{A_c}\mathbf{x}(t) + \mathbf{B_c}\mathbf{p}^{*}(t) \\ \boldsymbol{d}(t) &= \mathbf{G_c}\mathbf{x}(t) + \mathbf{J_c}\mathbf{p}^{*}(t)\end{aligned}}$$

2.1.3 Discretization

The last step is to discretize in time the previous state-space models, as it is this form that is used in the algorithm. The sampling rate is taken equal to $\frac{1}{\Delta t}$. Equation (2.10),

$$\dot{\mathbf{x}}(t) - \mathbf{A_c}\mathbf{x}(t) = \mathbf{B_c}\mathbf{p}^*(t)$$

is a linear, first order and non-homogeneous ordinary differential equation (ODE).

One way to discretize this ODE, for $k\Delta t \leq t \leq (k+1)\Delta t$ is to first multiply both sides by $e^{-\mathbf{A_c}t}$, which gives:

$$\int_{k\Delta t}^{(k+1)\Delta t} d(e^{-\mathbf{A_c}t}\mathbf{x}) = \int_{k\Delta t}^{(k+1)\Delta t} e^{-\mathbf{A_c}t}\mathbf{B_c}\mathbf{p}^*(k)dt$$

The left hand side integral can easily be calculated and if both sides are multiplied by $e^{\mathbf{A_c}(k+1)\Delta t}$, the equation becomes:

$$\begin{aligned} e^{-\mathbf{A_c}(k+1)\Delta t}\mathbf{x}(k+1) - e^{-\mathbf{A_c}k\Delta t}\mathbf{x}(k) &= \int_{k\Delta t}^{(k+1)\Delta t} e^{\mathbf{A_c}t}\mathbf{B_c}\mathbf{p}^*(k)dt \\ \mathbf{x}(k+1) - e^{-\mathbf{A_c}k\Delta t}\mathbf{x}(k) &= \int_{k\Delta t}^{(k+1)\Delta t} exp[\mathbf{A_c}((k+1)\Delta t - t)]\mathbf{B_c}\mathbf{p}^*(k)dt \end{aligned}$$

To simplify the right hand side, let us now define τ such that $\tau = (k+1)\Delta t - t$, thus $d\tau = -dt$ and the integration boundaries change into $\tau = \Delta t$ and $\tau = 0$. Consequently,

$$\int_{\Delta t}^{0} exp[\mathbf{A_c}\tau]\mathbf{B_c}\mathbf{p}^*(k)(-d\tau) = \int_{0}^{\Delta t} exp[\mathbf{A_c}\tau]\mathbf{B_c}\mathbf{p}^*(k)d\tau$$

By inserting this in the previous equation, the system matrices can be defines as:

$$\mathbf{x}(k+1) = \underbrace{e^{-\mathbf{A_c}k\Delta t}}_{\mathbf{A}}\mathbf{x}(k) + \underbrace{\int_0^{\Delta t} \exp[\mathbf{A_c}\tau]\mathbf{B_c}d\tau}_{\mathbf{B}}\,\mathbf{p}^*(k)$$

Where,

$$\mathbf{B} = \int_0^{\Delta t} \exp[\mathbf{A_c}\tau]\mathbf{B_c}d\tau = e^{\mathbf{A_c}\Delta t}\mathbf{A_c}^{-1}\mathbf{B_c} - e^0\mathbf{A_c}^{-1}\mathbf{B_c} = [\mathbf{A} - \mathbf{I}]\mathbf{A_c}^{-1}\mathbf{B_c}$$

The discretization of the second equation of the model is trivial. Finally, the discrete-time state-space model is given by:

$$\boxed{\begin{aligned} \mathbf{x}_{[k+1]} &= \mathbf{A}\mathbf{x}_{[k]} + \mathbf{B}\mathbf{p}^*_{[k]} \\ \mathbf{d}_{[k]} &= \mathbf{G}\mathbf{x}_{[k]} + \mathbf{J}\mathbf{p}^*_{[k]} \end{aligned}}$$

In general, **A** is called the state matrix, **B** is the input matrix, **G** is the measurement/output matrix and **J** is the feedthrough matrix.

2.2 Consideration of noise

To take into account the noise, two terms can be added to the discrete-time state-space model found in section 2.1.3, which then gives:

$$\boxed{\begin{aligned} \mathbf{x}_{[k+1]} &= \mathbf{A}\mathbf{x}_{[k]} + \mathbf{B}\mathbf{p}^*_{[k]} + \mathbf{w}_{[k]} \\ \mathbf{d}_{[k]} &= \mathbf{G}\mathbf{x}_{[k]} + \mathbf{J}\mathbf{p}^*_{[k]} + \mathbf{v}_{[k]} \end{aligned}}$$

Where $\mathbf{w}_{[k]}$ is the process noise vector, it is the sum of the noise due to stochastic excitation and noise due to modelling errors. $\mathbf{v}_{[k]}$ is the measurement noise vector, it is defined as the sum of a contribution due to stochastic excitation, due to measurement errors and a contribution due to modelling errors. Both are assumed to be zero mean and white.

Their covariance matrices $\mathbf{Q}$, $\mathbf{R}$ and $\mathbf{S}$ are known and defined by:

$$\mathbb{E}\left[\begin{pmatrix} \mathbf{w}_{[k]} \\ \mathbf{v}_{[k]} \end{pmatrix} \begin{pmatrix} \mathbf{w}^T_{[l]} & \mathbf{v}^T_{[l]} \end{pmatrix}\right] = \begin{bmatrix} \mathbf{Q} & \mathbf{S} \\ \mathbf{S}^T & \mathbf{R} \end{bmatrix} \delta_{[k-l]} \tag{2.15}$$

Where, $\mathbf{R} > 0$ and $\begin{bmatrix} \mathbf{Q} & \mathbf{S} \\ \mathbf{S}^T & \mathbf{R} \end{bmatrix} \geq 0$.

2.3 The algorithm

The algorithm given in many scientific papers, such as [19] and [34], is divided into 3 steps:

Input estimation

$$\tilde{\mathbf{R}}_{[k]} = \mathbf{G}\mathbf{P}_{\mathrm{x}[k|k-1]}\mathbf{G}^{\mathrm{T}} + \mathbf{R} \tag{2.16}$$

$$\mathbf{M}_{[k]} = \left(\mathbf{J}^{\mathrm{T}}\tilde{\mathbf{R}}^{-1}_{[k]}\mathbf{J}\right)^{-1}\mathbf{J}^{\mathrm{T}}\tilde{\mathbf{R}}^{-1}_{[k]} \tag{2.17}$$

$$\hat{\mathbf{p}}_{[k|k]} = \mathbf{M}_{[k]}\left(\mathbf{d}_{[k]} - \mathbf{G}\hat{\mathbf{x}}_{[k|k-1]}\right) \tag{2.18}$$

$$\mathbf{P}_{\mathrm{p}[k|k]} = \left(\mathbf{J}^{\mathrm{T}}\tilde{\mathbf{R}}^{-1}_{[k]}\mathbf{J}\right)^{-1} \tag{2.19}$$

Measurement update

$$\mathbf{K}_{[k]} = \mathbf{P}_{\mathrm{x}[k|k-1]}\mathbf{G}^{\mathrm{T}}\tilde{\mathbf{R}}^{-1}_{[k]} \tag{2.20}$$

$$\hat{\mathbf{x}}_{[k|k]} = \hat{\mathbf{x}}_{[k|k-1]} + \mathbf{K}_{[k]}\left(\mathbf{d}_{[k]} - \mathbf{G}\hat{\mathbf{x}}_{[k|k-1]} - \mathbf{J}\hat{\mathbf{p}}_{[k|k]}\right) \tag{2.21}$$

$$\mathbf{P}_{\mathrm{x}[k|k]} = \mathbf{P}_{\mathrm{x}[k|k-1]} - \mathbf{K}_{[k]}\left(\tilde{\mathbf{R}}_{[k]} - \mathbf{J}\mathbf{P}_{\mathrm{p}[k|k]}\mathbf{J}^{\mathrm{T}}\right)\mathbf{K}^{\mathrm{T}}_{[k]} \tag{2.22}$$

$$\mathbf{P}_{\mathrm{xp}[k|k]} = \mathbf{P}^{\mathrm{T}}_{\mathrm{px}[k|k]} = -\mathbf{K}_{[k]}\mathbf{J}\mathbf{P}_{\mathrm{p}[k|k]} \tag{2.23}$$

Time update

$$\hat{\mathbf{x}}_{[k+1|k]} = \mathbf{A}\hat{\mathbf{x}}_{[k|k]} + \mathbf{B}\hat{\mathbf{p}}_{[k|k]} \tag{2.24}$$

$$\mathbf{N}_{[k]} = \mathbf{A}\mathbf{K}_{[k]}\left(\mathbf{I}_{n_{\mathrm{d}}} - \mathbf{J}\mathbf{M}_{[k]}\right) + \mathbf{B}\mathbf{M}_{[k]} \tag{2.25}$$

$$\mathbf{P}_{\mathbf{x}[k+1|k]} = \begin{bmatrix} \mathbf{A} & \mathbf{B} \end{bmatrix} \begin{bmatrix} \mathbf{P}_{\mathbf{x}[k|k]} & \mathbf{P}_{\mathbf{xp}[k|k]} \\ \mathbf{P}_{\mathbf{px}[k|k]} & \mathbf{P}_{\mathbf{p}[k|k]} \end{bmatrix} \begin{bmatrix} \mathbf{A}^{\mathrm{T}} \\ \mathbf{B}^{\mathrm{T}} \end{bmatrix} + \mathbf{Q} - \mathbf{N}_{[k]}\mathbf{S}^{\mathrm{T}} - \mathbf{S}\mathbf{N}^{\mathrm{T}}_{[k]} \tag{2.26}$$

Where the system matrices appearing in the algorithm are defined by the following expressions:

$$\mathbf{A} = e^{\mathbf{A_c}\Delta t} = \exp\left(\begin{bmatrix} \mathbf{0} & \mathbf{I} \\ -\boldsymbol{\Omega}^2 & -\boldsymbol{\Gamma} \end{bmatrix} \Delta t\right) \tag{2.27}$$

$$\mathbf{B} = [\mathbf{A} - \mathbf{I}]\mathbf{A_c}^{-1}\mathbf{B_c} = \left[\exp\left(\begin{bmatrix} \mathbf{0} & \mathbf{I} \\ -\boldsymbol{\Omega}^2 & -\boldsymbol{\Gamma} \end{bmatrix} \Delta t\right) - \mathbf{I}\right] \begin{bmatrix} \mathbf{0} & \mathbf{I} \\ -\boldsymbol{\Omega}^2 & -\boldsymbol{\Gamma} \end{bmatrix}^{-1} \begin{bmatrix} \mathbf{0} \\ \mathbf{M}^{*-1} \end{bmatrix} \tag{2.28}$$

$$\mathbf{G} = \mathbf{G_c} = \left[\mathbf{S_d}\boldsymbol{\Phi} - \mathbf{S_a}\boldsymbol{\Phi}\boldsymbol{\Omega}^2 \quad \mathbf{S_v}\boldsymbol{\Phi} - \mathbf{S_a}\boldsymbol{\Phi}\boldsymbol{\Gamma}\right] \tag{2.29}$$

$$\mathbf{J} = \mathbf{J_c} = \left[\mathbf{S_a}\boldsymbol{\Phi}\mathbf{M}^{*-1}\right] \tag{2.30}$$

Notice the similarity with the well known Kalman filter for the measurement and time update, which is underlined in [19]. The main difference is that the state estimate is based on an optimal estimate for the input and no more its exact value. Plus, if $\mathbf{B} = \mathbf{0}$ and $\mathbf{J} = \mathbf{0}$, then the Kalman filter is obtained. For a deeper understanding of the algorithm, its formulation is detailed in Appendix A.

2.4 Applicability conditions

As for any inverse technique and especially an instantaneous system inversion as in the case of the joint input-state estimation algorithm presented in this chapter, some conditions must be met to assure the invertibility. In [33] these are given by the following:

- Identifiability: In order to be able to identify the wanted forces and states, the measurements must contain sufficient information.
- Stability: The algorithm must be stable to avoid completely false results following a small perturbation of the data.
- Uniqueness: The results of the algorithm, i.e. the input forces and states must be unique.

These are briefly specified in what follows for the case of a linear and a modally reduced-order system. Here and generally in structural dynamics, often only the n_m first modes of the structure are taken into account for simplicity. For more information about the applicability conditions, the reader may refer to [32] and [33].

Identifiability

The first condition is respected if the following three requirements are fulfilled. First, the observability of the system, which asks that, if n_m modes are taken into account, they must have been excited when taking measurements ie. information about them must have been captured in the measurements. Additionally, the sensors can not be placed at the nodes of this mode. A necessary and sufficient condition for the system to be observable is that the matrix $(\mathbf{S_d} + \mathbf{S_v} + \mathbf{S_a})\boldsymbol{\Phi}$ has no zero columns.

A second requirement is the controllability of the system, which is assured if $\mathbf{S_p}^T\mathbf{\Phi}$ has no zero columns, where $\mathbf{S_p}$ is a matrix containing the locations of the applied forces.

Finally, the third requirement is the direct invertibility of the system, which is respected if and only if rank($\mathbf{J}$)=n_p, where n_p is the number of forces to be identified with $n_p \leq n_{d,a}$, $n_{d,a}$ being the number of acceleration measurements. For a modally reduced model, this requirement extends to rank($\mathbf{J}$)=min($n_{d,a}, n_p, n_m$) and an additional condition $n_p \leq n_m$ is added.

Stability

To assure the stability of the system, it can not have any unstable or marginally unstable transmission zeros. These zeros are complex numbers for which a non zero input gives a zero output. The finite transmission zeros correspond to the roots of the numerator of the corresponding transfer function, which for a state-space system is given by [31]: $\mathbf{H}(s) = \mathbf{G}(s\mathbf{I} - \mathbf{A})^{-1}\mathbf{B} + \mathbf{J}$. The transmission zeros are considered stable if they are located inside the unit circle in the z-domain or equivalently if located in the left half plane of the Laplace domain. As shown in figure 3. They are marginally stable if they are on the unit circle or the vertical axis and unstable if they are outside the unit circle or on the right half plane.

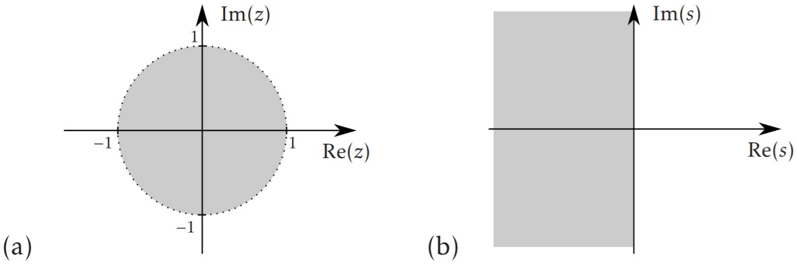

Figure 3: Stability regions in grey in the z-domain (a) and the Laplace domain (b) [34]

This is verified, if there is at least one displacement/strain measurement, such that rank($\mathbf{J} - \mathbf{G}(\mathbf{A} - \mathbf{I})^{-1}\mathbf{B}$)=min($n_p$,$n_d$). This is the case if $n_p \leq n_{d,d}$, where n_d is the total number of measurements and $n_{d,d}$ is the number of displacement/strain measurements. This is because acceleration and/or velocity measurements are insensitive to a constant excitation and do not enable the identification of the static component of the input forces and states of the system. It will be shown in chapter 4, when validating and analysing the joint input-state estimation algorithm.

Uniqueness

To assure a unique identification of the forces and states of the system it should not have any finite transmission zeros.

Chapter 3

Experimental data acquisition and analysis

This chapter presents the experimental part of this work. Vibration measurements were carried out on the Geierlay footbridge in Germany. After a brief description of the footbridge[1] based on [15], [27] and [48], the experimental campaign is presented and more particularly the followed process as well as the conditions on site. The measurements are then analyzed and interpreted in order to determine the modal properties of the Geierlay.

3.1 Description of the footbridge

The Geierlay footbridge is located in western Germany and links the villages Mörsdorf and Sosberg. It is open to the public since October 2015, after a record construction time of less than six months. The footbridge, which hovers 100m above the ground[2] and has a span of 360m, offers an exceptional view of the valley, as suggests figure 4.

Figure 4: View of the Geierlay footbridge (right: Mörsdorf / left: Sosberg) [59]

The study, as well as the construction planning of the footbridge, were made by the Swiss

---

[1] Note that some information in this section may differ with that given in the previous master thesis [30] and [42] due to misunderstandings.

[2] The value of 100m is obtained by taking the difference between the entrance to the footbridge on the Mörsdorf side, which is approximately at a level of +321.00m and the lowest point of the valley being approximately at a level of +220.32m.

engineer Hans Pfaffen and his engineering office. He provided us with a document [48] that contains part of the static study which was carried out.

It also contains the composition of the footbridge and the materials that were used. The Geierlay is made of a successive arrangement of 195 elements of type A (every 1.5m) and 46 of type B every time the bridge is retained in the transverse direction by cables (approximately every 7.45m, except at the entries). Both element types are shown in figure 5.

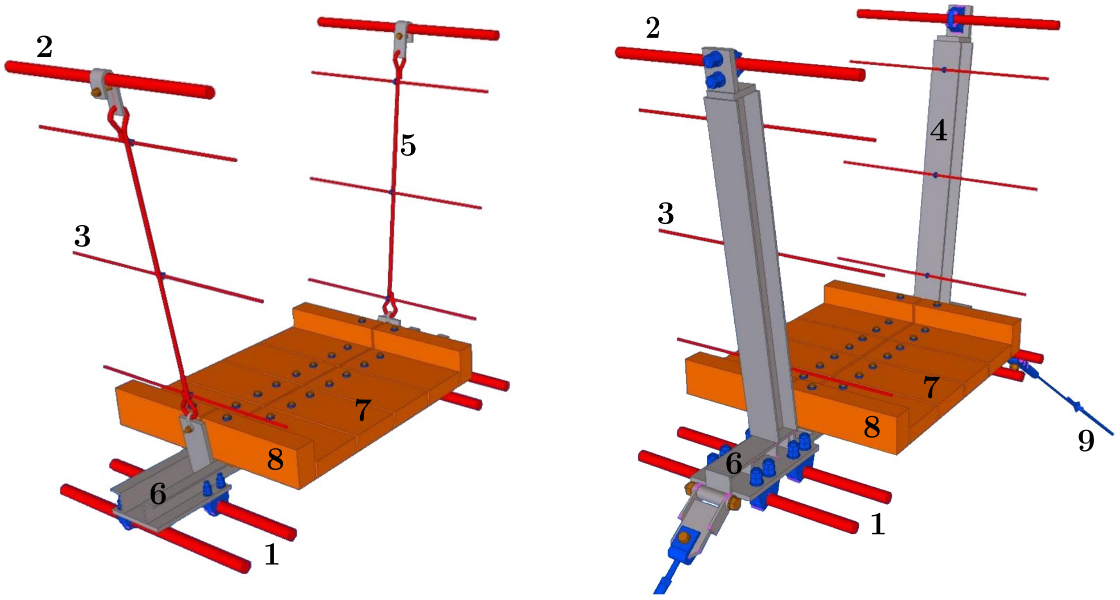

Type A

Type B

Figure 5: Elements forming the Geierlay footbridge (adapted from [48])

Thus, the footbridge consists of several suspended cables, four with a diameter of 40mm at the bottom (1) and two with a diameter of 34mm on top, which also serve as a handrail (2). A 50mm by 50mm grid made of cables with a diameter of 4mm is set up at each side on a height of 900mm for pedestrian safety[3]. This is reinforced by three ropes of 8mm diameter at each side, at the bottom, middle and top of the mesh grid (3). Additionally, every 1.5m there are vertical columns HEA100 (4) or a metal rod (5) at each side inclined from the vertical. At the same intervals, there are horizontal beams (6) placed on the four bottom cables, on top of which the floor covering is deposited. It is made of 1.48m long wooden boards with a section of 200mm by 60mm and are placed in a row of four with a spacing of 10mm to form a footpath 85cm large (7). At each side, there are wooden borders of the same length, but with a section of 80mm by 120mm (8). At the ends, the bridge is hooked to two massif concrete abutments. Moreover, the footbridge is retained transversely mainly against wind loads by several lateral cables of 14mm diameter (9). These are near the ends of the bridge directly anchored to the ground and otherwise connected to two long parabolic cables (10)[4], one at each side of the footbridge. These are of 32mm diameter and their ends are directly anchored to the ground.

Regarding the properties of the used materials, the reinforced concrete has a self-weight of 25kN/m^3 and has a resistance class of C30/37. The steel has a self-weight of 78.5kN/m^3

---

[3] The mesh grid is not visible in figure 5.

[4] The long parabolic cables on each side of the footbridge are not shown in figure 5, but are visible in figure 4.

and belongs to the resistance class S355. The used wood is of the type Larch, it has a self-weight of 7.2kN/m^3, to which 10% of its self-weight is added to take into account any possible water absorption. Thus finally, it has a self-weight of 7.92kN/m^3. Three different types of structural cables are used to build the footbridge, fully locked cables (FLC), open spiral strands (OSS), both of norm DIN EN 12385-10 and stranded ropes (SR) of norm DIN EN 12385-4. The properties of the different cables are summarized in table 1.

Cable number	Type	Weight [kg/m]	Young's modulus [MPa]	Diameter [mm]	Metal cross section [mm^2]	Maximum load [kN]
1	FLC	9.2	160000	40	1104	1082
2	OSS	5.8	150000	34	706	702
3	SR	0.3	112500	8	40	24
9	SR	1.0	112500	14	127	74
10	OSS	5.1	150000	32	625	620

Table 1: Properties of the different cables used for the Geierlay footbridge

The footbridge can be considered as a light structure with a total self-weight of 170.3kg/m, which is obtained by taking the sum of:

- the four suspension cables at the bottom (1) and the two cables above (2): 36.8+11.6=48.4kg/m,
- the mesh grid: 7.2kg/m,
- the three cables at each side (3): 1.8kg/m,
- the wooden boards (7) and wooden borders (8): 15.2+38.0=53.2kg/m,
- ropes and clamps for wind bracing: 16.0kg/m,
- and the steel structure (4, 5, 6): 43.7kg/m.

To have a safety margin, the bridge is designed for an exploitation load of 2.5kN/m^2, which is higher than the value recommended by the Eurocode[5]. As the footbridge has an 85cm large footpath, the load per unit length is equal to 2.125kN/m. For more information about the variable loads (snow, wind, temperature), the reader may refer to [48].

The information concerning the sagging deflection of the footbridge lacks precision. The engineering office Pfaffen [48], only provided us with the additional deflection under four different load cases, given in table 2. These values are given compared to the shape of the complete empty footbridge even without any self-weight.

Load cases	Deflections [m]
Self-weight	+ 1.56
Heated by 30°C	+ 0.48
Cooling by 30°C	− 0.22
Full load	+ 2.73

Table 2: Deflections under 4 different load cases

---

[5] Eurocode recommends an exploitation load of: $2.0 + \frac{120}{span+30}$. Thus, a value of $2.308kN/m^2$ for the Geierlay footbridge with a span of 360m

According to the engineer Norman Kratz from the Stadt-Land-plus GmbH office, who was responsible for the construction management of the footbridge, it's sagging deflection is about 21m. This value differs from that given in [15], where a deflection of approximately 25m is given. In this same reference, a maximum entry slope of approximately 27% is also mentioned. Since [48] indicates that there is a 4m altitude difference between both entries and knowing that the Mörsdorf side is higher, the given maximum slope has to be on that side, as shown in figure 6.

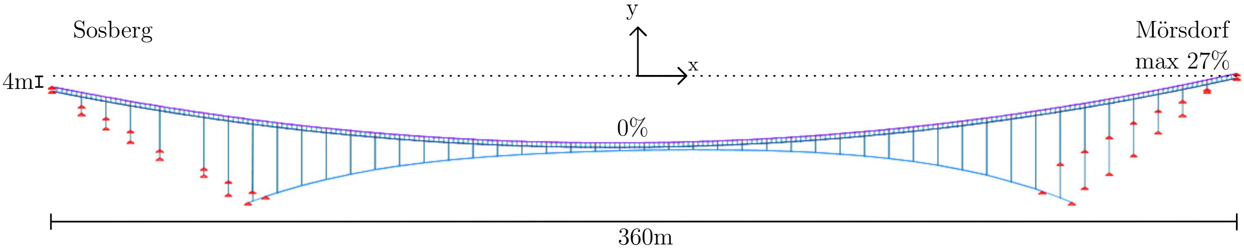

Figure 6: Elevation view of the Geierlay (adapted from [48])

By assuming that the footbridge can be assimilated to a parabola, its shape can be described by the general equation:

$$f(x) = ax^2 + bx + c \tag{3.1}$$

In the frame indicated in figure 6, the Mörsdorf entry has the coordinates (180,0) and the Sosberg entry (-180,-4). A third condition is added, by demanding that $f'(180) = 27\%$. Such that the unknown coefficients are: $a = 7.1 \cdot 10^{-4}$, $b = 0.0111$ and $c = -25.3$.

Thus, a slope of 0% is reached at a -7.74m distance from the mid-span. More interestingly, the maximum deflection relative to Mörsdorf entry is $|f(-7.74)| = 25.34$m, or equal to 21.34m relative to the Sosberg entry. Since it was not possible to have a clarification on that matter, one can assume that the deflection difference between the value given by Norman Kratz and [15] are due to a reference to a different entry. Moreover, since the slope of 27% is said to be a maximum value, one may also assume that the value of 25.34m is achieved for full loading of the footbridge. Under self-weight only, a value of the deflection equal to 22.61m relative to the Mörsdorf entry may be deduced from table 2. In the following a mean value of the deflection relative to both entries is taken, thus $d = 20.61$m under self-weight only and $d = 23.34$ under self-weight and full loading. This corresponds to the value obtained with respect to the line connecting both entries.

According to [29], a cable can be assimilated to a parabola, in the case of an inextensible cable with a large span to deflection ratio L/d (> 10) under a uniformly distributed load, like its self-weight for example. Or in the case of an inextensible cable with an arbitrary L/d ratio, but a uniformly distributed load, much higher than the self-weight of the cable. For the Geierlay $L/d = 360/20.61 \simeq 17.47$. Thus, the first condition is verified and the footbridge can indeed be assimilated to a parabola.

The length of the footbridge, can now be found by using the formula to calculate the length of a portion of curve, given by:

$$l = \int_{x_1}^{x_2} \sqrt{1 + (f'(x))^2} dx \tag{3.2}$$

In this case the integral is computed in the interval $x_1 = -180$m and $x_2 = 180$m and yields a length of $l = 363.90$m.

3.2 Data acquisition

The data acquisition was done on the 3rd September 2020 on site with four high performance X2-5 accelerometers data logger, illustrated in figure 7. Originally named B45E, A8D2, 4743 and A2D8, they are called *a*, *b*, *c* and *d* in the following for simplicity. The accelerometers are placed on the horizontal steel beams of the footbridge, perpendicular to the walking path. These correspond to the element number 6 shown in figure 5. The accelerometers are able to record the accelerations of the footbridge in three directions, i.e transversal (x), longitudinal (y) and vertical (z).

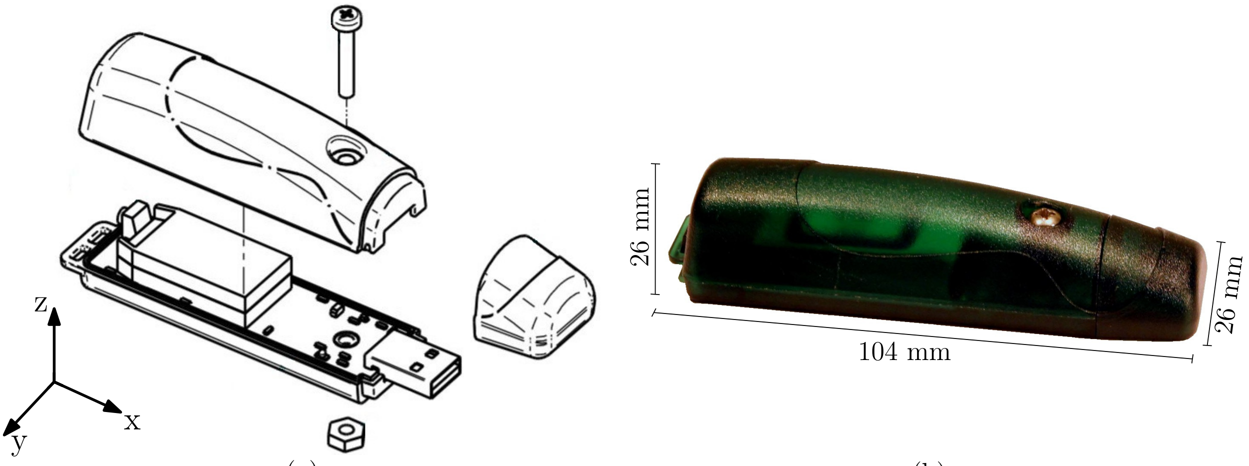

(a) (b)

Figure 7: Exploded view (a) and picture (b) of an high performance accelerometer X2-5, indicating the sensor's orientation and the device's dimensions (adapted from [9])

Based on [9], the accelerometers have a micro-resolution feature that assures a 0.1ms timing precision. They are considered to have a high sensitivity and to be low noise. It is possible to select a sampling rate between 4 and 2000Hz[6]. Additionally, they have a 2g and 8g range modes. It works as a mass storage device and due to its USB connection, the recorded data can easily be transferred from the device to a computer for post-processing.

Three sets of measurements are carried out, using the same positioning of the sensors for the first two and a different one for the last set, as shown in figure 8.

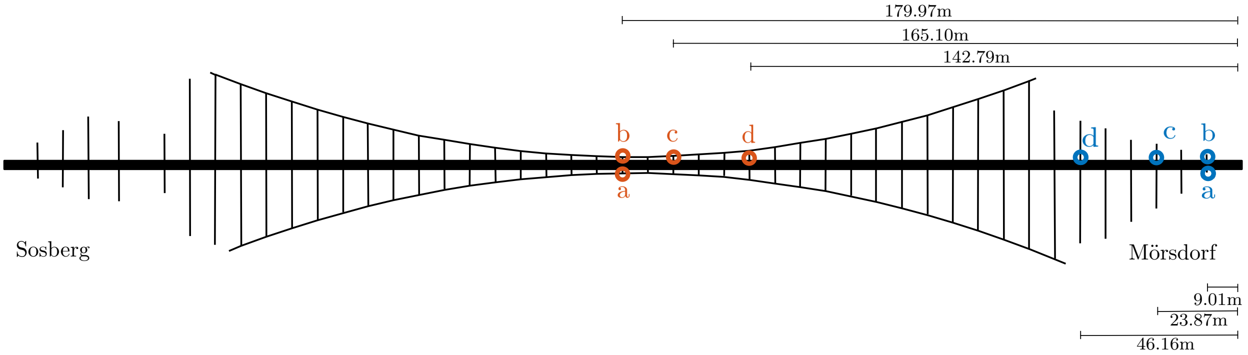

Figure 8: Location of the sensors for the data acquisition (blue: 1st and 2nd set / orange: 3rd set) (adapted from [48])

---

[6] More precisely, the user can select a sampling rate between 4, 8, 16, 31, 62, 125, 250, 500, 1000 and 2000Hz.

Note that for the first set, the sensors a and c did not work correctly. This is why the second set of measurements is done by positioning the sensors at the same location. The aim of placing the sensors a and b at the same level but on both sides of the bridge is to be able to capture possible torsion effects.

The approximate duration for each set of measurements has been calculated and they are given in table 3 which specifies the start and the end time. However, the sensors were not all set up and picked up exactly at the same moment, as several seconds were needed to go from one location to another.

Set of measurements	Start	End	Duration
First	11h25	12h36	71min
Second	13h10	14h36	86min
Third	14h44	15h42	58min

Table 3: Approximate measurements duration

Due to the covid-19 pandemic, some security measures were active at the date of the data acquisition. Such as, the pedestrians could only cross the footbridge in one direction, which changed every hour. At odd hours, it was possible to go from the Mörsdorf side to Sosberg and at even hours the reverse. Plus, the pedestrians were sent by groups of about 20 to 25 on the footbridge. According to observations made on site and post-processing of a short video done on site, every two to three minutes a new group is sent, counting from the first person to set a foot on the bridge, from the previous group to that of the next group. Besides, each group needs a little more than one minute to be completely on the bridge. In the beginning, the group is quite compact and begins to split around the middle of the bridge, because the pedestrians take pictures and because of the beginning of the upward slope. This can be seen in figure 9.

Figure 9: Capture from video post processing showing two groups of pedestrians on the footbridge

The last group was then sent ten minutes before the full hour, to be sure that the bridge is empty at the moment the pedestrians cross it in the other direction. Actually, one person takes about 9 minutes to cross the bridge, taking into account a few stops to take some pictures and admire the view. Consequently, it was not possible to measure a large enough free response of the footbridge. In fact, the greatest duration is 40s for the second set and only 30-32s for the first and last one.

An example of the measured accelerations in the vertical, transverse and longitudinal direction for the second set of measurements done with accelerometer d, are shown in figures 10, 11 and 12. As a reminder, for the second set, the accelerometers are placed at the beginning of the footbridge on the Mörsdorf side, as shown in figure 8. The first perturbation corresponds to pedestrians crossing the footbridge from Mörsdorf to Sosberg. Thus they face a downward slope when they pass near the accelerometers. Then the small free response of approximately 40s can be observed. For the second perturbation, the pedestrians cross the footbridge in the other direction and they walk on an upward slope near the accelerometers. As described above, the group of pedestrians sent on the footbridge is quite compact, but once the ascendant slope begins the group stretches out. Thus, one could expect smaller acceleration amplitudes for the second perturbation, since the group of people is more separated. However, this is not the case. Additionally, even if for the second perturbation the accelerometers are placed on the other end of the footbridge, accelerations are directly recorded. Due to the flexibility of the footbridge any perturbation is directly captured, no matter where it is applied.

One may expect that the accelerations measured at the end of the footbridge are slightly smaller than those measured at midspan for the third set. Due to a higher stiffness at the ends of the footbridge, where it is hooked to a massif concrete abutment and some lateral cables are directly anchored into the ground. Again, this is not observed. Notice that the measurements of the different sets were not recorded at the same time and under the same conditions and thus can not be compared. In fact, the last measurements were carried out later that day, where fewer pedestrians were crossing the footbridge. All the measured accelerations are assembled in Appendix C.

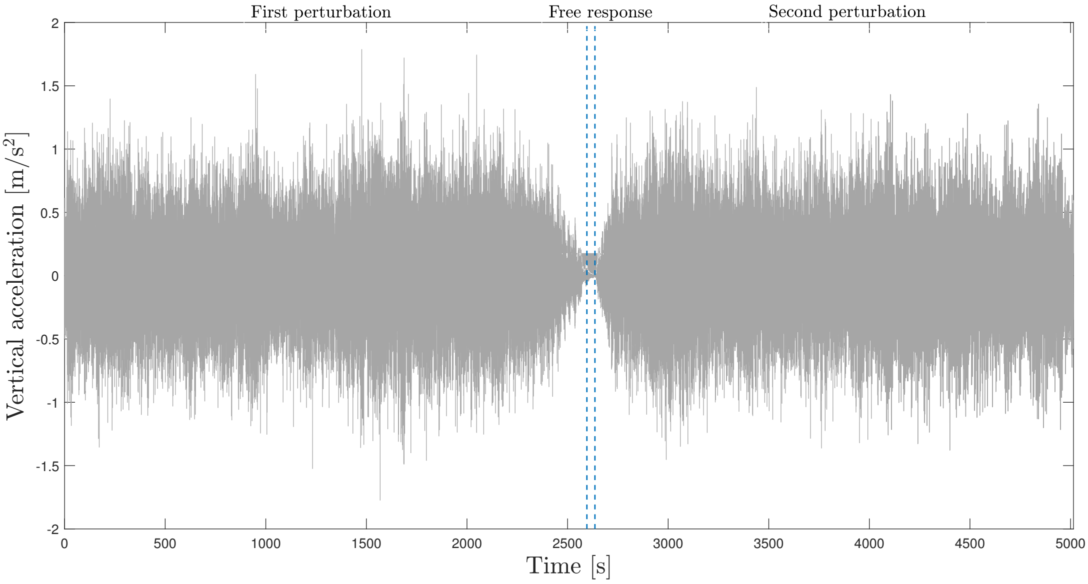

Figure 10: Vertical accelerations recorded with sensor d during the 2nd set

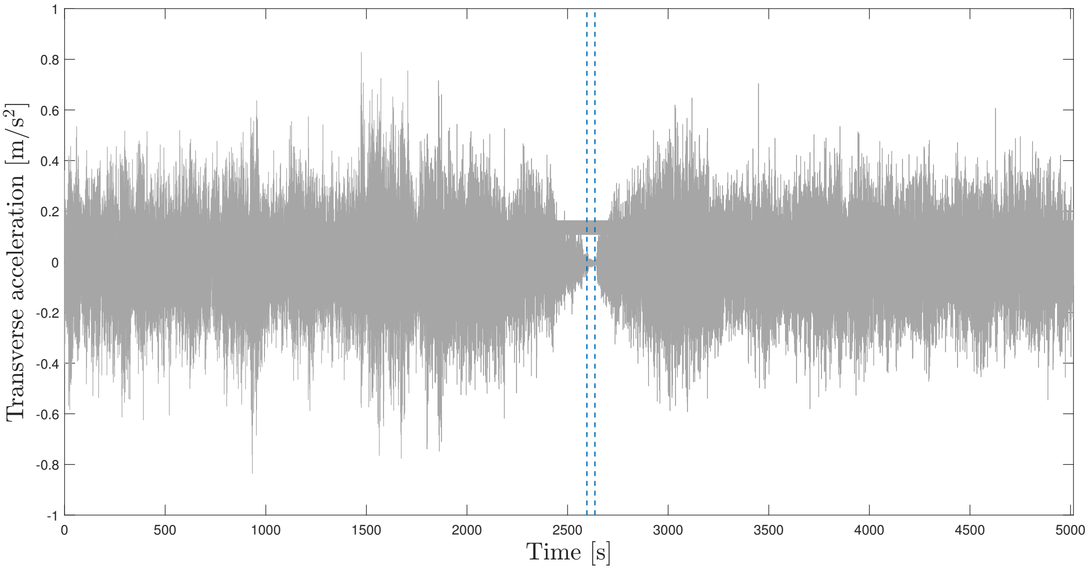

Figure 11: Transverse accelerations recorded with sensor *d* during the 2nd set

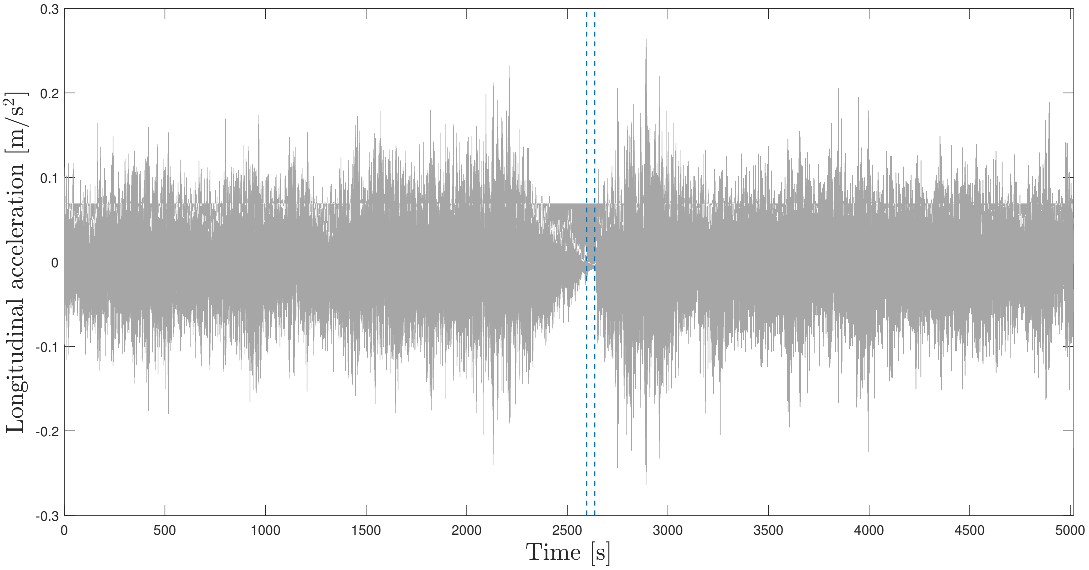

Figure 12: Longitudinal accelerations recorded with sensor *d* during the 2nd set

As expected the vertical accelerations have the highest amplitude. However, even if the amplitude of the transverse accelerations is smaller, these are important. Synchronisation problems may occur precisely due to lateral vibrations.

The Sétra guide [1] suggests three comfort zones, where the third one should not be exceeded without risking discomfort for pedestrians. These are summarised in table 4.

	Acceleration ranges [m/s^2]	
	Vertical	Transversal
Maximum comfort	0 - 0.5	0 - 0.15
Mean comfort	0.5 - 1.0	0.15 - 0.30
Minimum comfort	1.0 - 2.5	0.30 - 0.80

Table 4: Acceleration ranges corresponding to three comfort zones defined by [1]

Appendix A2 of Eurocode 0 [54], also gives maximum acceleration values that should not be exceeded to ensure the comfort of pedestrians.

- In the vertical direction: 0.7m/s^2
- In the horizontal direction for normal use: 0.2m/s^2 or under exceptional conditions such as a crowd: 0.4m/s^2

The values given by the Eurocode are more restrictive compared to those of the minimum comfort zone given by the Sétra guide. The measured accelerations exceed them both in the vertical and transverse direction. Concerning the intervals suggested by the Sétra guide, the footbridge can be considered to offer only minimum comfort. Indeed, on site, the vibrations could be felt and we could see that some pedestrians were afraid to cross the footbridge or at least needed to grab the handrail firmly. According to the engineer Hans Pfaffen [48], the footbridge is supposed to swing by design. A comfort study has already been carried out in [30] and similar observations were made.

Additionally, according to the Sétra guide, for horizontal accelerations below $0.10\ \text{m/s}^2$ the pedestrians on the footbridge can be considered as random and a synchronisation of only around 5 to 10% should be expected. However, if this limit is exceeded, the synchronisation can rise up to 60% or more. In the case of the Geierlay footbridge, this limit is exceeded in the transverse direction and locally in the longitudinal direction, thus a high synchronisation is likely in the present case.

3.3 Identification of the modal properties

The modal properties of a structure, such as the natural frequencies and its damping ratios are important in dynamic analysis. In this section, the modal properties of the Geierlay footbridge are identified. These are necessary in order to apply the joint input-state estimation algorithm in chapter 4 and 5.

3.3.1 Natural frequencies

The natural frequencies of the footbridge are first identified analytically based on the fundamentals of cable dynamics [52] and then based on the acceleration measurements done on site. These values are finally compared to those obtained in [42] based on a model of the Geierlay done with the software *FinelG*, which employs the finite elements method. For more information, the reader may refer to [20].

Analytical identification

In [52], the identification of the natural frequencies is based on the linear theory of cable vibrations. Due to the linearisation, the in-plane and out-of-plane motion are decoupled. Such that this theory is only applicable in the case of small cable vibrations. Additionally, this theory is used for a rigidly supported cable, under a quasi-static elastic deformation and a small deflection over span ratio ($0 \leq d/L \leq 1/8$). For the Geierlay footbridge, this ratio is equal to $20.61/360 \simeq 0.057 \leq 1/8$, so the linear theory of vibrations may be applied.

A fundamental characteristic parameter of a suspended cable, also called the Irvine parameter λ^2 is defined. It takes into account both geometric and deformational characteristics and is given by:

$$\lambda^2 = \left(\frac{mgl}{T}\right)^2 \cdot \frac{l}{\frac{TL_e}{EA_0}} \tag{3.3}$$

where m is the mass of the cable per unit length, g is the gravitational acceleration (9.81m/s^2), T is the tension in the cable of section A_0 and a Young modulus E. Two lengths appear in this expression, l the cord length and L_e is a virtual length of the cable, defined by:

$$L_e = \int_0^L \left(\frac{ds}{dx}\right)^3 dx \simeq l\left[1 + 8\left(\frac{d}{l}\right)^2\right] \tag{3.4}$$

where ds is the length of a small segment of the cable and d is the deflection of the cable.

The Irvine parameter can be used to verify if a cable is correctly stressed or not. For instance, a small value of λ^2 represents highly stressed and low sagging cables, whereas a large value represents low stressed and high sagging cables. Thus, this parameter can be employed for the inspection of a cable-stayed bridge, where a small value of λ^2, typically between 0 and 1 is expected. As shown in figure 16, in that case, the natural frequencies are multiples of the fundamental natural frequency. If this condition is not verified, the stay cable has to be tensioned.

In order to verify this parameter for the Geierlay, the footbridge has to be assimilated to a single cable, but with the corresponding properties. The goal of such a procedure is to know if the natural frequencies will be multiples of the first one or not. Hopefully, this will simplify the identification of the frequencies based on the measured accelerations. First, the various quantities involved in equation (3.3) need to be calculated. The chord length of the cable and its deflection are taken equal to those of the footbridge, $l = 363.9\text{m}$ and $d = 20.61\text{m}$. Such that, $L_e \simeq 373.24\text{m}$. The equivalent cable section is taken equal to the sum of the four suspension cables at the bottom (1), the two cables above (2) and the three cables of each side (3) which are shown in figure 5. Based on table 1, the equivalent cable section can be calculated as well as the equivalent Young's modulus. It is taken proportional to the different cable sections:

$$A_0 = 4 \cdot 1104 + 2 \cdot 706 + 6 \cdot 40 = 6068\text{mm}^2$$

and

$$E = \frac{4416 \cdot 160000 + 1412 \cdot 150000 + 240 \cdot 112500}{4416 + 1412 + 240} = 155794.33\text{MPa}$$

As shown in [62], the prestressing forces T in the various cables have a direct impact on the modal properties of a flexible structure. For instance, a higher prestressing force increases the natural frequencies. This is why this value appears directly in the definition of the Irvine parameter.

Depending on whether the cable has supports on the same level or not, a different procedure has to be followed to determine the tension in a cable. These are given in Appendix B. In [52], a distinction between horizontal and inclined cables is also done. As already mentioned above, for the Geierlay, there is a 4m altitude between both entries of the footbridge for a span of 360m, which gives a global inclination of approximately $\theta \simeq 0.64°$. Thus, the inclination is very small and the influence is negligible as will be shown below. The Geierlay footbridge can thus be assimilated to a horizontal cable. Hence, the well-known formula for the computation of tension in a parabolic cable with supports at the same level as in figure 13 may directly be applied.

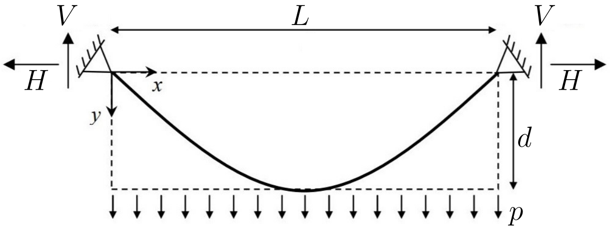

Figure 13: Scheme of a parabolic cable with supports at the same level (adapted from [29])

The horizontal support reaction is given by:

$$H = \frac{pL^2}{8d} \tag{3.5}$$

The vertical reaction is simply $V = \frac{pL}{2}$ and thus the tension in the cable is $T = \sqrt{H^2 + V^2}$. By considering V small enough compared to H the assumption $T \simeq H$ is often made.

The tension in the equivalent cable representing the footbridge can be obtained by applying equation (3.5). The lateral parabolic cables, whose dimensions are shown in figure 14 have been neglected so far. Their favourable effect can however be taken into account by adding a corresponding load on the equivalent cable, as done in [30] and [42]. The same procedure is followed here, but by adapting the values.

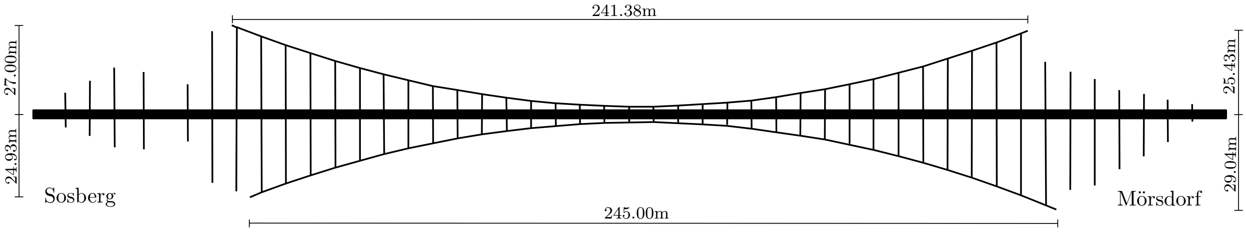

Figure 14: Dimensions of the lateral parabolic cables of the Geierlay footbridge

The initial prestressing force in the lateral parabolic cables is given in [57] and is approximately equal to T =100kN. As these cables have different dimensions, their tension may be slightly different too. Due to a lack of information, the only given prestressing force is used for both and their mean dimensions are used, such as a span length of L =243.19m and a deflection of d =26.6m. According to equation (3.5), this corresponds to a load of:

$$p = \frac{T8d}{L^2} \simeq 0.360\text{kN/m}$$

These two cables are linked to the footpath through various lateral inclined cables, such that only a part of the calculated load is transmitted to the footpath. Based on construction plans from the section of the footbridge given in [48] and shown in figure 15, an angle of 35° relative to the horizontal can be measured. Thus the vertical load becomes only $0.360\sin(35) = 0.206$kN/m or 21.04kg/m.

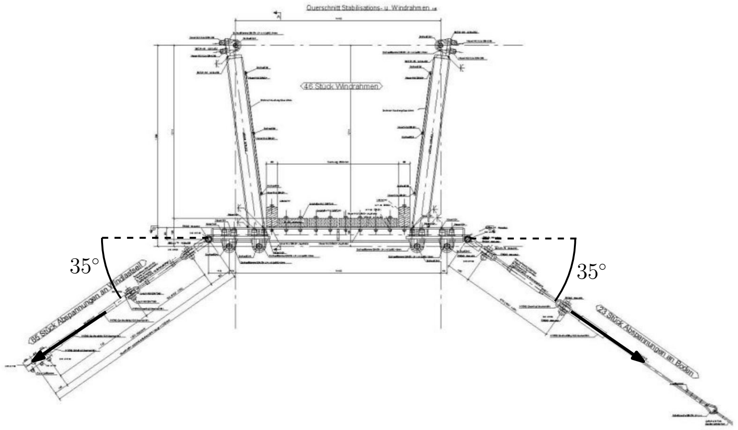

Figure 15: Construction plan of one section of the Geierlay footbridge (adapted from [48])

To take into account both cables, this value is multiplied by two and added to the self-weight of the footbridge. Thus,

$$m = 170.30 + 2 \cdot 21.04 = 212.38\text{kg/m}$$

The tension in the equivalent cable modelling the footbridge is then obtained by using equation (3.5):

$$H = \frac{pL^2}{8f} = \frac{212.38 \cdot 9.81 \cdot 360^2}{8 \cdot 20.61} \simeq 1637.64\text{kN}$$

Finally, the Irvine parameter for the Geierlay footbridge modelled by a single cable given by equation (3.3), yields:

$$\lambda^2 = \left(\frac{212.38 \cdot 9.81 \cdot 363.9}{1637.64 \cdot 10^3}\right)^2 \cdot \frac{363.9}{\frac{1637.64 \cdot 10^3 \cdot 373.24}{155794.33 \cdot 6068}} \simeq 120.63$$

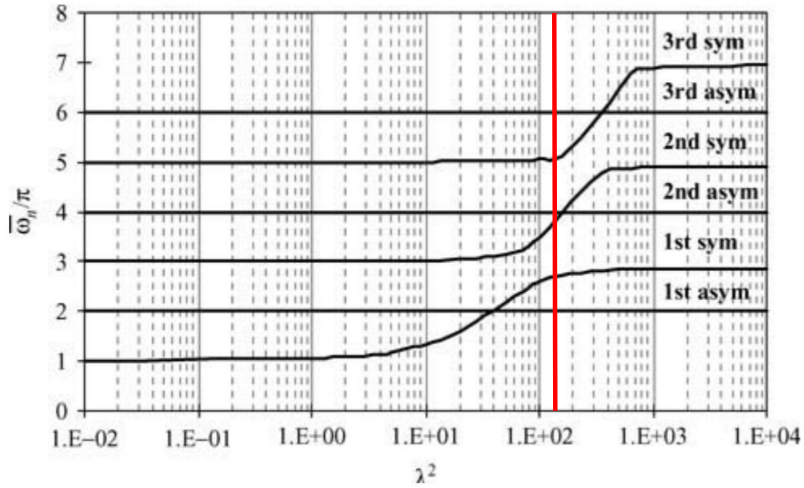

Figure 16: Variation of the natural frequencies of the six first in-plane modes of vibration with the Irvine parameter (adapted from [52])

A high value of λ^2 is obtained as expected for suspension bridges, where the principal cable is low stressed and highly sagging. Thus, as shown in figure 16, for the Geierlay one can not expect to have natural frequencies multiples from the first one for the in-plane motion, at least with regard to the symmetrical modes.

The natural frequencies can be calculated analytically based on the formulas derived in [52]. For an out-of-plane motion, these can be obtained by:

$$\omega_n = \frac{n\pi}{L} \cdot \sqrt{\frac{H}{m}} \tag{3.6}$$

where L is the footbridge's span which is equal to 360m, $H = 1637.64\text{kN}$ is the horizontal component of the tension in the cable under its self-weight and the effect of the lateral parabolic cables, obtained through equation (3.5). $m = 212.38\text{kg/m}$ has also already been calculated above. $n = 1, 2, 3, ...$ is the nth frequency of vibration. This can also be expressed as a function of the adimensional natural frequency

$$\bar{\omega}_n = n\pi$$

with

$$\bar{\omega}_n = \frac{\omega_n L}{\sqrt{H/m}} \tag{3.7}$$

To verify the initial assumption, for an inclined cable, the nth adimensional natural frequency is defined as:

$$\bar{\omega}_{*,n} = \frac{\omega_{*n} L_{*n}}{\sqrt{H_{*n}/m}}$$

where $L_* = L\sec\theta$ and $H_* = L\sec\theta$. In the case of the Geierlay $\theta = 0.64°$ and $\sec\theta \simeq 1$. Thus the effect of the inclination can indeed be neglected.

For the in-plane motion, one may distinguish anti-symmetric and symmetric modes. The first ones, are given by $\bar{\omega}_n = 2n\pi$ or:

$$\omega_n = \frac{2n\pi}{L} \cdot \sqrt{\frac{H}{m}} \tag{3.8}$$

The natural frequencies corresponding to the symmetric in-plane modes are the roots of

$$\tan\frac{\bar{\omega}}{2} = \frac{\bar{\omega}}{2} - \frac{4}{\lambda^2}\left(\frac{\bar{\omega}}{2}\right)^3 \tag{3.9}$$

where λ^2 is the Irvine parameter already defined earlier and equal to 120.63 for the Geierlay. To avoid solving equation (3.9), the $\bar{\omega}_n/\pi$ values can directly be read from figure 16. For the given λ^2, they are approximately equal to 2.7, 3.9 and 5.0s^{-1} for the 1st, 2nd and 3rd symmetric mode.

The frequency f_n expressed in Hz, is finally obtained by

$$f_n = \frac{\omega_n}{2\pi} \tag{3.10}$$

and the different values for the three first modes for out-of-plane and in-plane motion are summarized in table 5. A regular spacing of 0.124Hz is observed for the out-of-plane motion and of 0.248Hz for the anti-symmetric in-plane motion. As shown above, when calculating the Irvine parameter λ^2, there is no regular spacing for the symmetric in-plane motion.

Mode	Out-of-plane motion	In-plane motion	
		anti-symmetric	symmetric
1st	0.122	0.244	0.320
2nd	0.244	0.488	0.463
3rd	0.366	0.732	0.593

Table 5: The first natural frequencies [Hz] obtained based on the linear theory of vibrations

Identification based on the measured accelerations

Before identifying the natural frequencies based on the measurements, it is interesting to verify if the locations for the sensors were well chosen. If a sensor was placed at a node of the mode, this sensor was not able to collect any information concerning that mode. For a cable on two supports, if the modes are considered uncoupled, the vertical or transversal modes which are here of interest can be represented as in figure 17.

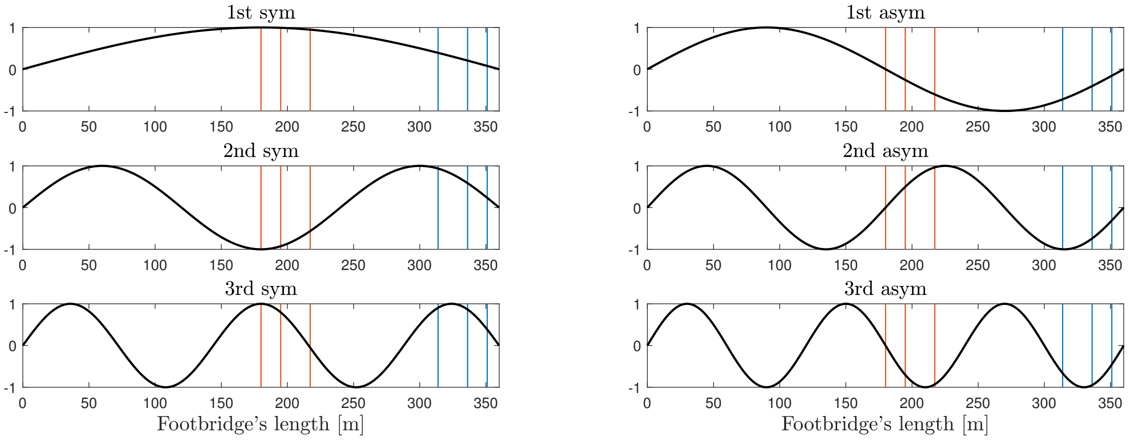

Figure 17: The three first symmetric and anti-symmetric vertical or transveral mode shapes and the locations of the sensors, right being the Mörsdorf side and left the Sosberg side. (blue: 1st and 2nd set / orange: 3rd set)

However, notice that the Geierlay footbridge is not only hooked at both ends, it is also retained transversely by several lateral cables, which are either directly anchored to the ground or connected to the lateral parabolic cables. The ends of which are then anchored to the ground. Thus, the mode shapes shown in figure 17 would correspond to the reality only if the lateral cables had a negligible stiffness. This is not the case, otherwise they would be useless. Thus the footbridge behaves more like a cable on multiple spring supports, as shown in figure 18, whose mode shapes depend on the stiffness of the springs and are thus more complicated to predict. The first mode shapes of the footbridge are provided in Appendix D, they have been extracted from the model.

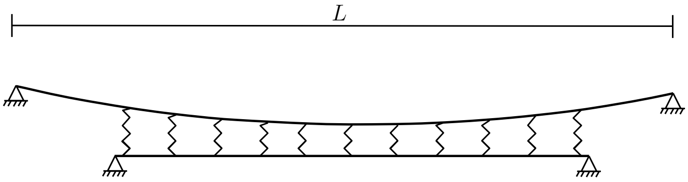

Figure 18: Cable on multiple spring supports representing the Geierlay footbridge

The natural frequencies can be identified by using the peak picking (PP) method, which is a frequency-domain spectrum-driven method. It consists in reading the peak values of a spectrum plot, which is here obtained by doing a fast Fourier transform (FFT) of the time-domain accelerations. Due to its simplicity, this method is often used in civil engineering for the identification of the modal properties of a structure. It is based on the assumption that the frequencies of each mode are well-separated, thus each peak of the spectrum plot corresponds to a single mode as explained in [47].

If all the signal of a set of measurements is taken into account, most of it is a result of pedestrian loads. Starting approximately from 2Hz, which corresponds to the step frequency for a normal walk, it can be seen in figures 19 and 20, for the out-of-plane motion and the vertical motion, that it is impossible to clearly distinguish any peaks corresponding to a natural frequency of the structure. Whereas, in figure 20 for the longitudinal direction it is possible to identify up to high frequencies. The results for the three sets of measurements shown here[7] can already be used to identify the first natural frequencies of the footbridge.

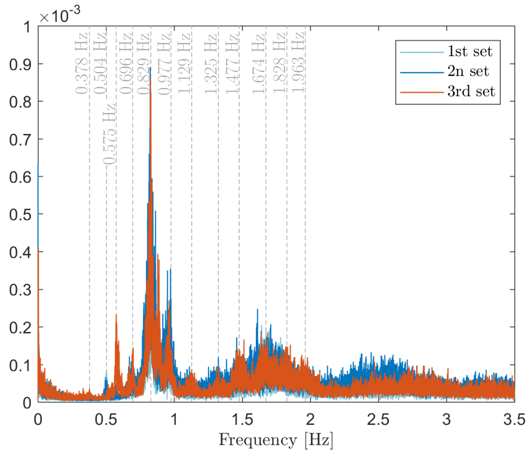

Figure 19: FFT of out-of-plane accelerations under pedestrian crossing

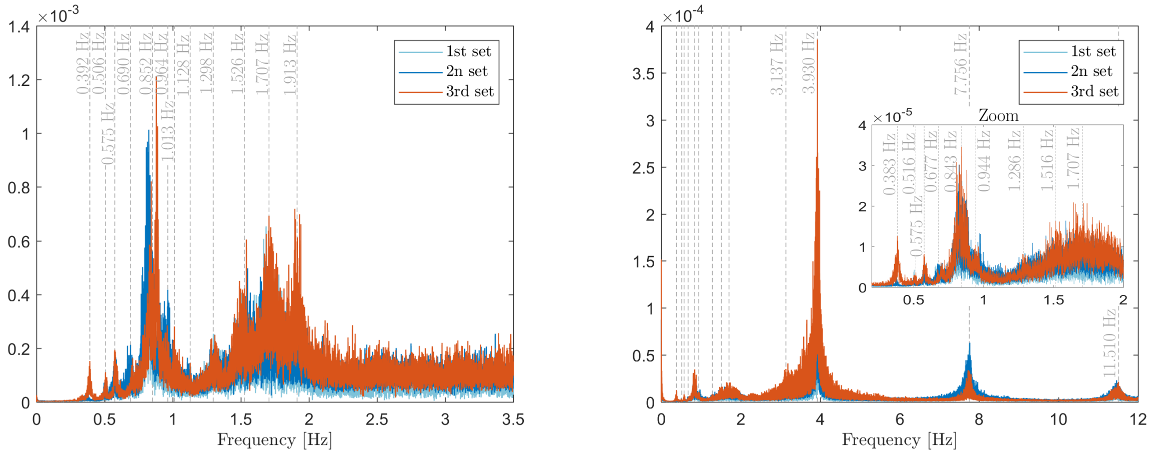

Figure 20: FFT of the in-plane accelerations under pedestrian crossing (left: vertical /right: longitudinal)

---

[7] The FFT for each measurement set is obtained by doing the root mean square (RMS) of the FFT corresponding to each sensor.

However, if only the free response part of measurements is used, it should be possible to identify clearer and higher modes in the vertical and transverse directions. As mentioned in section 3.2, it was not possible to measure a free response longer than 30-40s. To verify if it is long enough to identify the natural frequencies, only a third, then two thirds and then all the free response signal is used. By comparing the FFT of the three signals, it was possible to observe similar peaks for the last two. Thus, we can assume that a little bit longer free response signal would not considerably change the identification of the natural frequencies. In figures 21 and 22, the FFT of the three sets of measurements are shown. Only the results of the out-of-plane and vertical accelerations are shown here, as they are the most interesting: the vertical ones due to their higher amplitudes and the transverse ones due to a possible origin of a synchronisation problem, which generally occurs in that direction.

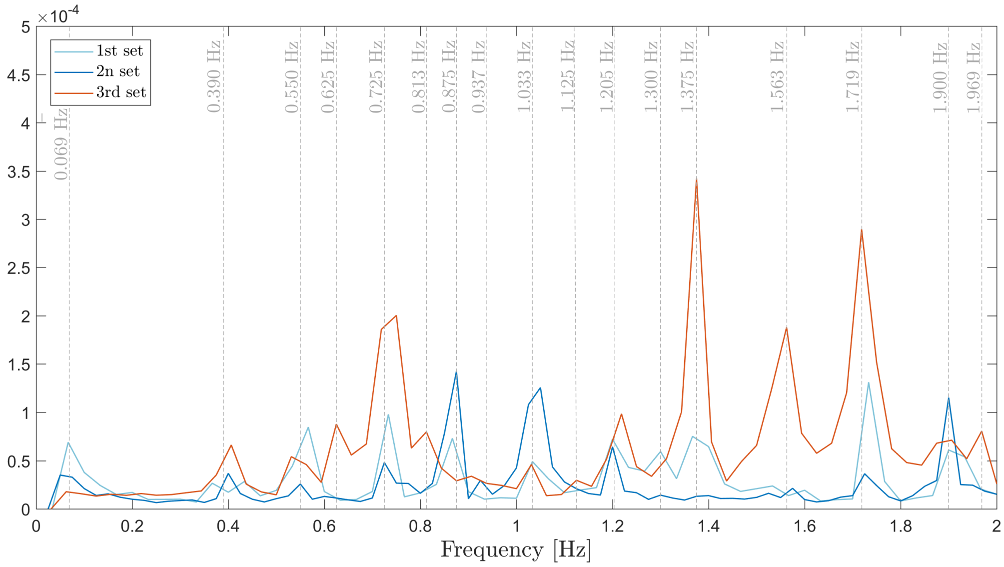

Figure 21: FFT of out-of-plane free response accelerations (transverse)

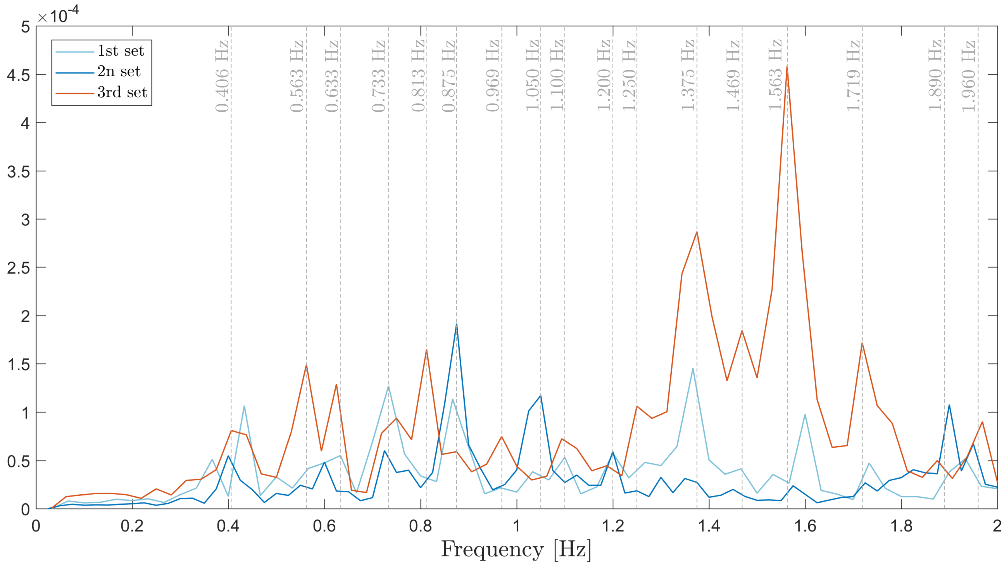

Figure 22: FFT of in-plane free response accelerations (vertical)

The identification is limited here to a frequency of 2Hz, but it would be possible to identify higher frequencies based on these signals. As expected more peaks can be identified, including those seen in figures, 19 and 20 where the entire signal, also the part under pedestrian crossing, was kept. Thus these are the ones used to identify the natural frequencies of the footbridge.

Notice that the natural frequencies identified from the full signal and from the free response only, are similar, but not exactly the same. In fact, the pedestrians have an influence on the identified frequencies, which explains the small differences. This effect increases with the number of pedestrians on the footbridge. In [53], it is shown that the natural frequencies tend to increase due to pedestrians walking on the structure. As the frequencies are directly proportional to the ratio $\sqrt{k/m}$, they assume that the modal stiffness k increases faster than the modal mass m. However, in our case, the opposite can be observed. This can be linked to the fact that the tests in [53] are carried out on a rigid structure. On the contrary, here the footbridge is flexible. This would mean that for a flexible footbridge the additional mass due to the pedestrians increases faster than the additional stiffness. The fact that the natural frequencies of a flexible footbridge decrease due to a human-structure interaction is confirmed in [3], where the same observations are made based on tests carried out on a flexible structure.

Additionally, some identified frequencies based on the transverse and vertical accelerations are very similar. From the linear theory of cable vibrations we already know that the natural frequencies for the out-of-plane motion are given by a multiple $n = 1, 2, 3, ...$ of $\pi/(L\sqrt{m/H})$ and those for the anti-symmetric in-plane modes are given by a multiple $2n$. Thus some of the identified frequencies should be the same.

Comparison

In this section, the natural frequencies obtained analytically, the ones based on the measured accelerations and the ones computed by FinelG can be compared.

Notice that the results obtained analytically do not really correspond to those obtained from the measurements. In fact, the hypothesis of being able to assimilate the bridge to a single cable having the same behaviour is not verified. Some effects are probably not taken into account, which explains the difference. The obtained values are recalled in table 6.

Mode	Out-of-plane motion	In-plane motion	
		anti-symmetric	symmetric
1st	0.122	0.244	0.320
2nd	0.244	0.488	0.463
3rd	0.366	0.732	0.593

Table 6: Recall of the natural frequencies calculated analytically

Now the natural frequencies identified from the measured free response accelerations and those obtained by the model of the footbridge done in FinelG in [42] are compared. These values are similar, as can be read from table 7, for the first vertical modes. However, for higher in-plane modes, as well as for the out-of-plane modes, it seems that not all the information has been measured. Thus, the corresponding natural frequencies can not been identified. If the footbridge behaved as a cable on two supports, it can be seen from figure

17 that not each sensor individually would be able to capture all the modes. However, by taking all sensors together, we should have enough information to identify the natural frequency corresponding to each mode. Provided, the mode was excited when taking the measurements. This confirms what has been stated above, the footbridge behaves more like a cable on various spring supports and probably some sensors were placed on or near the nodes of a given mode. More realistic mode shapes can be extracted from the FinelG model and are given in Appendix D.

Natural Frequencies [Hz]	
FinelG	Measurements
0.443	0.406
0.560	0.563
0.695	0.633
0.713	0.733
0.859	0.813
0.877	0.875
0.966	0.969
1.036	1.050
1.064	-
1.107	1.100
1.185	-
1.214	1.200
1.241	-
1.250	1.250
1.365	1.375

Table 7: Comparison of the obtained natural frequencies for the in-plane modes

Natural Frequencies [Hz]	
FinelG	Measurements
0.163	0.069
0.239	-
0.289	-
0.290	-
0.312	-
0.323	-
0.352	-
0.391	0.390
0.461	-
0.475	-
0.480	-
0.526	0.550
0.622	0.625

Table 8: Comparison of the obtained natural frequencies for the out-of-plane modes

3.3.2 Damping ratios

The damping ratios are only identified from the measurements. Based on the PP method, the already identified natural frequencies above can be used. The half-power bandwidth method (HPBWM) can then be applied to estimate the damping ratio, such that:

$$\xi_i = \frac{\omega_2 - \omega_1}{2\omega_i} \tag{3.11}$$

where ω_i and ξ_i are the natural frequency and the damping ratio corresponding to mode i. ω_1 and ω_2 are two frequency values left and right from ω_i, often taken at $\sqrt{2}$ from the peak amplitude. However, this method is considered to be not very accurate as mentioned in [47].

Another simple method is directly based on the time domain free response of the structure. Its envelope can be assimilated to a decreasing exponential, like $e^{-\xi\omega t}$ from which the value of ξ can be deduced. Here, the measured free responses of the footbridge are too short as mentioned in section 3.2 to apply this method.

The covariance-driven stochastic subspace identification method (SSI-COV) is applied in the time domain and can also be used to identify the modal properties of a structure. As explained in [47] and in [49], this method is able to identify a stochastic state-space model, like

$$\mathbf{x}_{[k+1]} = \mathbf{A}\mathbf{x}_{[k]} + \mathbf{w}_{[k]} \tag{3.12}$$

$$\mathbf{d}_{[k]} = \mathbf{G}\mathbf{x}_{[k]} + \mathbf{v}_{[k]} \tag{3.13}$$

based on correlations of the given output data, such as the vibrational response of the structure. The modal properties can then be obtained by an eigenvalue decomposition of matrix **A**. This method is used here, especially to identify the damping ratios, as the natural frequencies have already been identified in the previous section 3.3.1. A stabilization diagram is first created to see which modes the method was able to correctly identify. One example is shown in figure 23, where only the first, second and eleventh identified frequency can be considered stable. Only these are then used to identify the damping ratios, as shown in figure 24.

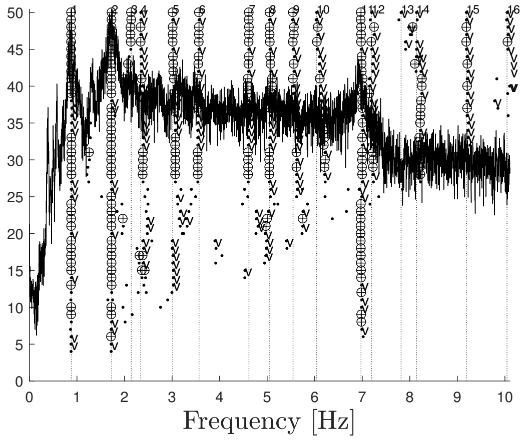

Figure 23: Example of a stabilization diagram

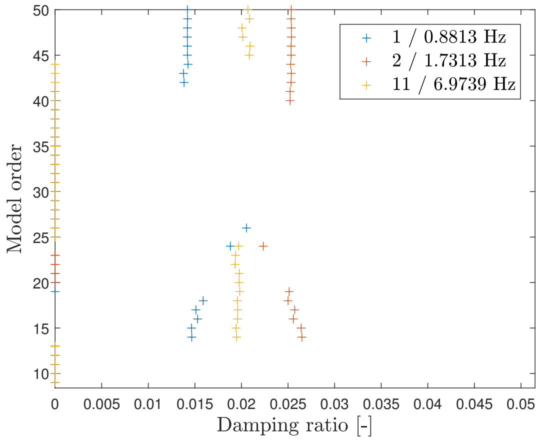

Figure 24: Identified damping ratios

This analysis can be done with each acceleration signal recorded in the vertical and transverse direction. However, it was not possible to identify more than the tree frequencies stated above. The mean values are summarized in table 9.

Frequency [Hz]	Damping ratios [%]
0.881	1.32 - 1.51
1.731	1.97 - 2.23
6.974	2.53 - 3.02

Table 9: Identified damping ratios for in-plane modes

Similar values are also obtained for the out-of-plane modes.

It has been shown in [21] and in [53] that a human-structure interaction induces an increase of the damping ratios of the footbridge. This is because humans are able to absorb a part of the energy and thereby damp the structure's motion through their knees. These effects increase with the number of pedestrians on the footbridge, like for the effects on the natural frequencies. Thus the damping ratio of the footbridge, under self-weight, only is smaller than the identified values.

Chapter 4

Validation and analysis of the algorithm

Before applying the algorithm to a real-world example, it is validated by two academic test cases which are discussed in this chapter. The first one is based on the example in [44], where the modal properties are already given, as well as the resulting modal load. The second case, is the extension of the former, by adjusting with the Geierlays geometric features and modal properties. For these two examples, the acceleration measurements are simulated by using the general definition of a single pedestrian load. In doing so, the loads identified by the algorithm can be compared to those that generated the simulated measurements. A reminder about human-induced loads is given in the first section. More information about this topic may be found in [1] and [6].

4.1 Single pedestrian loading model

A person crossing a pedestrian structure induces a dynamic loading in three directions, i.e. vertical, transverse and longitudinal, which can be considered periodic. In other words, it varies in time and repeats at regular intervals.

First, one can distinguish between walking and running, generating a continuous or a discontinuous ground contact respectively. By specifying these two main types, table 10 shows average values of the corresponding step frequency or pacing rate f_s and forward speed v_s.

	Pacing rate f_s [Hz]	Forward speed v_s [m/s]
Slow walk	1.7	1.1
Normal walk	2.0	1.5
Fast walk	2.3	2.2
Slow running (jog)	2.5	3.3
Fast running (sprint)	> 3.2	5.5

Table 10: Average values of pacing rates and forward speeds corresponding to different types of human motion [6]

The Sétra guide [1] doesn't do this distinction and only gives two ranges of step frequencies, one for walking from 1.6 to 2.4Hz and one for running from 2 to 3.5Hz.

In the context of this work, only the cases of slow and normal walking are considered, as they correspond to the types of motion usually observed on flexible footbridges. Additionally, according to the Sétra guide, a single running pedestrian crosses the footbridge in a too short amount of time to cause any problematic phenomena, such as resonance for example.

The dynamical load in the three directions due to a single pedestrian walking can be represented as in figure 25. However, it is only a schematic representation, indeed the load-time function depends on various parameters, like the pacing rate, footwear, surface conditions, the person's weight and gender or other stepping particularities. Notice that there is always an overlap of the left and right foot loads, such that there is always at least one foot on the ground. This is why for walking we talk about continuous ground contact.

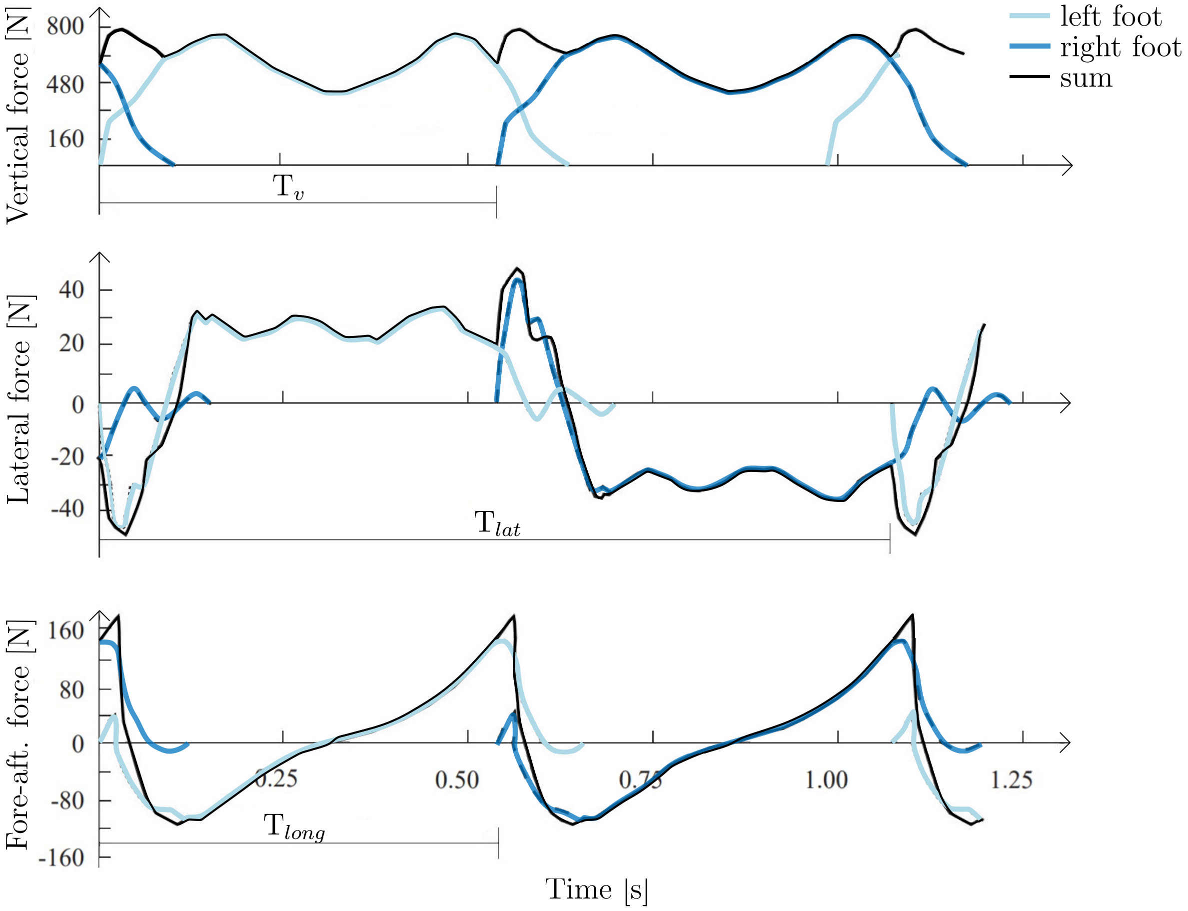

Figure 25: Example of dynamical load in vertical, transverse and longitudinal direction due to a single pedestrian walking (adapted from [63])

As shown in figure 25, the period in the vertical T_v and longitudinal T_{long} direction is defined as the time between two consecutive footsteps. Whereas the period in the lateral direction T_{lat} is equal to the time of two consecutive right or two consecutive left footsteps. This is because, the lateral load component is due to the pedestrian's balance when he changes legs, such that the steps produce a load in opposite directions. The other two components create a load in the same direction.

Thus, the vertical pedestrian load for a continuous ground contact is a periodic function, which can be decomposed into a Fourier series. It is defined by a constant term and a sum of harmonic contributions and may be written:

$$F_v(t) = W + \alpha_{1,v} W \sin(2\pi f_s t) + W \sum_{i=2}^{n} \alpha_{i,v} \sin(2\pi i f_s t - \varphi_i) \tag{4.1}$$

where W is the person's weight, generally assumed equal to 700N or 800N, f_s is the pedestrian's step frequency, φ_i is the phase angle of the ith harmonic relative to the first one. The $\alpha_{i,v}$ with i=1,2,...,n are coefficients also called dynamical load factors (DLF) or Fourier coefficients. Multiplied by the weight W, they represent the amplitude of the ith harmonic. The number of harmonics n taken into account is usually limited to three and sometimes even to only the first one. Several authors proposed different values for these coefficients. Some values for $\alpha_{i,v}$ and φ_i are summarized in table 11, taken from [7], [22], [26], [41] and [50]. For the vertical load, the Sétra guidelines suggest to use the coefficients from Bachmann et al.

Author(s)	Fourier coefficients/Phase angles [-]
Blanchard et al.	$\alpha_1 = 0.257$
Bachmann et al.	$\alpha_1 = 0.4 - 0.5$, $\alpha_2 = \alpha_3 = 0.1$ (for $f_s = 2.0 - 2.4$Hz) $\varphi_2 = \varphi_2 = \pi/2$
Schulze	$\alpha_1 = 0.37$, $\alpha_2 = 0.1$, $\alpha_3 = 0.12$ (for $f_s = 2.0$Hz) $\alpha_4 = 0.04$, $\alpha_5 = 0.08$
Kerr	$\alpha_1 = -0.265 f_s^3 + 1.321 f_s^2 - 1.760 f_s + 0.761$ $\alpha_2 = 0.07$, $\alpha_3 = 0.05$
Seiler et al.	$\alpha_1 = 0.4$, $\alpha_2 = 0.15$, $\alpha_3 = 0.1$
Young	$\alpha_1 = 0.37(f_s - 0.95) \leq 0.5$ $\alpha_2 = 0.054 + 0.0044 f_s$ $\alpha_3 = 0.026 + 0.0050 f_s$ $\alpha_4 = 0.010 + 0.0051 f_s$
Charles & Hoorpah	$\alpha_1 = 0.4$
Murray et al.	$\alpha_1 = 0.5$, $\alpha_2 = 0.2$, (for $f_s = 1.6 - 2.2$Hz) $\alpha_3 = 0.1$, $\alpha_4 = 0.05$
EC5, DIN1074	$\alpha_1 = 0.4$, $\alpha_2 = 0.2$
Synpex [1]	$\alpha_1 = 0.0115 f_s^2 + 0.2803 f_s - 0.2902$ $\alpha_2 = 0.0669 f_s^2 + 0.1067 f_s - 0.0417$ $\alpha_3 = 0.0247 f_s^2 + 0.1149 f_s - 0.1518$ $\alpha_4 = -0.0039 f_s^2 + 0.0285 f_s - 0.0082$ $\varphi_2 = (-99.76 f_s^2 + 478.92 f_s - 387.8)\pi/180$ $\varphi_3 = (-150.88 f_s^3 + 819.65 f_s^2 - 1431.35 f_s + 811.93)\pi/180$ (if $f_s < 2.0Hz$) $\varphi_3 = (813.12 f_s^3 + 5357.6 f_s^2 - 11726 f_s + 8505.9)\pi/180$ (if $f_s > 2.0Hz$) $\varphi_4 = (34.19 f_s - 65.14)\pi/180$

Table 11: Fourier coefficients for vertical dynamical loading due to walking [7], [22], [26], [41], [50]

---

[1] Advanced Load Models for Synchronous Pedestrian Excitation and Optimised Design Guidelines for Steel Footbridges (Synpex) is a European research project, on which is based among others [22].

Even if the horizontal dynamical load due to a pedestrian is smaller than the vertical one, it may be a problem for footbridges and therefore must be taken into account. The transverse horizontal and the longitudinal horizontal load for one single pedestrian are given by:

$$F_{lat}(t) = W \sum_{i=1}^{n} \alpha_{i,lat} \sin\left(2\pi i \frac{f_s}{2} t - \varphi_i\right) \quad \text{and} \quad F_{long}(t) = W \sum_{i=1}^{n} \alpha_{i,long} \sin(2\pi i f_s t - \varphi_i) \quad (4.2)$$

The horizontal loads are also usually limited to the first harmonic. Note that for the transverse load, the frequency taken into account is only the half of the step frequency f_s, this is because of the definition of the period which is double in this direction as explained above and shown in figure 25.

The Fourier coefficients $\alpha_{i,lat}$ and $\alpha_{i,long}$, differ from those given above for the vertical loading component. Some values are summarized in tables 12 and 13, based on [22]. However, on these two coefficients, there is less research carried out and therefore fewer values have been proposed. For the horizontal loads, the Sétra guidelines suggest using the coefficients from Charles and Hoorpah.

Author(s)	Fourier coefficients [-]
Bachmann et al.	$\alpha_1 = \alpha_2 = \alpha_3 = 0.1$
Charles & Hoorpah	$\alpha_1 = 0.05$
Schulze	$\alpha_1 = 0.039, \alpha_2 = 0.01,$ $\alpha_3 = 0.043, \alpha_4 = 0.012,$ $\alpha_5 = 0.015$
EC5, DIN1074	$\alpha_1 = \alpha_2 = 0.1$

Table 12: Fourier coefficients for horizontal transverse load due to walking [22]

Author(s)	Fourier coefficients [-]
Bachmann et al.	$\alpha_{1/2} = 0.1, \alpha_1 = 0.2,$ $\alpha_2 = 0.1$
Charles & Hoorpah	$\alpha_1 = 0.2$
Schulze	$\alpha_{1/2} = 0.037, \alpha_1 = 0.204,$ $\alpha_{3/2} = 0.026, \alpha_2 = 0.083,$ $\alpha_{5/2} = 0.024$

Table 13: Fourier coefficients for horizontal longitudinal load due to walking [22]

The external excitation experienced by the footbridges is composed of a temporal and spatial contribution and takes the following form:

$$p(x,t) = F(t)\delta(x - x_p(t)) \quad (4.3)$$

where $x_p(t) = v \cdot t$ is the the pedestrian position on the structure and $F(t)$ is the pedestrian load defined by (4.1) or (4.2). The dirac delta δ assures that the forced excitation is equal to zero, when the pedestrian has left the structure.

As a reminder the modal load $p^*(x,t)$ can easily be derived by using the continuous form of the equation of motion and doing a coordinate transformation to switch into the modal form, as done in chapter 2. Thus, for a SOF and by integrating it over the footbridge's length l:

$$p^*(x,t) = \int_0^l \Phi(x)p(x,t)dx = \int_0^l \Phi(x)F(t)\delta(x - x_p(t)) = F(t)\Phi(vt) \quad (4.4)$$

The definition of the modal load given by (4.4) is used to obtain the corresponding vibrational response.

4.2 Vibrational response

The vibrational response of a structure, i.e. accelerations, velocities and displacements, may be obtained by solving the equations of motion by only knowing the external excitation and its modal properties. Two different numerical methods have been implemented in this work.

The first one is the classical *Newmark method*, an implicit time integration scheme. The formulas are recalled here:

$$\dot{q}_{t+\Delta t} = \dot{q}_t + [(1-\delta)\ddot{q}_t + \delta\ddot{q}_{t+\Delta t}]\Delta t \tag{4.5}$$

$$q_{t+\Delta t} = q_t + \dot{q}_t\Delta t + [(1/2-\alpha)\ddot{q}_t + \alpha\ddot{q}_{t+\Delta t}]\Delta t^2 \tag{4.6}$$

Where q_t, $\dot{q}_t$ and $\ddot{q}_t$ are the displacement, velocity and acceleration respectively, at a given time t. δ and α are two coefficients that take different values depending if a constant acceleration ($\alpha = 1/4$, $\delta = 1/2$) or a linear acceleration ($\alpha = 1/6$, $\delta = 1/2$) is considered. It can be shown that Newmark is unconditionally stable and non-dissipative, if a constant acceleration is used. Whereas, in the case of a linear acceleration, it is conditionally stable. Therefore, the first one is chosen. Relations (4.5) and (4.6) are then introduced in the equation of motion at time $t + \Delta t$:

$$m\ddot{q}_{t+\Delta t} + c\dot{q}_{t+\Delta t} + kq_{t+\Delta t} = p_{t+\Delta t} \tag{4.7}$$

The solution is then computed iteratively by starting from $\ddot{q}_{t+\Delta t}$, then using (4.5) and (4.6) to obtain $\dot{q}_{t+\Delta t}$ and $q_{t+\Delta t}$. For the last step, equation (4.7) is used to obtain a new value of the iterate $\ddot{q}_{t+\Delta t}$.

Depending on the chosen time step Δt, there may be a period elongation, which can distort the results. To avoid this, the ratio time step over the structure's period $\Delta t/T_1$ should be smaller than 0.10. Note that this method can be extended to solve non-linear problems or can be rewritten as an explicit scheme. For more details, the reader may refer to [13] and [61].

The second method uses the *discrete-time state-space form of the equation of motion in the modal basis* obtained in chapter 2:

$$\mathbf{x}_{[k+1]} = \mathbf{A}\mathbf{x}_{[k]} + \mathbf{B}\mathbf{p}^*_{[k]} + \mathbf{w}_{[k]}$$

where the only unknown is the modal state vector $\mathbf{x}_{[k]}$, as $\mathbf{p}^*_{[k]}$ can be defined by (4.4). The system matrices $\mathbf{A}$ and $\mathbf{B}$ are defined in chapter 2 and given by (2.28) and (2.29). The modal state vector's initial value is assumed to be equal to zero. As a reminder the modal state vector at instant k is defined as

$$\mathbf{x}_{[k]} = \begin{pmatrix} \mathbf{q}_{[k]} \\ \dot{\mathbf{q}}_{[k]} \end{pmatrix}$$

The acceleration is calculated in a subsequent step by a simple centred finite difference:

$$\ddot{\mathbf{q}}_{[k]} = \frac{\dot{\mathbf{q}}_{[k-1]} + \dot{\mathbf{q}}_{[k+1]}}{2\Delta t} \tag{4.8}$$

4.3 First test case

The first case is based on the application example used in K. Van Nimmen et al. "Inverse identification of pedestrian-induced loads" [44]. Where a single pedestrian walks over a laboratory structure, which consists of a 7m long, hollow-core pre-stressed and simply-supported concrete slab. In that work, the measurements are done by using 13 accelerometers and one optical displacement sensor, which are placed as shown in figure 26.

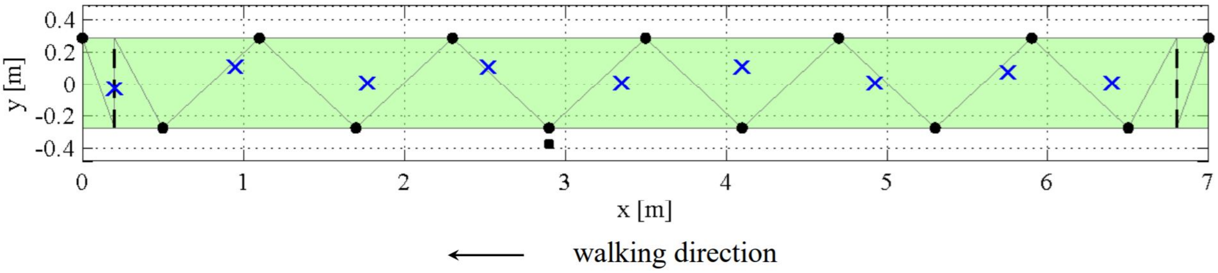

Figure 26: Measurements set up: accelerometers (●), optical displacement sensor (■), line supports of the slab (− −) and identified footstep locations (x). [44]

4.3.1 Definition of the parameters

Several parameters must be given as input in the algorithm, most of them are clearly stated in [44]. These are:

- the modal properties of the structure, where the two first modes could be identified, as shown in figure 27.

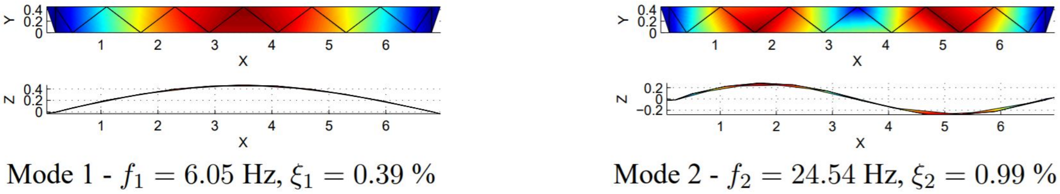

Figure 27: First two modes of the laboratory structure (f_i and ξ_i are the natural frequencie and the damping ratio corresponding to mode i) [44].

  However only the modes in the frequency range of 0Hz to 20Hz are considered ie. only the first one.

- The sensors attached to the pedestrian registered his motion which allows the identification of his average step frequency found to be $f_s = 1.98$Hz,
- the sampling step is $\Delta t = 0.01$s,
- the noise covariance matrix of the process and measurement noise vectors is taken equal to $\mathbf{S} = \mathbf{0}$,
- $n_{d,a} = 13$ accelerations and $n_{d,d} = 1$ displacement are considered with coordinates that can be read from figure 26,
- and as already mentioned, the slab's length is $L = 7$m.

- The initial state estimate vector $\hat{\mathbf{x}}_{[0|-1]}$ and the corresponding error covariance matrix $\mathbf{P}_{[0|-1]}$ are both considered equal to zero. This remains maintained for all following applications

Regarding the measures, we do not directly have access to them. All that is given in [44] is a graph of the accelerations as a function of time at the midspan, indicating that the duration of the measurements is 50s. Additionally, a graph of the identified modal loads is also given It shows that the pedestrian walks on the structure for a duration of approximately t =4s and therefore has a speed of $v_s = 1.75$m/s.

Following the procedure presented in section 4.1, the modal load for the first mode of a shape $\Phi(x) = \sin\left(\frac{\pi x}{L}\right)$ is given by equation (4.4) and yields:

$$p_1^*(t) = F(t)\sin\left(\frac{\pi v_s t}{L}\right) \tag{4.9}$$

where, $F(t)$ is the vertical pedestrian load defined by (4.1).

Two assumptions must be made concerning the pedestrian's and the slab's weight, as these are not given. The pedestrian's weight is assumed to be equal to 600N. For the slab, we do know that it is a hollow-core concrete slab and its mass density of 1909 kg/m^3 is given. Its weight is assumed to be equal to 900kg or 128.57kg/m. The modal mass is defined as:

$$M^* = \int_0^L \mu\Phi^2(x)dx = \frac{\mu L}{2} \tag{4.10}$$

and is equal to 450kg.

Following the guidelines of Sétra [1], the Fourier coefficients appearing in the definition of the vertical dynamical load are chosen equal to $\alpha_1 = 0.4$ and $\alpha_2 = \alpha_3 \simeq 0.1$, which are those proposed by Bachmann et al. from table 11. Note that these values are for a step frequency of 2Hz, which is not the step frequency in this case ($f_p = 1.98Hz$), but it is close enough to be considered as acceptable.

The vibrational response is simulated by using the second method presented in section 4.2, based on the discrete-time state-space form of the equation of motion. One reason for this choice is because it is easier to add noise and analyse its impact on the results of the impact. There is a second reason, which will be clarified when comparing both methods in the next section 4.3.2.

In the first place, the noise is neglected or at least considered very small. Only in the section where its influence is analysed, it is taken into account, by adding a process noise vector $\mathbf{w}$ to the state vector $\mathbf{x}$ and a measurement noise vector $\mathbf{v}$ to the data vector $\mathbf{d}$. These are calculated based on the standard deviation of the state and data vector. The corresponding noise covariance matrices $\mathbf{Q}$ and $\mathbf{R}$ are obtained accordingly.

4.3.2 Discussion of the results

Before showing the results obtained by applying the joint input-state estimation algorithm to this first case, notice that in contrast to the accelerations used in [44], those used here are simulated, as we do not have the measured ones. It implies that there may already be some numerical errors on the vibrational response, before running the algorithm. Even if a natural frequency of 6.05Hz is used for the first mode as mentioned in the paper, after simulating the accelerations and doing the fast Fourier transform, the value of the natural frequency identified here is slightly different (6.059Hz). This error can be reduced by decreasing the time step and depends on the method used to obtain the vibrational response. The accelerations simulated at midspan of the concrete slab are shown in figure 28. Where after 4s the pedestrian has already crossed the structure and the free response of the structure is observed.

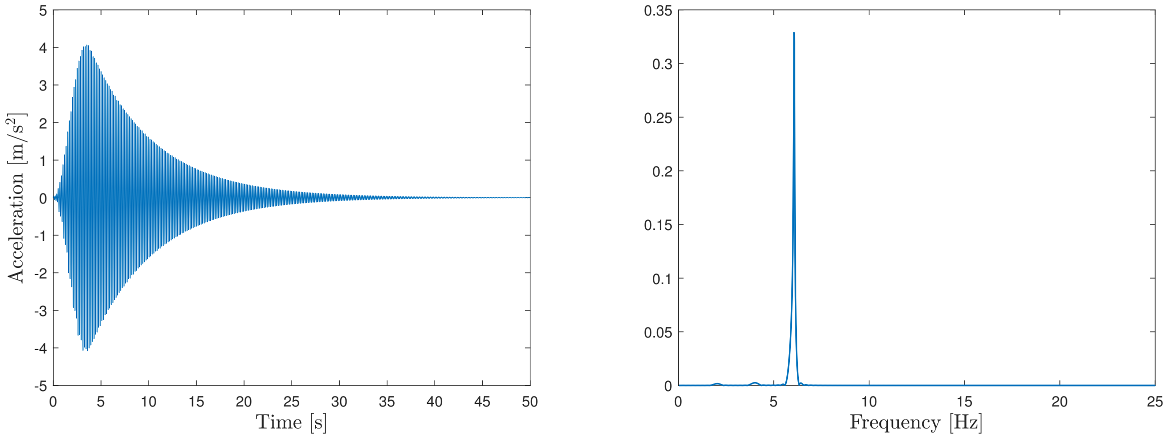

Figure 28: Simulated accelerations as a function of time and its corresponding FFT

The aim here is not only to reproduce the results in [44], even if this allows to validate the joint input-state estimation algorithm and it ensures thereby that it has been well implemented. This test case enables also to analyse the influence of various parameters, like the number of measurements taken into account, a modification of the time step, addition of noise and the number of modes taken into account. Which will help to identify the limitations of the algorithm and verify the applicability conditions mentioned in section 2.4 of chapter 2.

Influence of the number of measurements

The output vector d of the algorithm contains the different measurements, such as $n_{d,a}$ accelerations, $n_{d,v}$ velocities and/or $n_{d,d}$ displacements. As in [44], 13 accelerations and one displacement are used, the results obtained are shown in figure 32 and are in agreement with those of the paper. The modal load given by the algorithm is not too far from the exact one. However, if only 13 accelerations are used as for figure 29, the obtained modal load is not correct, the static component is missing. In fact, by using only accelerations, the algorithm does not capture very well the low frequencies, as shown in the corresponding Fourier transform. By adding one (figure 30) or even 13 velocities (figure 31), the results are improved but are still worse than those obtained with an added displacement. This was already expected, according to what is mentioned in section 2.4 about the applicability conditions. As a reminder, accelerations and velocities are insensitive to a constant load, such as the constant component of the pedestrian load. Thus, by keeping all the other parameters presented in section 4.3.1 unchanged, at least one displacement is needed to ensure the stability of the algorithm as well as the uniqueness of the results.

In any case, the algorithm can be used to identify the dynamic component of the pedestrian load, as shown in figure 33. Which is the most interesting for designing a footbridge since it is the source that can cause vibration problems. Notice that the identified modal load still do not perfectly match the exact one, but this will be explained and improved in the second test case.

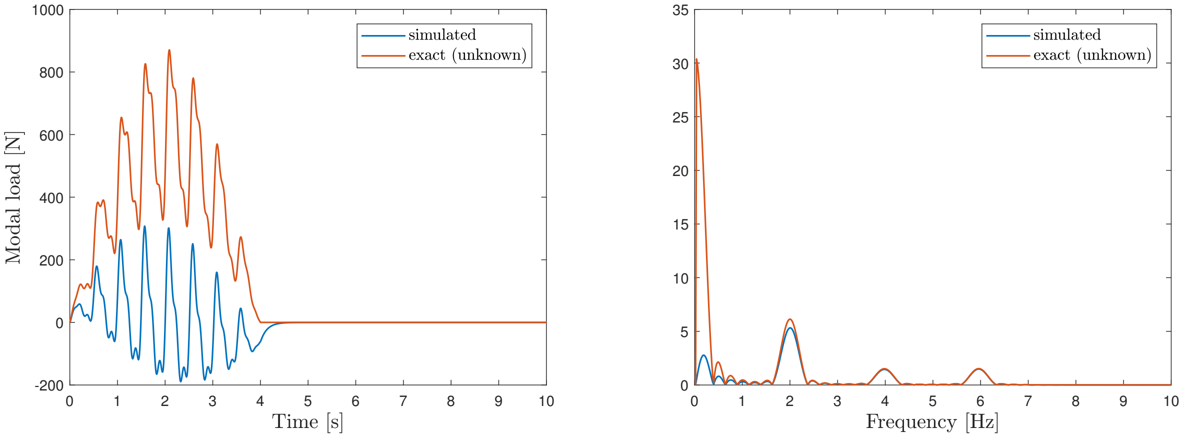

Figure 29: Simulation based on 13 observations (accelerations only) for the first mode with a sampling step of Δt=0.01s and its corresponding FFT

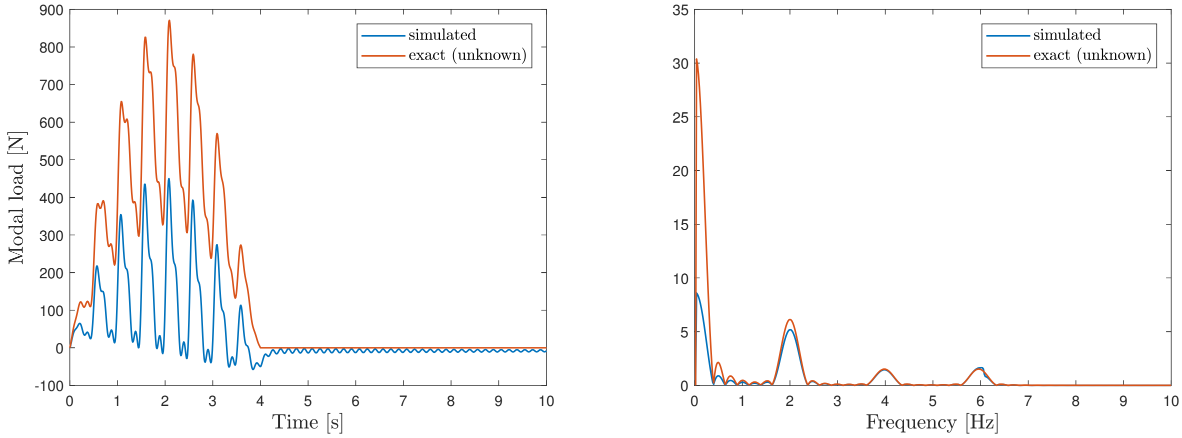

Figure 30: Simulation based on 14 observations (13 accelerations and 1 velocity) for the first mode with a sampling step of Δt=0.01s and its corresponding FFT.

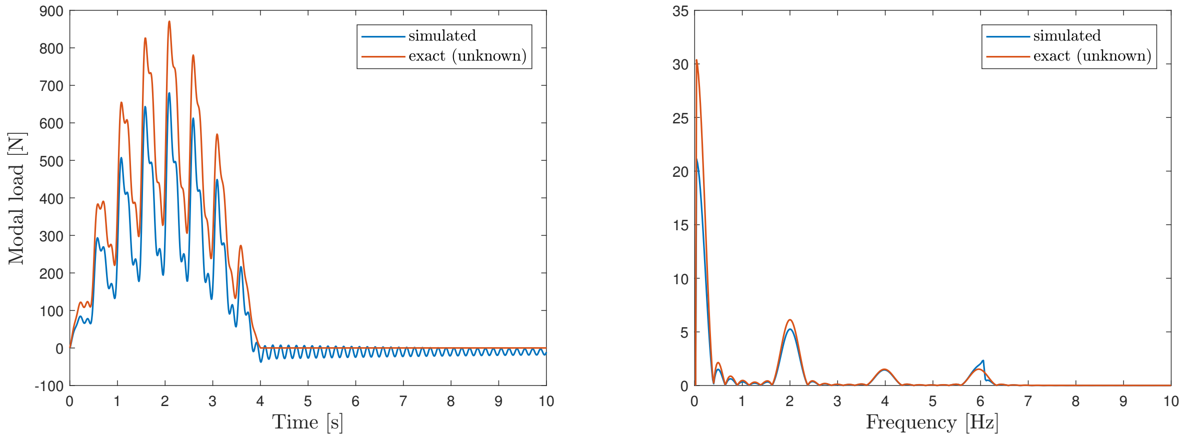

Figure 31: Simulation based on 26 observations (13 accelerations and 13 velocities) for the first mode with a sampling step of Δt=0.01s and its corresponding FFT.

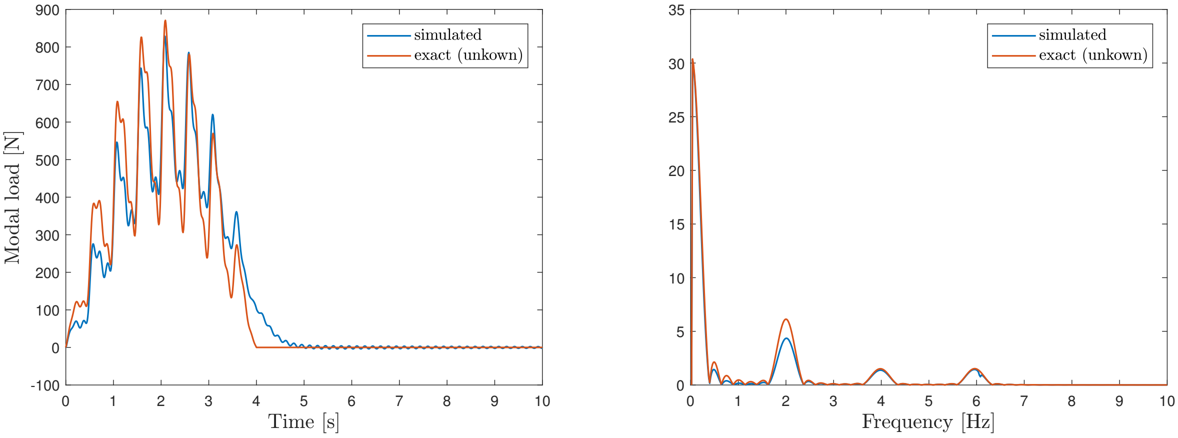

Figure 32: Simulation based on 13 observations (13 accelerations and 1 displacement) for the first mode with a sampling step of Δt=0.01s and its corresponding FFT.

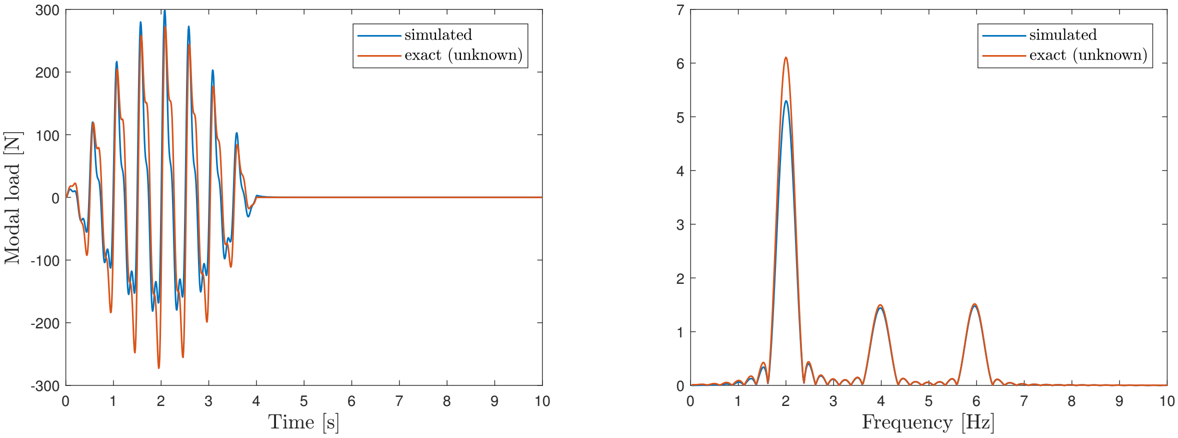

Figure 33: Simulation of the dynamical load component based on 13 observations (accelerations only) for the first mode with a sampling step of Δt=0.01s and its corresponding FFT.

Influence of the time step

Since it is not always possible to measure a displacement for real world footbridges, it is interesting to analyse if it is possible to improve the results by keeping only accelerations as measurements, but by decreasing the sampling step Δt. As shown through figures 34, and 35, the results can indeed be improved. By decreasing the sampling step the ratio period T_1 over the sampling step Δt increases from approximately 16.53 by the same factor 10^4. This means that per period there will be much more points containing useful information.

However, notice that the sampling step has to be significantly decreased, which comes with other problems like an increase of the simulation time. Moreover, the accelerometers may not be able to record at such small sampling step.

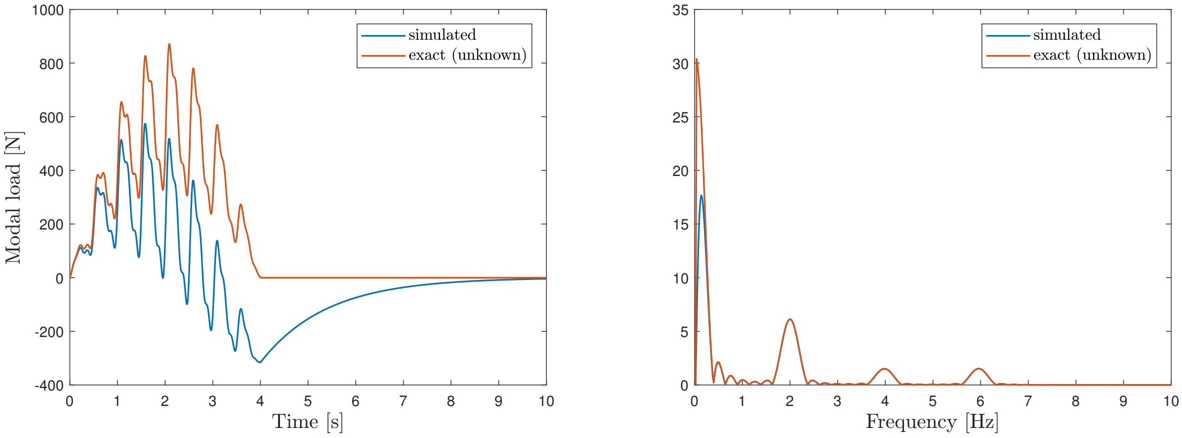

Figure 34: Simulation based on 13 observations (accelerations only) for the first mode with a sampling step of Δt=0.001s and its corresponding FFT

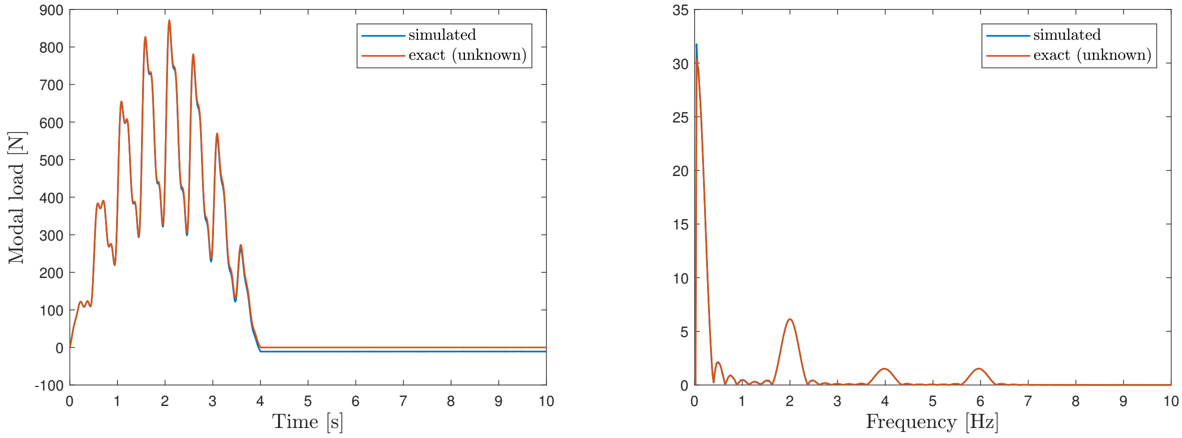

Figure 35: Simulation based on 13 observations (accelerations only) for the first mode with a sampling step of Δt=0.00001s and its corresponding FFT

Influence of noise

As mentioned in section 2.2 of chapter 2, the state-space model takes noise into account by adding a measurement noise vector $\mathbf{v}$ to the data/output vector $\mathbf{d}$ and a process noise vector $\mathbf{w}$ to the states vector $\mathbf{x}$. Both are assumed zero mean and white. So far, as the measurements are simulated there is no measurement noise or noise due to stochastic excitation. However, for measurements done on real-world structures, there will be. The influence of noise on the identified modal loads is analysed by adding a maximum noise of 0.25% and 5% of the standard deviation of the states and data vector. As a reminder, the noise covariance matrices $\mathbf{Q}$ and $\mathbf{R}$ are defined as:

$$\mathbf{Q} = \mathbb{E}\left[\mathbf{w}_{[k]}\mathbf{w}_{[l]}^T\right]\delta_{[k-l]}$$

and

$$\mathbf{R} = \mathbb{E}\left[\mathbf{v}_{[k]}\mathbf{v}_{[l]}^T\right]\delta_{[k-l]}$$

It can be seen from figures 36 and 37, that even with heavily noisy measurements, the algorithm is able to correctly identify the modal load. This confirms the advantage of this inverse technique compared to others, it deals very well with noise.

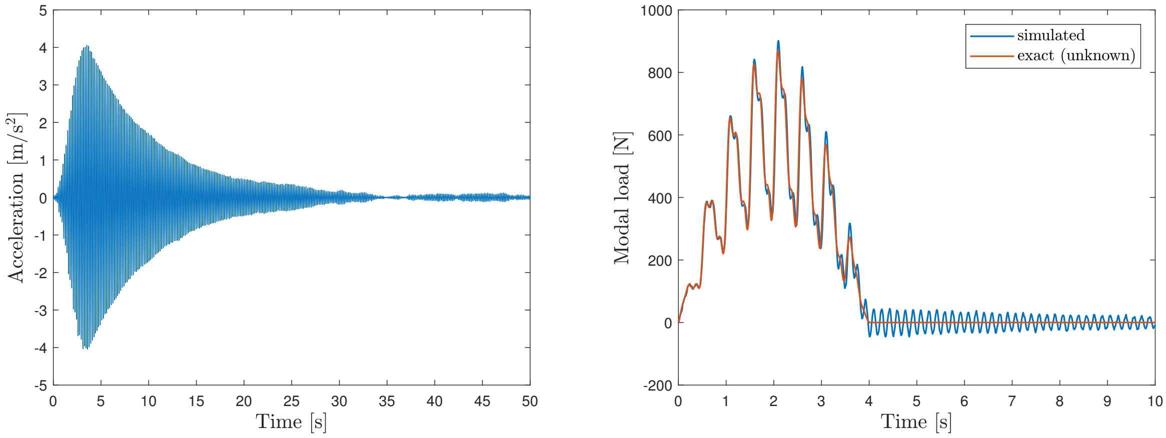

Figure 36: Simulation based on 14 observations (13 accelerations and 1 displacement) for the first mode with a sampling step of Δt=0.01s and 0.25% noise.

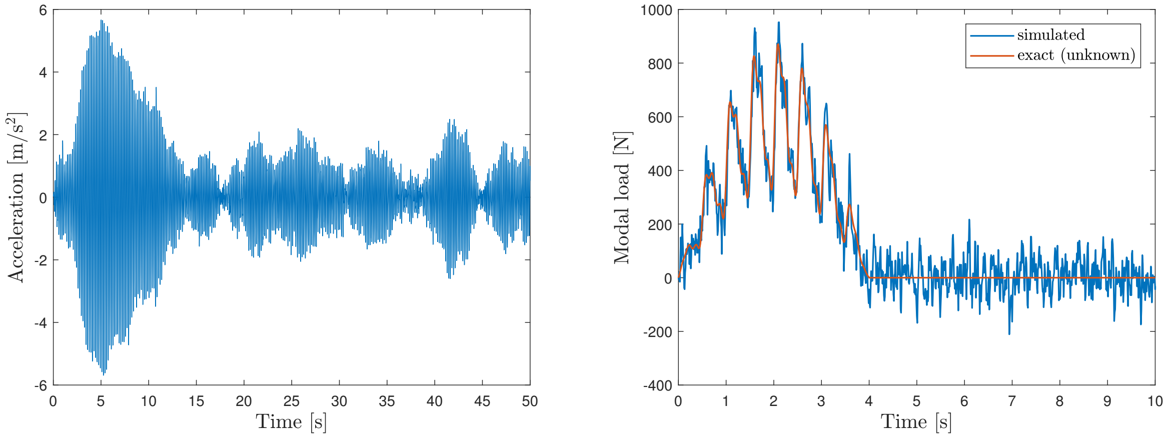

Figure 37: Simulation based on 14 observations (13 accelerations and 1 displacement) for the first mode with a sampling step of Δt=0.01s and 5% noise.

Influence of the number of modes taken into account

The algorithm is able to take into account an arbitrary number of modes n_m. In this case, we only have information about the first two. The identified modal loads based only on accelerations are shown in figure 38. The results for the first mode are slightly improved compared to those obtained previously by also using only accelerations. However, they are still far from satisfactory.

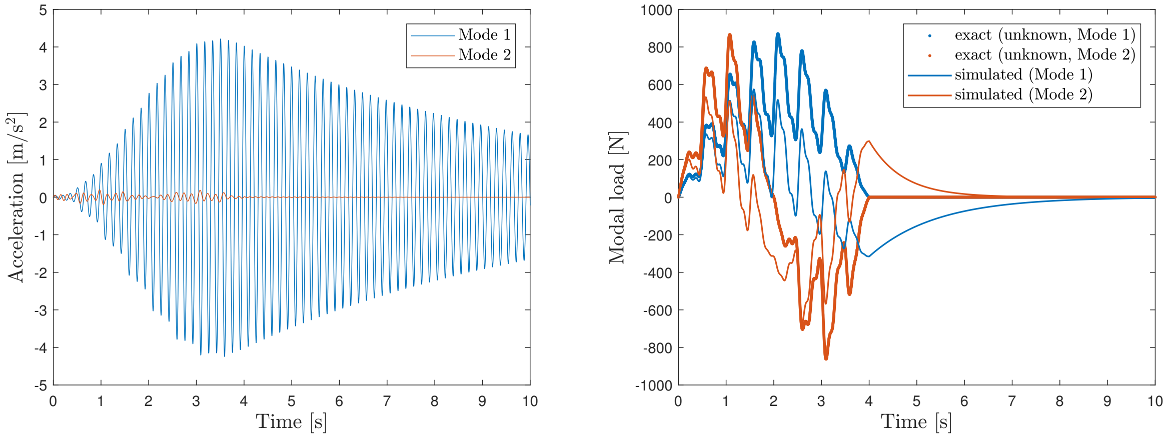

Figure 38: Simulation based on 13 observations (accelerations only) for the first two modes with a sampling step of Δt=0.001s.

4.3.3 Impact of a frequency error on the modal forces

The natural frequencies of the Geierlay are obtained based on experimental data acquisition. Thus there may be errors in the identified values. Chapter 3, already shows that the values slightly change from set to set and are slightly different from those given by the model of the footbridge. For this reason, it is interesting to analyse the impact a frequency error might have on the modal load. At the same time, both methods presented in section 4.2 to obtain the vibrational response of the structure are compared, by documenting the impact of frequency errors for each method. The impact is quantified by using the L2 relative error norm, given by:

$$\text{Relative error} = \sqrt{\frac{\sum_{i=1}^{n}(p_{fft,i} - \hat{p}_{fft,i})^2}{\sum_{i=1}^{n} p_{fft,i}^2}} \tag{4.11}$$

where $p_{fft,i}$ is the FFT of the exact pedestrian load obtained by the single-pedestrian loading model presented in chapter 4 and $\hat{p}_{fft,i}$ is the FFT of the simulated load given by the algorithm. An error of -1Hz and +1Hz compared to the exact frequency value of 6.05Hz for the first mode is analysed.

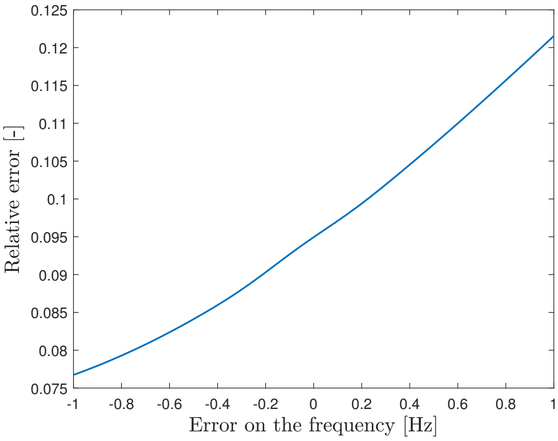

Figure 39: Method based on the discrete-time state-space form of the equation of motion (method 1)

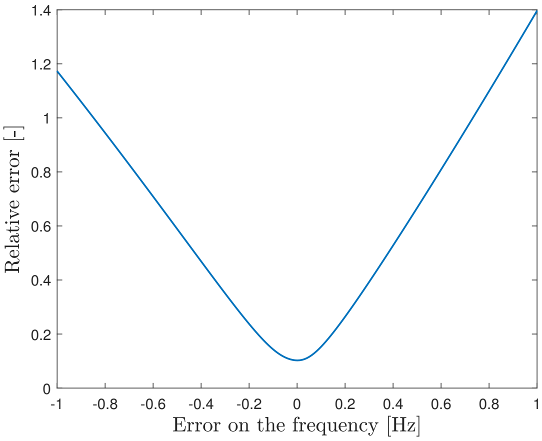

Figure 40: Newmark method (method 2)

The relative error on the FFT of the modal load is shown in figure 39 by using the method based on the discrete-time state-space form of the equation of motion. And in figure 40, by using the Newmark method. As can be seen on the y-axis, the error committed increases much faster for the Newmark method. This is directly visible in figures 41 and 42, showing the modal load and its corresponding FFT for three different frequency values. By using method 1, the error can be considered negligible. Thus this method will be used when applying the algorithm to the second test case, where the modal properties of the Geierlay footbridge will be used.

Notice that for the Newmark method, instability is observed. This is because the criteria of a ratio $\Delta t/T_1 < 0.10$ is not respected. This can be avoided by decreasing the sampling step, which is not always possible if the measured accelerations have been recorded with a fixed sampling step.

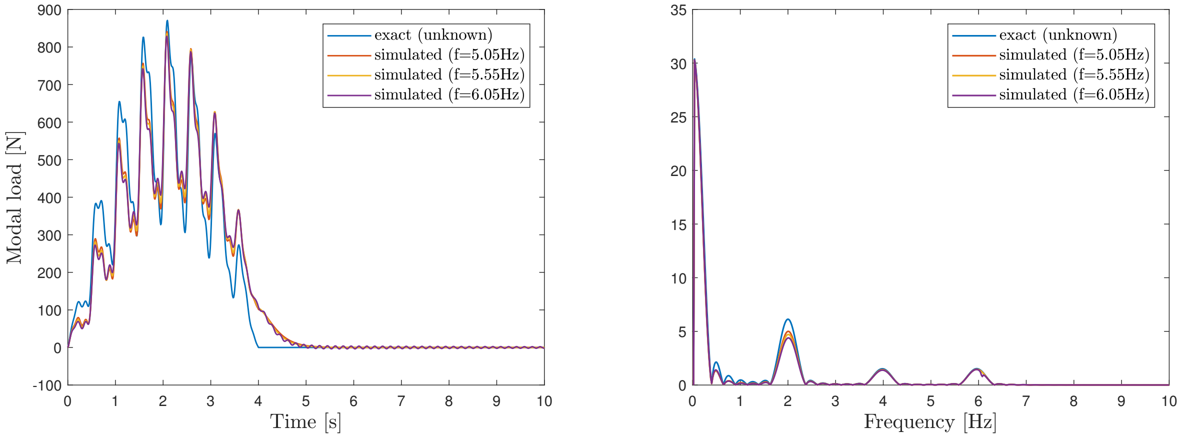

Figure 41: Impact of a frequency error on the modal load and its corresponding FFT by using method 1

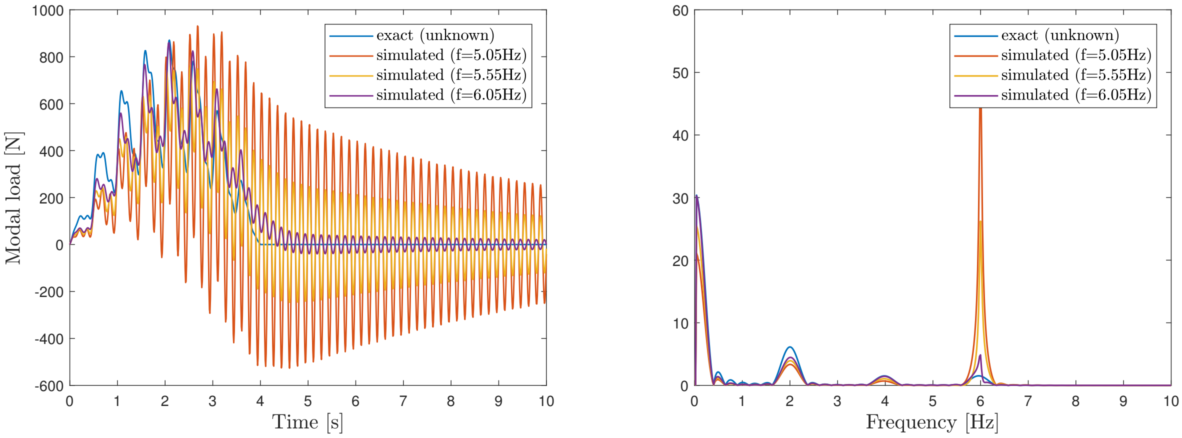

Figure 42: Impact of a frequency error on the modal load and its corresponding FFT by using method 2

4.3.4 Impact of a damping ratio error on the modal forces

The same analysis can be done for a damping ratio error, as this modal property is also identified based on the measurements and is thus not very precise. The impact is quantified by applying the same L2 relative error norm on the FFT of the identified modal load, given by equation (4.11). An error of -0.30% to +0.30% compared to the exact value of 0.39% for the first mode is considered.

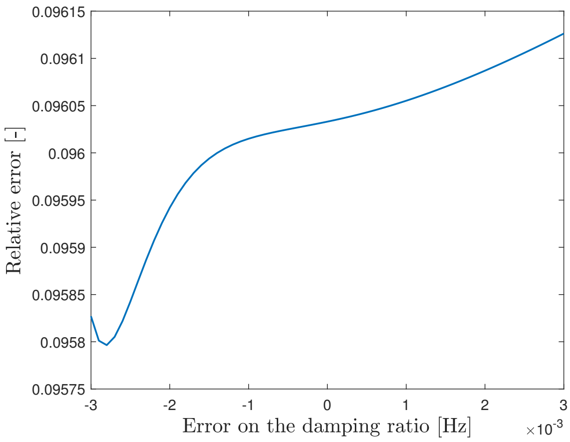

Figure 43: Method based on the discrete-time state-space form of the equation of motion (method 1)

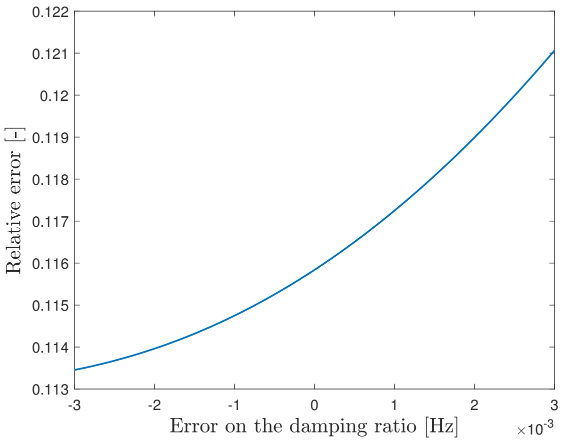

Figure 44: Newmark method (method 2)

The relative error on the FFT of the modal load is shown in figure 46 and 44 for both methods. Here again, the method based on the discrete-time state-space form of the equation of motion is less influenced by an error and the impact can be considered negligible. Even if the impact is higher for the Newmark method it stays small and the relative error increases slower as for a natural frequency error. This is clearly shown in figures 45 and 46, were the differences for the various values are almost not visible.

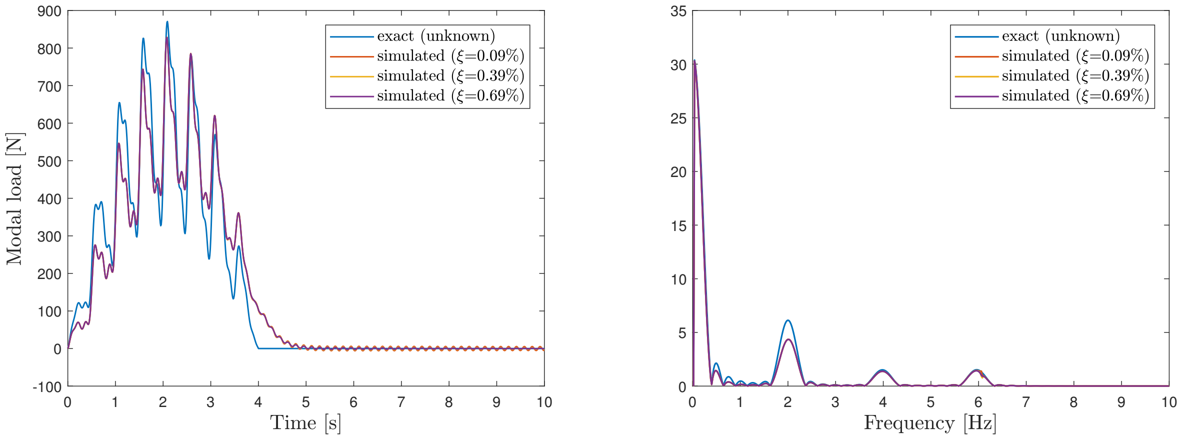

Figure 45: Impact of a damping error on the modal load and its corresponding FFT by using method 1

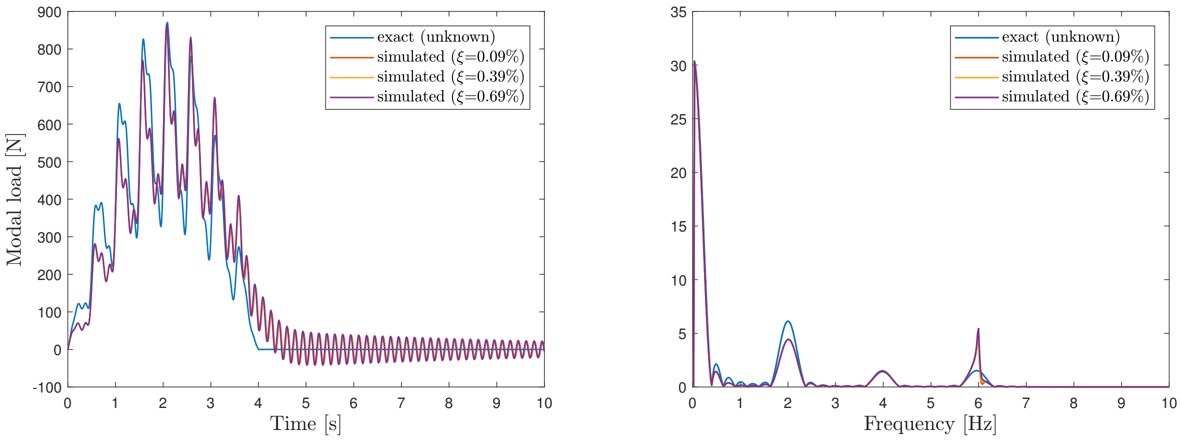

Figure 46: Impact of a damping error on the modal load and its corresponding FFT by using method 2

This analysis, therefore, does not change the choice made above, which is to use the method based on the discrete-time state-space form of the equation of motion for the second test case.

4.4 Second test case

The second test case is the extension of the former, by adjusting for the Geierlay's geometric features and modal properties. A brief description, as well as the identification of the modal properties of the footbridge, are already given in chapter 3.

4.4.1 Definition of the parameters

Based on what is presented in chapter 3, the following information is given as input in the algorithm:

- The first vertical modes are defined by the following natural frequencies: $f_1 = 0.42$Hz, $f_2 = 0.56$Hz and $f_3 = 0.63$Hz.
- The damping ratios have been identified based on the accelerations under pedestrian load. It was not possible to identify the damping ratio corresponding to each mode, however as shown in the analysis carried out in section 4.3.4, the identified modal load is little influenced by the damping ratio value taken into account. Thus a value of $\xi = 1.4\%$ is considered here.
- The footbridge's length is equal to $l = 363.9$m,
- and knowing that a pedestrian needs approximately 9 minutes to cross the footbridge, it's velocity is $v_s = 363.9/540 \simeq 0.67$m/s.
- The generalised mass of the footbridge are taken from [42] and for the first three modes are equal to $M_1^* = 27.57$T, $M_2^* = 37.12$T and $M_3^* = 33.37$T.
- Only $n_{d,a} = 4$ accelerations are considered here, corresponding to the number of accelerometers used for the experimental campaign. Additionally, their coordinates are taken equal to the locations where the sensors were placed. These are given in

chapter 3. This allows already to get as close as possible to the data that will be used when the algorithm is applied to the real footbridge.

The other parameters are defined as for the first test case, to allow a better comparison between both test cases. Thus, the step frequency is kept equal to 1.98 Hz, the pedestrian's weight is 600N and the sampling step is 0.01s. The influence of noise has already been analysed and is therefore no more taken into account here.

The vibrational response is calculated following the procedure based on the discrete-time state-space form of the equation of motion, which is described in section 4.2 and by using the dynamical load factors suggested by Bachmann et al.

4.4.2 Discussion of the results

The simulated accelerations are given in figure 47. This time we clearly see that the amplitude increases when the pedestrian walks to the footbridge's midspan, where the maximum is reached and decreases when he walks away.

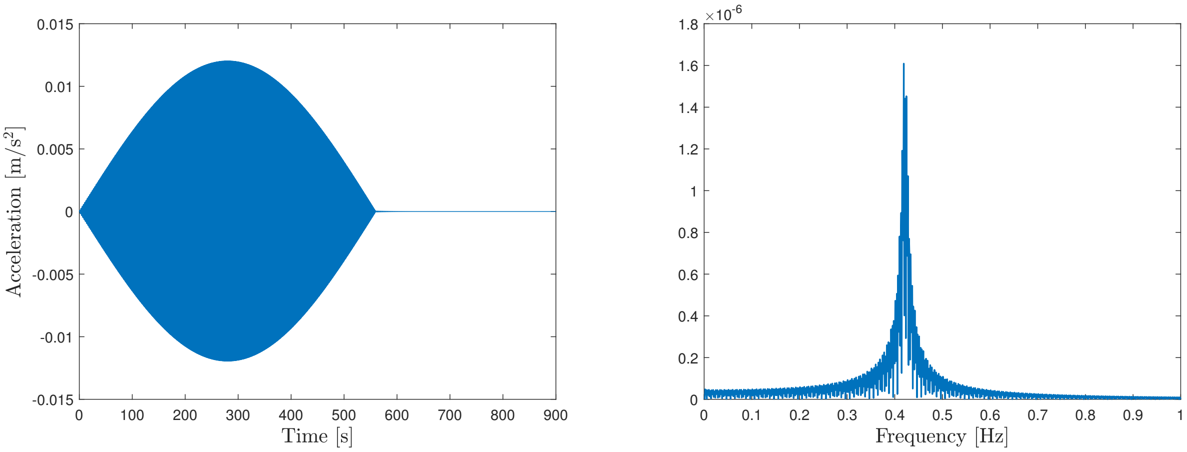

Figure 47: Acceleration as a function of time and its corresponding FFT

The aim of this second test case is not to analyse again the influence of the several parameters, but rather to verify that there are no major complications that might stem from non-idealised parameters as opposed to the laboratory conditions of the previous test case. As shown in figure 48, without any surprise, the algorithm still does not capture the static component of the pedestrian load if only accelerations are used in the data vector d. However, this time the modal load is already very well identified by only adding one velocity as proven by figure 49. This can be explained by the difference of the two ratios $\frac{T_1}{\Delta t}$ and $\frac{T_{cross}}{T_1}$, where T_1 is the structures period for the first mode, which is equal to the inverse of its natural frequency in this same mode, Δt is the sampling step and T_{cross} is the time necessary for one pedestrian to cross the structure. Their numerical values are given in table 14.

	1st test case	2nd test case
$\frac{T_1}{\Delta t}$	$\frac{1/6.05}{0.01} \simeq 16.53$	$\frac{1/0.42}{0.01} \simeq 238.10$
$\frac{T_{cross}}{T_1}$	$\frac{4}{1/6.05} = 24.20$	$\frac{540}{1/0.42} = 226.80$

Table 14: Comparison of the ratios $T_1/\Delta t$ and T_{cross}/T_1 for both test cases

The ratio $T_1/\Delta t$ indicates that for the second test case, there are approximately 14 times more measured points per period. Additionally, according to the ratio T_{cross}/T_1 there are approximately 9 times more oscillations measured during the excitation of the second case which lasts longer. Thus there is much more information for the second test case, which improves considerably the modal load identification.

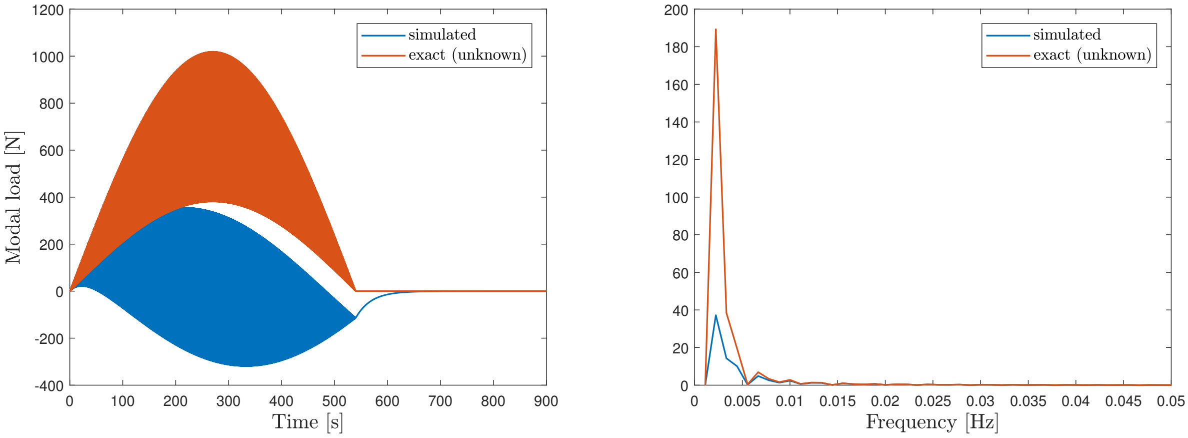

Figure 48: Simulation based on 4 observations (accelerations only) for the first mode with a sampling step of Δt=0.01s and a zoom of its corresponding FFT.

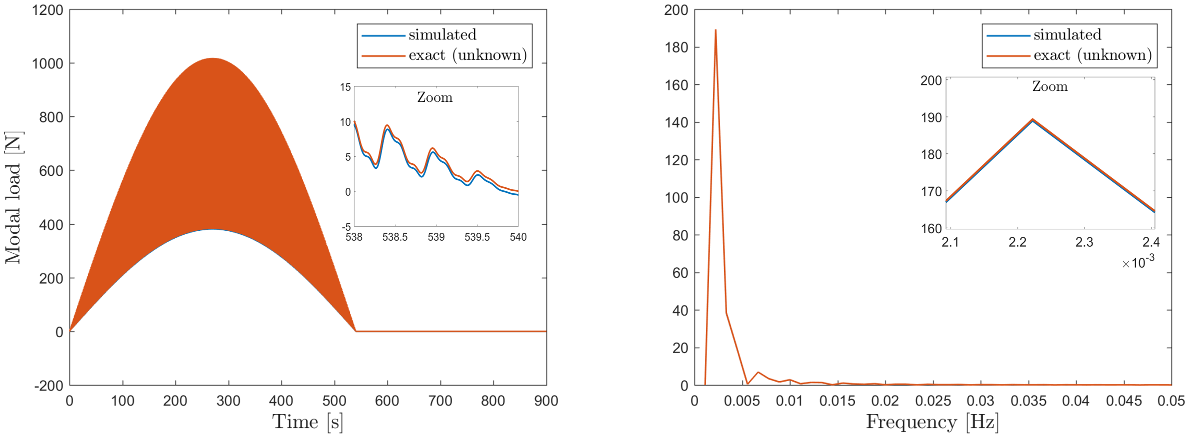

Figure 49: Simulation based on 5 observations (4 accelerations and 1 velocity) for the first mode with a sampling step of Δt=0.01s and a zoom of its corresponding FFT.

As already discussed, only accelerations have been measured on the real world footbridge. Thus we will only be able to correctly identify the dynamical pedestrian load component.

Which are for the same reasons stated above improved compared to the first test case, as shown in figure 50. This is good news since this test case is closer to reality and confirms that the joint input-state estimation algorithm can be applied to the Geierlay footbridge to identify the dynamical pedestrian load, which is the purpose of this work.

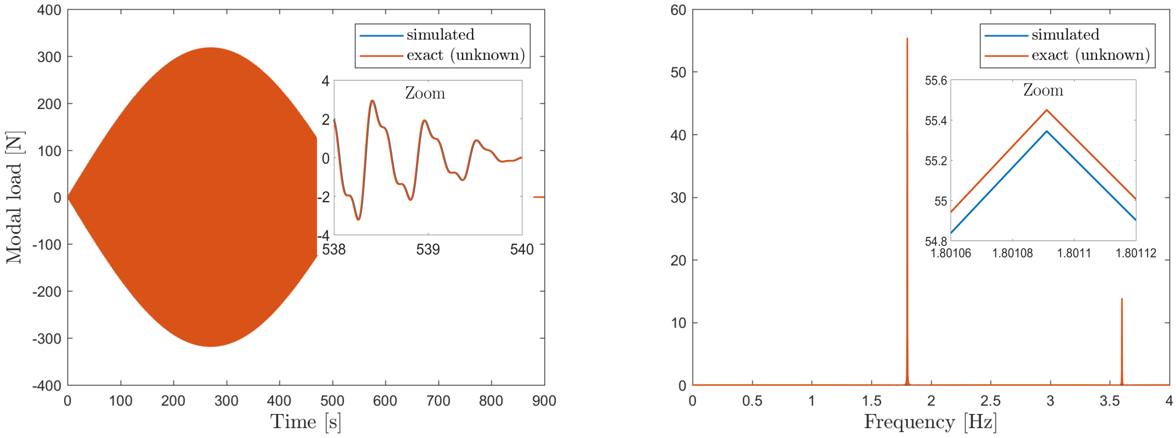

Figure 50: Simulation of the dynamical load component based on 4 observations (accelerations only) for the first mode with a sampling step of Δt=0.01s and its corresponding FFT.

4.5 Limitations of the algorithm

As can be seen from the various results presented in this chapter, the algorithm doesn't work always very well. At least one displacement is needed to allow correct identification of the modal load, as already mentioned in chapter 2. Otherwise only the dynamical load component can be identified. This is usually not a problem in civil engineering. Most of the time a displacement can easily be measured and when this is not the case, the dynamical component is often already very useful.

If possible a ratio $T_1/\Delta t$ and T_{cross}/T_1 of the order 100 should be taken for accurate results.

Additionally, the measurement noise vector $\mathbf{v}$ can not be taken equal to zero to avoid singular matrix problems. The corresponding noise covariance matrix $\mathbf{R}$ appears directly in the first equation of the input estimation step of the algorithm which defines $\tilde{\mathbf{R}}$ by:

$$\tilde{\mathbf{R}}_{[k]} = \mathbf{G}\mathbf{P}_{\mathrm{x}[k|k-1]}\mathbf{G}^{\mathrm{T}} + \mathbf{R}$$

and the reverse of which is then taken. Thus, by initiating the covariance matrix of the state estimate error $\mathbf{P}_{\mathbf{x}[0|-1]}$ also too zero, $\tilde{\mathbf{R}}$ is close to a zero matrix. This problem does not occur when the process $\mathbf{v}$ noise is taken equal to zero. However, when the algorithm is applied by using measurements carried out on a real structure, there will always be measurement noise.

Chapter 5

Algorithm applied to the Geierlay footbridge

The final step of this work is to apply the joint input-state estimation algorithm to a real-world example, the Geierlay footbridge. But first, a reminder of existing loading models for a group of pedestrians or a crowd is given. As explained in chapter 3, during the data acquisition, there were groups of people crossing the bridge and not a single pedestrian as assumed for the validation test cases. The obtained results are then compared to these loading models and if necessary some improvements are proposed.

5.1 Loading models for a group of pedestrians or a crowd

In contrast to the single-pedestrian loading models, which were presented in section 4.1, loading models for a group of pedestrians or a crowd are not well defined. Current knowledge of the behaviour of multiple pedestrians crossing a structure is limited and there is still progress to be made. The difficulty comes from the wide variety of parameters that are not easy to predict or simulate. Thus tests have to be done by simulating a crowd, where each pedestrian may have a different step frequency, velocity and self-weight. One may also take into account the initial phase change between the pedestrians entering at different moments on the bridge. Additionally, the pedestrians might more or less synchronise with each other or with the footbridge. The first synchronisation type depends on the pedestrian's frequency, his velocity and the number of pedestrians on the footbridge. It is favoured by a larger number. The second type, also called the 'lock-in' phenomenon, depends additionally on the frequency of the bridge as well as the amplitude of its motion, as mentioned in [2]. This happens when an initially random crowd feels the motion of the footbridge and to compensate this feeling of imbalance they gradually adopt the footbridge's frequency and become in phase with its motion. This creates a resonance problem that amplifies at the beginning due to a crowd synchronisation. Once the motion is sufficiently large to prevent the pedestrians from walking the phenomenon attenuates. So far, the lock-in effect has only been observed for lateral movements, since in the vertical direction pedestrians can counterbalance the motion with their knees for example.

There are several footbridges which on their inauguration day started to move so much that it affected the comfort of pedestrians. This proves that they have not been correctly designed for a crowd. A well-known example is the *Millennium* footbridge in London.

During its opening day in June 2000, the bridge faced a transverse lock-in phenomenon and needed to be closed two days later. Investigations have been done and several dampers were added, before reopening almost two years later. Another example is the *Léopold-Sédar-Senghor* footbridge in Paris, or better known as the *Solférino* bridge before it was renamed in 2006. It opened in 1999 and suffered from the same phenomenon. Further information on these footbridges can be found in [24]. One last example cited here is *La Belle Liègeoise* in Liege shown in figure 51. During its inauguration day in May 2016, there was also an event nearby at the end of which everybody crossed the footbridge at the same time. This again caused a lateral lock-in phenomenon. Several tests have been done after that with a group of approximately 80 pedestrians running or walking, however no accelerations out of the ordinary have been observed. Thus, the conclusion was that the synchronisation only occurs for an exceptionally dense crowd and since this is very rare, the project owner decided not to add additional dampers.

Figure 51: Belle Liègeoise footbridge (Liège, Belgium)

As seen above, it is always a problem of comfort and not of resistance, that may occur during exceptional events like an inauguration. However, the investigations and modifications on the footbridge that need to be made afterwards are time-consuming and expensive. Thus they should be avoided. Several loading models have already been proposed, each having its advantages and limitations.

Initially, footbridges were designed based on single pedestrian models and by adding several requirements concerning its stiffness and natural frequencies. As one may imagine, this is not the optimal way to proceed.

A well-known loading model was suggested by Bachmann and Ammann [6], derived from the research of Matsumoto et al. [36], it consists in multiplying the dynamical load due to a single pedestrian[1] by an enhancement factor k based on the Poisson distribution of the arrival probability. It is defined as:

$$k = \sqrt{\lambda T} \tag{5.1}$$

where λ is the rate at which the pedestrians enter the footbridge and is given in persons per second over the deck's width. For reasons of space, the maximum value is approximately taken equal to 1.5 persons/s m. T is the time needed for one pedestrian to cross the

---

[1] A reminder of single pedestrian loading models is given in section 4.1 of chapter 4.

footbridge and can also be expressed as the total length of the footbridge L divided by a pedestrian's speed v. Thus, the product λT defines the number of pedestrians N on the bridge at a given time. The enhancement factor can be rewritten as $k = \sqrt{N}$. This loading model takes into account an initial phase shift but assumes that each pedestrian crosses the footbridge with the same frequency and speed.

The loading model used in the Sétra guidelines [1] to design footbridges for serviceability consists in representing a random crowd, where each pedestrian has a random phase and frequency by an equivalent number of pedestrians N_{eq} which will have the same effect. These pedestrians are supposed to all have the same frequency and phase. Tests are done using probability calculations and statistical processes to give each pedestrian a random phase and a normally distributed random frequency. This frequency is centred around 2Hz and has a standard deviation of 0.175H. Each pedestrian is assumed to have the same velocity equal to 1.5m/s. After lots of tests, the following relations have been established:

$$N_{eq} = \begin{cases} 10.8\sqrt{N\xi} & \text{for sparse or dense crowd} \\ 1.85\sqrt{N} & \text{for very dense crowd} \end{cases} \tag{5.2}$$

where a crowd is considered sparse if its density is 0.5 pedestrians/m^2, dense if it is 0.8 pedestrians/m^2 and very dense if it is about 1 pedestrian/m^2. N is the number of pedestrians on the footbridge at a given moment and ξ is the critical damping ratio. The N_{eq} pedestrians are then uniformly distributed on the footbridge and the applied load follows the mode shape. They create the same maximum acceleration as the corresponding random crowd. In order to obtain the load created by the crowd, the single pedestrian load is then multiplied by N_{eq} and a reduction coefficient Ψ which depends on the natural frequency of the structure and is shown in figure 52. This coefficient takes into account the probability of resonance effects. It decreases when there is less chance that the step frequency corresponds to a natural frequency of a given mode of the structure. The second peak takes into account the effects of the second harmonic of the crowd.

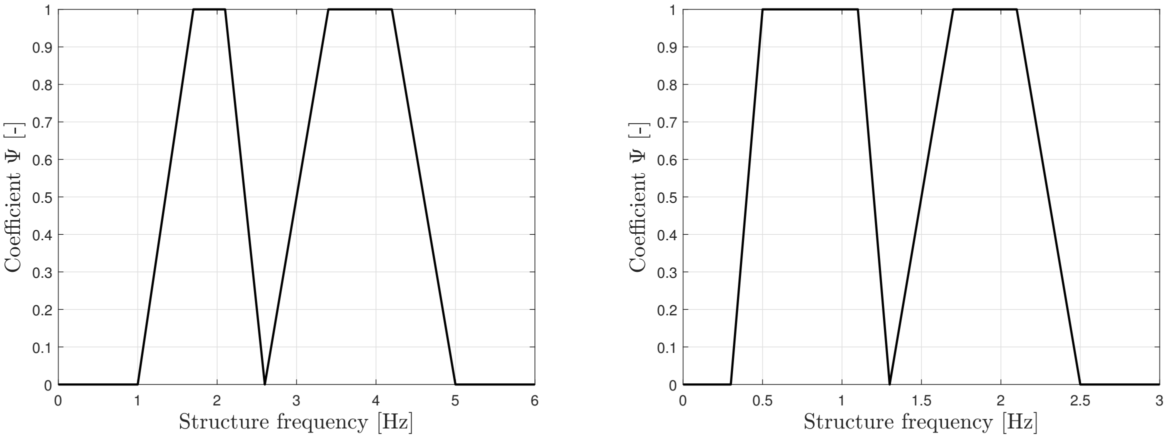

Figure 52: Reduction coefficients for the Sétra loading modal (left: for vertical and longitudinal vibration / right: for lateral vibrations) (adapted from [45])

Fujino et al. [18] suggested a factor for crowd induced lateral forces. Based on tests done on a two-span cable-stayed bridge. They assume that 20% of the crowd on the bridge is synchronised, such that the lateral forces induced by a single pedestrian need to be multiplied by

$$m_F = 0.2N \tag{5.3}$$

to obtain the effects of a group of N pedestrians. As mentioned in [1], several tests show that lateral synchronisation can increase up to 60% or more for a compact crowd and an acceleration higher than 0.1m/s^2.

Another model is given by Ebrahimpour et al. [14] for serviceability design. It is based on experimental measurements done on a large instrumented force platform. They use the general formula for the vertical dynamical load produced by a single pedestrian and define new Fourier coefficients. Depending on the step frequency and the size n of the crowd, where a crowd of 10 pedestrians is considered as large, they assume that once this number is exceeded the coefficient remains constant. The coefficients are summarized in the following table 15:

Frequency [Hz]	Fourier coefficients [-]	
1.5	α_1=0.18 - 0.05log(n)	n≤10
	α_1 = 0.13	n>10
1.75	α_1=0.25 - 0.08log(n)	n≤10
	α_1=0.17	n>10
2.0	α_1=0.34 - 0.09log(n)	n≤10
	α_1=0.25	n>10
2.5	α_1=0.51 - 0.09log(n)	n≤10
	α_1=0.42	n>10

Table 15: Fourier coefficients suggested by [14]

A loading model suggested by Niu et al. [46] for N persons on the bridge is given by:

$$F(x, y, t) = \sum_{j=1}^{N} \delta(x - x_j) \cdot \delta(y - y_j) \cdot \left[W_j + \sum_{i=1}^{n} W_j \alpha_{i,v} \sin(2\pi i f_{jp} t - \varphi_i) \right] \tag{5.4}$$

The last term represents the load induced by the single j-th pedestrian, whose position is given by x_j and y_j. These are defined by: $x_j = x_{0j} + v_{xj}$ and $y_j = y_{0j} + v_{yj}$. The tuple (x_{0j}, y_{0j}) are the coordinates of its initial position and (v_{xj}, v_{yj}) is the velocity in the 2D plane. For this model the position of the pedestrian needs to be known at each time and is given in a cartesian coordinate system with the origin at the center of the deck, the x-axis is parallel to the walkway and perpendicular to the y-axis which is according to the width.

In the field of civil engineering in Europe, the Eurocodes are often used when it comes to dimensioning. However, the footbridges are only briefly mentioned in some sections as:

- EN 1990 A2: Appendix A2 of Eurocode 0 (Basis of structural design) is about applications to bridges and among others to footbridges [54].
- EN 1991-2: The second part of Eurocode 1 (Actions on structures) speaks about traffic loads on bridges. Where, section 5 is devoted to 'Actions on footways, cycle tracks and footbridges' [55].
- EN 1995-2: Appendix B of the second part of Eurocode 5 (Design of timber structures) is about vibrations caused by pedestrians on timber bridges [56].

None of them gives any suggestion for a loading model. There is only a suggestion on how to calculate the accelerations of a simply supported or truss timber bridge in Eurocode 5.

It is worth mentioning here, since it could be possible to extend it to any other type of footbridge. The accelerations in [m/s^2] when several persons are crossing the bridge are given by:

$$a = \begin{cases} 0.23 a_{v,1} N k_v & \text{for vertical accelerations} \\ 0.18 a_{h,1} N k_h & \text{for horizontal accelerations} \end{cases} \tag{5.5}$$

where N is the number of pedestrians. A value of 13 is suggested for a distinct group or 0.6 times the area of the footbridge's deck [m^2] for a continuous flow of pedestrians. k_v and k_h are coefficients that depend on the fundamental natural frequency of the bridge in the vertical f_v and horizontal direction f_h. These are given in figures 53 and 54. $a_{v,1}$ and $a_{h,1}$ are the accelerations in the vertical and horizontal direction for a single pedestrian. For walking, they are given by:

$$a_{v,1} = \begin{cases} \frac{200}{M\xi} & \text{for f}_v \le 2.5 \text{ Hz} \\ \frac{100}{M\xi} & \text{for 2.5 Hz} < \text{f}_v < 5.0\text{Hz} \end{cases} \quad \text{and } a_{h,1} = \frac{50}{M\xi} \quad \text{for } 0.5 \text{ Hz} \le f_h \le 2.5 \text{ Hz} \tag{5.6}$$

with M the total mass of the footbridge [kg] and ξ its damping ratio [-].

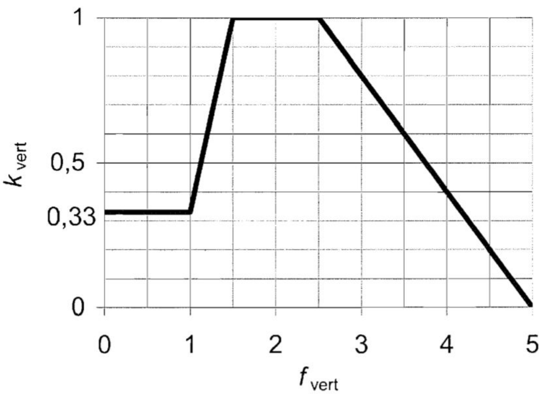

Figure 53: Value of the coefficient k_v depending on f_v [56]

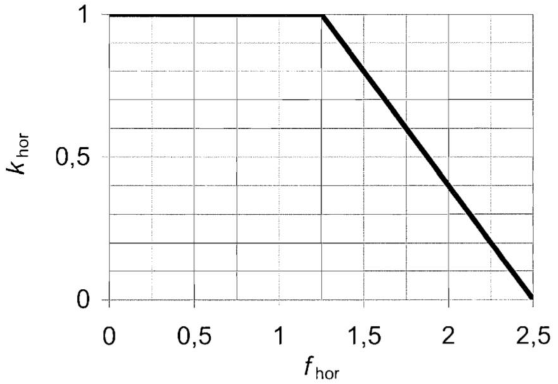

Figure 54: Value of the coefficient k_h depending on f_h [56]

5.2 Definition of the parameters

For the application of the joint input-state estimation algorithm to the Geierlay footbridge, various parameters are needed.

- The first vertical modes are defined by the following natural frequencies: $f_{v,1} = 0.42$Hz, $f_{v,2} = 0.56$Hz and $f_{v,3} = 0.63$Hz.
- This time the lateral motion will also be analysed. The first corresponding modes are defined by the following natural frequencies: $f_{lat,1} = 0.16$Hz, $f_{lat,2} = 0.24$Hz and $f_{lat,3} = 0.29$Hz.
- For the same reasons as stated above, a damping ratio of $\xi = 1.4\%$ is considered.
- The footbridge has a length of $l = 363.9$m.
- Since a pedestrian needs around 9 minutes to cross the bridge his walking velocity is deduced to be $v_s = 0.67$m/s.

- The generalised mass of the footbridge for the first modes is equal to $M_1^* = 27.57$T, $M_2^* = 37.12$T and $M_3^* = 33.37$T according to [42].
- The pedestrian's step frequency is considered to be of 1.8Hz, which is a mean value between slow and normal walking.
- The pedestrian's weight is assumed to be 700N as suggested by the Sétra guide [1].
- $n_{d,a} = 4$ have been recorded for each set of measurements. Only one data set is given as input in the algorithm each time, since the various sets have not been recorded at the same time and under the same conditions, they should not be mixed up. The corresponding coordinates are taken equal to the locations where the sensors have been placed on the footbridge. These were given in chapter 3.

This time the real measured accelerations on site are used in the data vector d. These are not simulated anymore as it was done for the test cases. An acquisition frequency of approximately 32Hz has been chosen which corresponds to a sampling step of $\Delta t = 0.0313$s.

5.3 Discussion of the results

During the experimental campaign, only accelerations were measured and no displacements nor velocities. From results shown in chapter 4, we already concluded that the algorithm will not be stable and nor be able to correctly capture the static component of the pedestrian's load.

Several proposals are suggested to solve this problem. These are based on the algorithm analysis done in chapter 4.

- Create a new acceleration signal with a smaller sampling step based on the measured ones, by doing an interpolation.
- Generate velocities based on the accelerations, by doing an integration.
- Calculate a static displacement.
- Use a high-pass filter on the measured accelerations. As seen on previous results, when observing the FFT of the identified modal load, the algorithm struggles to capture the low frequencies when no displacement is used.

Some of these propositions have been tested. Such as the interpolation of the measured accelerations. However, the identified modal loads seem to be unstable. This is confirmed by doing an interpolation of the simulated accelerations for the test cases, where the same effect is observed. The idea was to decrease the sampling step of the measurements already done without having to do them again. Additionally, depending on the measurement equipment it is not always possible to chose an arbitrary small sampling step. However, by doing an interpolation, information is created between the known data points, this pollutes the original measurements and leads to an erroneous modal load identification. A similar effect is expected for the second proposition. Indeed by integrating the accelerations to generate velocities, an initial error on the measurements is increased linearly and the obtained velocities may be wrong. By doing a double integration to obtain the displacement, the error increases even exponentially, this is why this idea is not suggested above. Various methods have been proposed in the literature to avoid these problems and [5] and [12] are just two examples.

The aim of this work is not to analyse or apply a method to obtain displacements or velocities from accelerations measurements done on site. It is to identify pedestrian loads in order to compare the obtained values to those given by existing loading models. Since the algorithm yields accurate results for the dynamic component of the load and since this is precisely the one that causes problems for certain footbridges. Thus in the following a high-pass filter is applied on the measured accelerations[2].

The identified modal load is shown in the following section and directly compared to the maximum values suggested by the various loading models. Only the vertical and lateral loads are analysed here. The former have the highest amplitude whereas the latter have been the cause of problems in the past.

5.4 Comparison of the identified loads with existing loading models

The identified modal loads in the vertical and transverse direction are shown in this section. These are directly compared to the maximum values obtained by applying existing loading models for a group of pedestrians, which are given in the first section of this chapter 5.

A distinction is made between the load identified based on the second data set done at the beginning of the footbridge and the one based on the third data set done at mid-span. The reason is the different local shape of the footbridge at these two measurement locations. At the entry of the footbridge, the walkway is inclined by approximately 27%, whereas at midspan the walkway can be considered flat. This has an impact on the amplitude of the pedestrian load, as will be shown and discussed in the following. However, notice that both measurement sets were not carried out at the same time, thus these were not recorded under the same conditions. As already said above the third set was done later that day, where fewer pedestrians were crossing the footbridge. For the second data set $N = 50$ pedestrians are considered to be on the footbridge at a given moment, which corresponds to approximately two groups of 25 people. For the third data set $N = 40$ pedestrians. These are only approximate values since the exact number of pedestrians at each moment on the footbridge has not been recorded.

5.4.1 Vertical direction

The results and comparison for the modal loads in the vertical direction are shown in figure 55 for the entry of the footbridge and in figure 56 at midspan.

For the vertical direction three loading models are compared:

- The first one is the loading model suggested by the Sétra guide [1]. In this case, a sparse or dense crowd can be considered. Thus, $N_{eq} = 10.8\sqrt{N\xi}$ with a damping ratio of approximately 1.4%. A value of $N_{eq,2nd\,set} = 9.05$ and $N_{eq,3rd\,set} = 8.08$ pedestrians is obtained for both data sets. This equivalent number of pedestrians multiplies the load due to a single pedestrian. The dynamical load factors of Bachmann et al. are used as suggested in the guide, which are $\alpha_1 = 0.4$ and $\alpha_2 = \alpha_3 = 0.1$.
- The loading modal suggested by Bachmann and Ammann [6] where the single pedestrian load using the DLF suggested by the same authors and also used in the Sétra

---

[2] The function *butter* is used for this in Matlab.

guide is multiplied by a factor $k = \sqrt{N}$. In this case, a value of $k_{2nd\ set} = 7.07$ and $k_{3rd\ set} = 6.32$ is obtained.

- A third loading model is suggested by Ebrahimpour et al. [14], where new DLF are defined. In this case for a frequency of approximately 2.0Hz and with N>10, the value of $\alpha_1 = 0.25$ should be used. Notice that if the definition of a single pedestrian load is used with only the 1st harmonic and this given DLF, the obtained load is very small, as they suggest that the DLF is constant when the number of 10 pedestrians is exceeded. Thus, even if it is not specified this value will be multiplied by N to obtain a more reasonable value and avoid ruling out this model immediately.

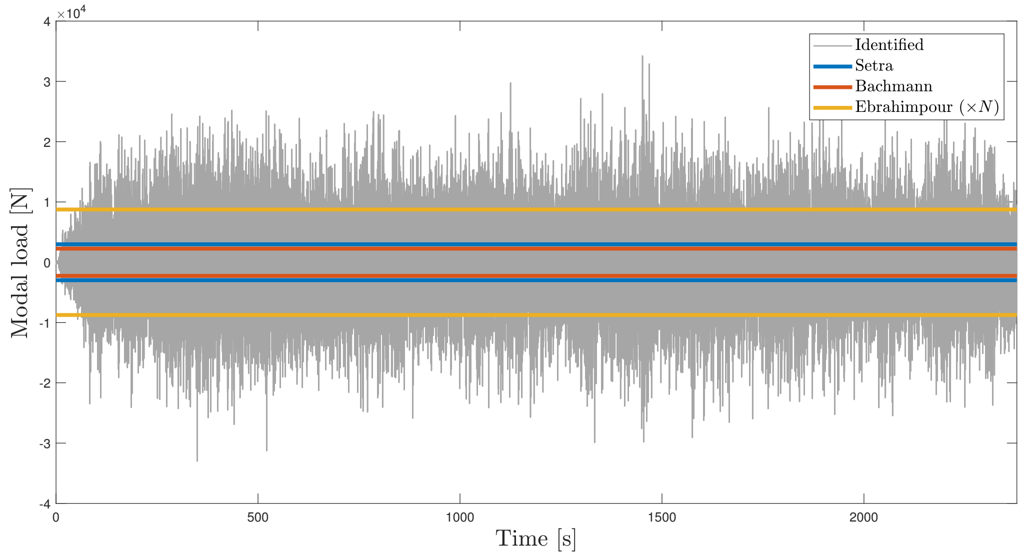

Figure 55: Comparison of the identified modal loads based on accelerations recorded at the entry of the footbridge with existing loading models for vertical load due to a group of pedestrians.

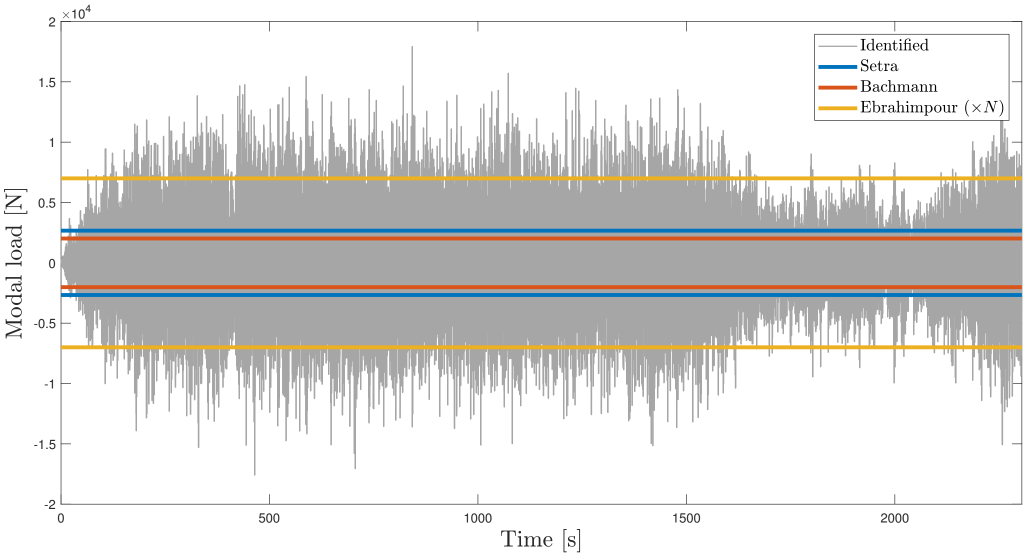

Figure 56: Comparison of the identified modal load based on accelerations recorded at mid span of the footbridge with existing loading models for vertical load due to a group of pedestrians.

It can be seen in figures 55 and 56 that the existing loading models tend to underestimate the modal load. In fact, these have been developed based on tests done on flat and rigid surfaces. The results show that they are no longer valid if applied to a flexible or inclined surface.

Pedestrians crossing a flexible footbridge tend to adapt to the bridge's motion, this has a direct impact on the force profile. For flexible surfaces, the heel strike peak becomes larger and the toe-off peak smaller as shown in figure 57. Thus, analysing only one step, the corresponding dynamical load factors tend to increase for a flexible footbridge as demonstrated in [4]. However, if the sum of several strides are analysed the inverse observations are done, for which slightly smaller DLF are found. Nevertheless, notice that the Geierlay footbridge can be considered as a more flexible structure as the one used in [4], which is only 7m long. The GRF may still be different, as well as the DLF. In [3], it is concluded that the dynamical load component increases for a flexible structure. The idea to keep from these references is that the flexibility of the surface does have an impact on the vertical dynamic loads due to walking. Besides, the flexibility of the footbridge can increase the probability of synchronisation which also has an impact on the load. Up to the author's knowledge, there is not much research comparing the pedestrian load on rigid to flexible footbridges like the Geierlay.

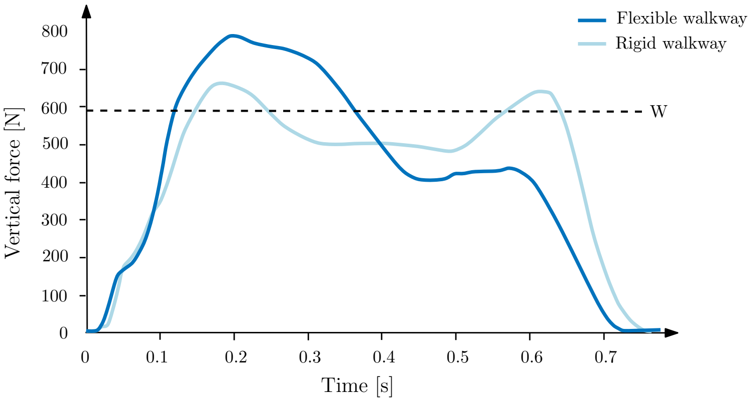

Figure 57: Vertical dynamical load on a flexible and a rigid walkway (adapted from [4])

Additionally, it is shown in [38], that the slope of the surface also has an impact on the vertical loads. These tend to increase, whether it is an upward or downward slope, as shown in figure 58. Approximately the same results are obtained in [11]). These observations have been done for slopes up to 10%, thus in the case of the Geierlay footbridge with a slope of approximately 27% at the entries, the effects are probably even more striking.

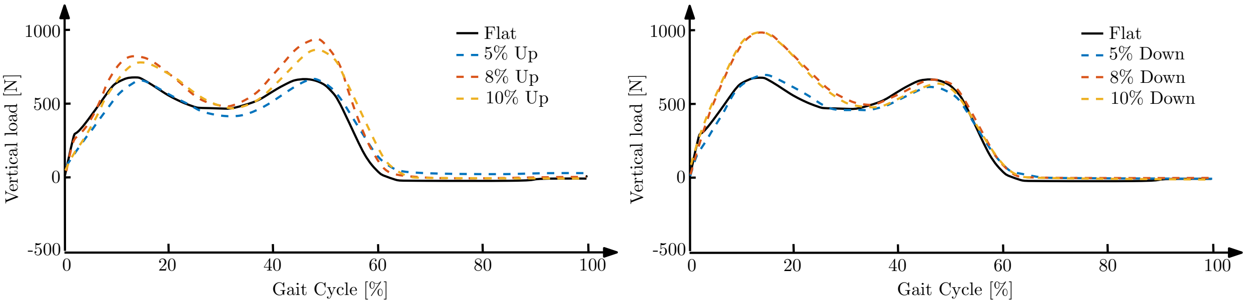

Figure 58: Influence of an inclined surface on the vertical load (adapted from [38])

An inclined surface also impacts the gait parameters of a pedestrian, such as the step length, its walking velocity and step frequency. Based on [38] and [39], the frequency tends to increase for a downwards slope and decreases for an upward slope. Concerning the step length and walking speed, results vary depending on the authors who did tests on this topic. A fairly complete summary is given in [39]. This has an influence on the loading models, as the step frequency f_s directly intervenes in the definition of a single pedestrian load.

By comparing both identified modal loads based on the set of measurements recorded at the beginning of the footbridge and at its midspan, it can be seen that the first ones have a higher amplitude. Two reasons can be put forward. First, the set of measurements at midspan have been recorded later in the day of the experimental campaign and fewer people were crossing the footbridge, as already mentioned above. A second reason is due to the different slope for both locations where the data was recorded. The impact of which has just been explained.

5.4.2 Transverse direction

The same analysis is done for the load in the transverse direction, which are again compared to the corresponding existing loading models, as shown in figure 59 for the entry of the footbridge and in figure 60 for the midspan.

For the transverse direction, one existing loading model from Fujino et al. [18] is used here for the comparison. However, various values for the dynamical load factors or the rate of synchronisation are tested.

- The first loading model is used with the DLF suggested by the Sétra guide [1], which is $\alpha_1 = 0.05$ from Charles and Hoorpah. The synchronisation rate is used equal to 20% as suggested by Fujino et al. Thus the single pedestrian load is multiplied by a value of $m_F, 2nd\ set = 10$ for the 2nd data set and $m_F, 2nd\ set = 8$ for the 3rd one.
- Another comparison is done by using the DLF from Bachmann et al. [6], which are $\alpha_1 = \alpha_2 = \alpha_3 = 0.1$ and the same rate of synchronisation is used. Therefore, the factor values do not change compared to the model before.
- A third comparison is done by using the DLF from Bachmann et al., but this time 60% of synchronisation is assumed. This value is more appropriate, as in chapter 3 it was observed that the acceleration's amplitude exceed the value of 0.1m/s^2. Thus according to the Sétra guide, the synchronisation can climb up to 60% or even higher. The factors become $m_{F,2nd\ set} = 30$ and $m_{F,2nd\ set} = 24$

Similar observations as for the vertical loads can be done. Figure 59 and 60 show that the original Fujino et al. loading models with only 20% of synchronisation tend to underestimate the identified modal loads. By using a synchronisation rate of 60% the obtained maximum value becomes more representative and fits the obtained results better. This is especially the case for the modal load identified based on the data set recorded at the midspan of the footbridge. Where the amplitude of the identified modal load is smaller than the one based on the second data set done at the beginning of the footbridge. The same two reasons as above can be used here ie. a difference in the number of pedestrians. Additionally, the fact that the slope can be considered flat at midspan, whereas at the beginning of the footbridge it is not. This has an impact also on the transverse pedestrian load as will be shown below.

A direct comparison of the force profile in the transverse direction for a rigid and a flexible footbridge could not be found. However, as discussed for the vertical load, the flexibility of the footbridge may influence also the transverse single pedestrian load which results in an adaptation of the DLF. Further research on this topic should be done to confirm this hypothesis.

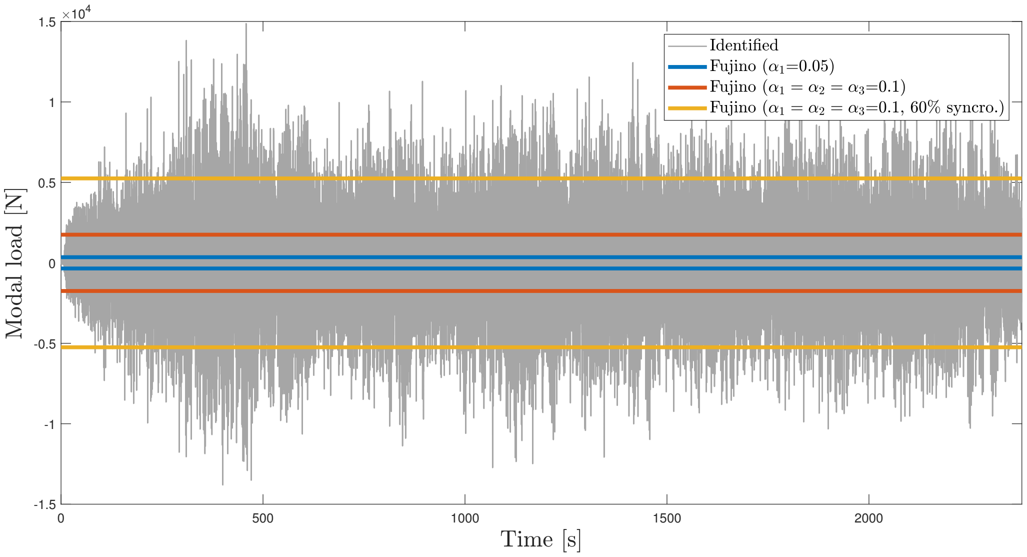

Figure 59: Comparison of the identified modal load based on accelerations recorded at the entry of the footbridge with existing loading models for transverse load due to a group of pedestrians.

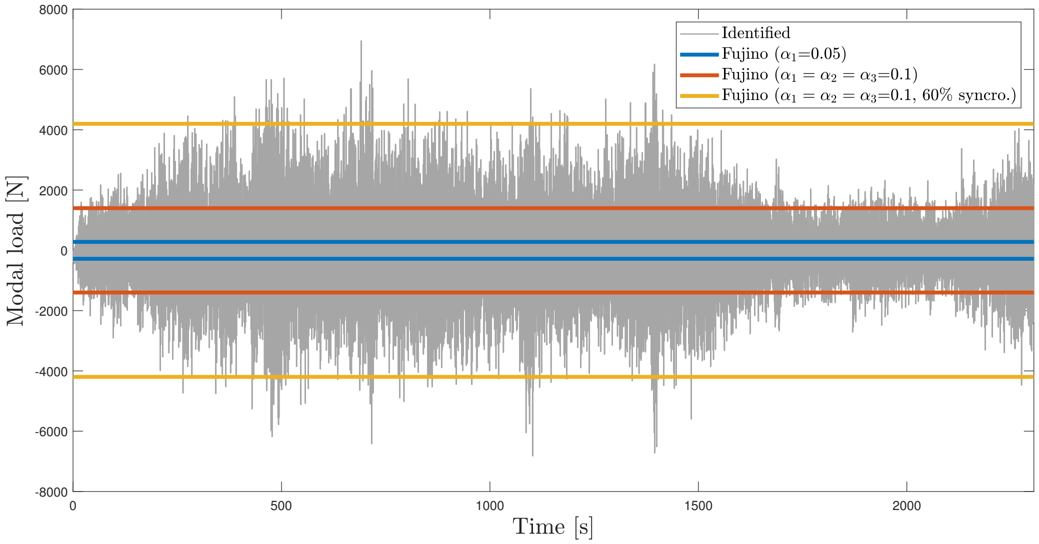

Figure 60: Comparison of the identified modal load based on accelerations recorded at mid span of the footbridge with existing loading models for transverse load due to a group of pedestrians.

The influence of the slope on the transverse load is shown in figure 61 and discussed in [11]. In the transverse direction, the impact is even more significant than in the vertical direction. Thus it has to be taken into account to avoid underestimating the modal load. This can again be done by increasing the dynamical load factors intervening in the definition of a single pedestrian load.

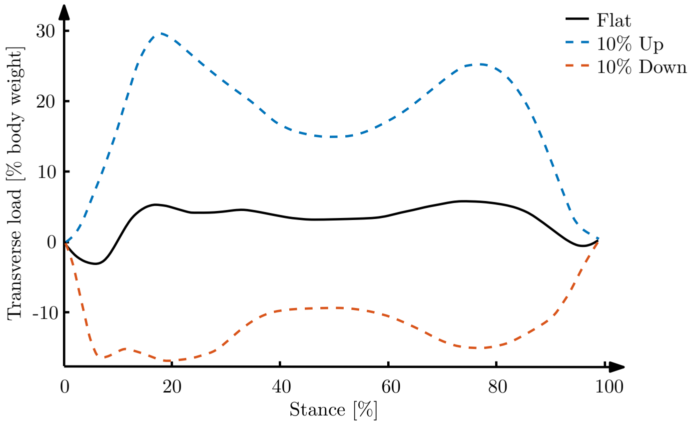

Figure 61: Influence of an inclined surface on the transverse load (adapted from [11])

5.5 Suggestion of improvements

The easiest way to model the load due to a pedestrian group is to rely on the loading model for a single pedestrian and to multiply it by a given factor. As observed in the previous section 5.4, the existing loading models tend to underestimate the load. Based on the results for the Geierlay footbridge, a new factor that fits the modal load better identified in this work can be suggested. This should be checked more rigorously before applying it to other footbridges since it is only based on measurements done on the Geierlay and under specific conditions.

To simplify the problem, only the first harmonic contribution of a single pedestrian is considered and the static component is not taken into account. Thus, the vertical and lateral load for a single pedestrian is given by

$$F_v(t) = \alpha_{1,v} \cdot W \sin\left(2\pi f_s t\right) \tag{5.7}$$

and

$$F_{lat}(t) = \alpha_{1,lat} \cdot W \sin\left(2\pi \frac{f_s}{2}\right) t \tag{5.8}$$

where W is the pedestrian's weight, α_1 is the Fourier coefficient of the first harmonic, also called DLF and f_s is the pedestrian's step frequency.

The first unknown is α_1, several authors suggested various values. These are summarized in section 4.1 of chapter 4 and depend on which step frequency is considered. In this case, the pedestrians cross the Geierlay footbridge with a slow or normal walk, which corresponds to a step frequency of 1.6-2.0 Hz. In this interval, the coefficient's values vary from 0.188 to 0.5 for the vertical load and from 0.039 to 0.1 for the lateral load. However, notice that for inclined and flexible surfaces the pedestrian loads tends to increase as shown above. Thus bigger values may be taken in that case. The second unknown is the factor k by which the single pedestrian load needs to be multiplied to obtain the identified load for a group of pedestrians.

Based on the upper envelope of the identified modal loads, a histogram indicates which range of values appears most often. The corresponding cumulative distribution function (CDF) is then used to determine the modal load that is not exceeded 95% of the time, as suggested in [22]. This is done for the vertical and transverse load, as well as the load identified at the entry and midspan of the footbridge. These are shown in figures 62, 63, 64 and 65.

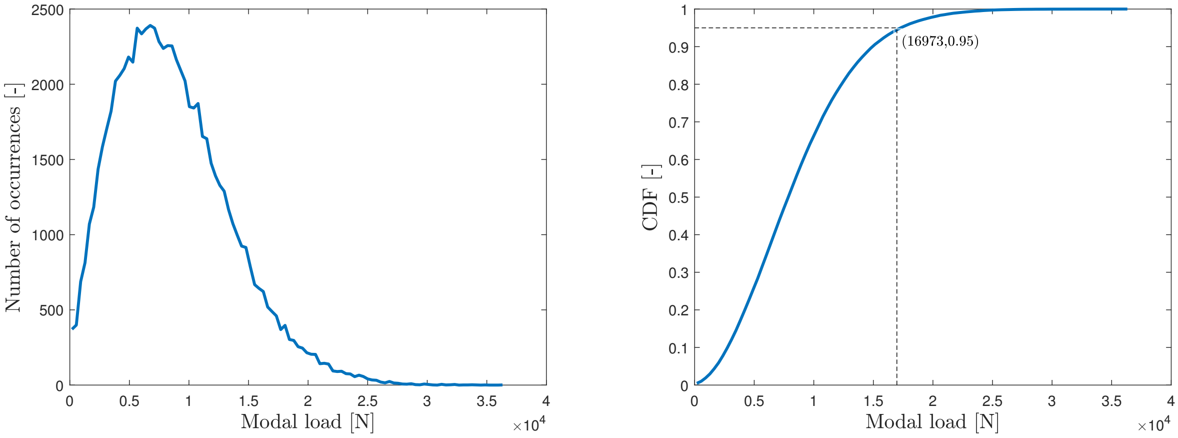

Figure 62: Histogram of the identified vertical modal load envelope based on the acceleration identified at the entry of the footbridge and the corresponding CDF.

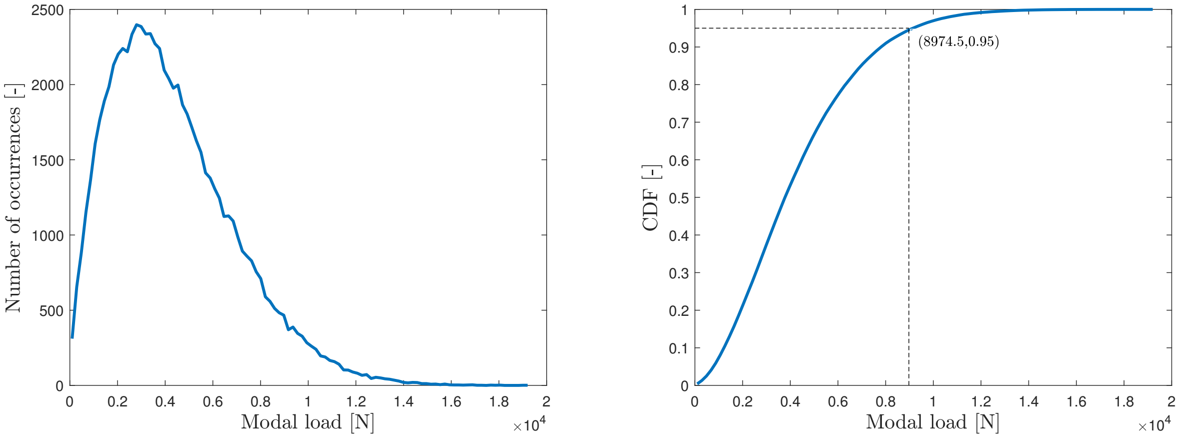

Figure 63: Histogram of the identified vertical modal load envelope based on the acceleration identified at the mid span of the footbridge and the corresponding CDF.

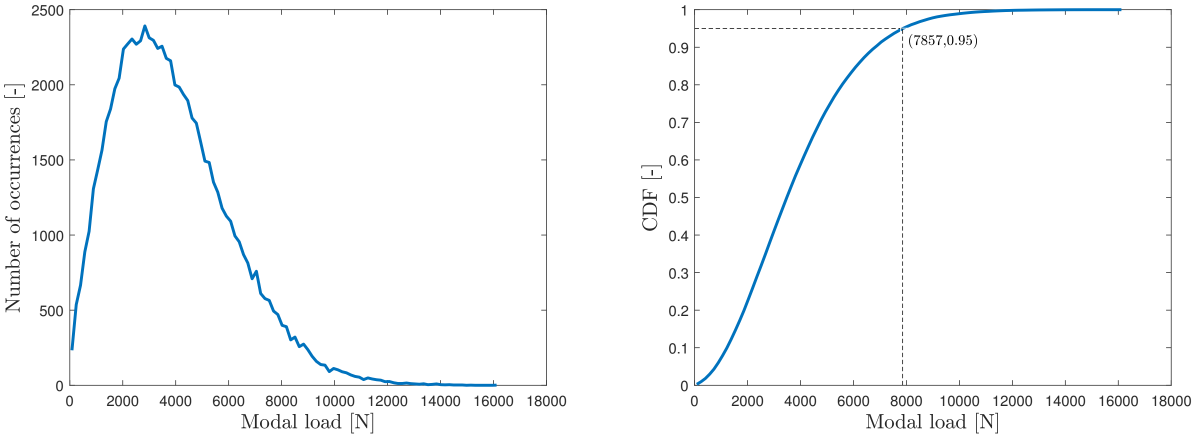

Figure 64: Histogram of the identified transverse modal load envelope based on the acceleration identified at the entry of the footbridge and the CDF.

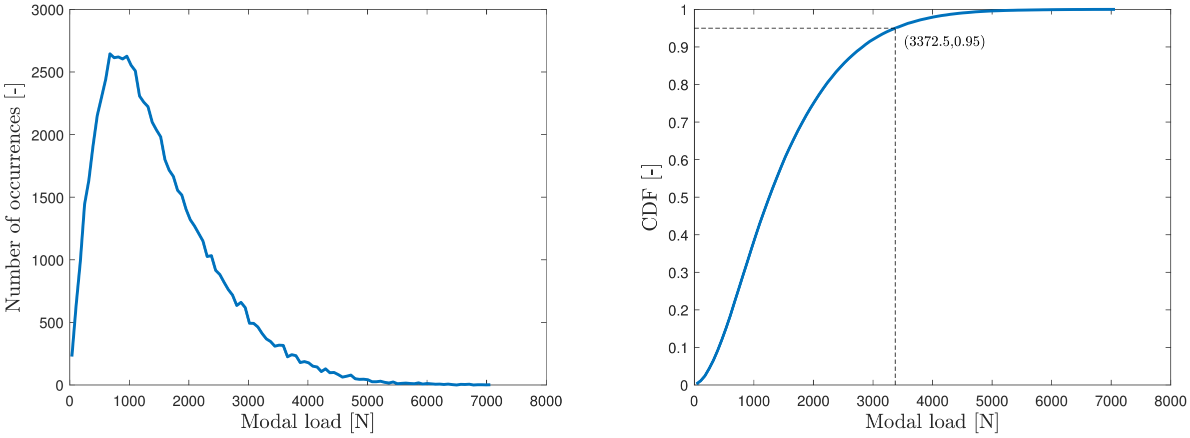

Figure 65: Histogram of the identified transverse modal load envelope based on the acceleration identified at the mid span of the footbridge and the CDF.

The identified dynamic component of the modal load can be considered symmetric. Thus only the upper envelope is used and compared to the maximum value of the upper envelope given by the single pedestrian loading model. Knowing that the modal load is defined by

$$p^*(t) = F(t)\Phi(vt) \tag{5.9}$$

Thus,

$$p^*_{v,group} = k_v \cdot \alpha_{1,v} \cdot W \sin{(2\pi f_s t)}\Phi(vt) \tag{5.10}$$

$$p^*_{lat,group} = k_{lat} \cdot \alpha_{1,lat} \cdot W \sin{\left(2\pi \frac{f_s}{2}\right)} t\Phi(vt) \tag{5.11}$$

The product $k \cdot \alpha_1$, can easily be calculated. The obtained values are given in table 16.

	Vertical		Transverse	
	Modal load [kN]	$k \cdot \alpha_1$ [-]	Modal load [kN]	$k \cdot \alpha_1$ [-]
Inclined walkway	16.973	24.25	7.857	11.23
Flat walkway	8.975	12.82	3.373	4.82

Table 16: Unknown product $k \cdot \alpha_1$ corresponding for the identified modal load from the upper envelope in vertical and transverse direction

As discussed above, the flexibility of the surface as well as its slope have a direct impact on the ground reaction forces and thus also on the dynamical load factors that appear in the definition of the load due to a single pedestrian. The values suggested by the various authors, which are summarized in chapter 4 should be adapted by increasing them. New DLF should be determined as a function of the surface type and its slope. So far only a distinction between walking and running is done.

The factor k also needs to be adapted. It has to be larger compared to those suggested at the beginning of this chapter. Due to the high accelerations and the flexibility of the footbridge, pedestrians are more likely to synchronise. This factor only depends on the number of pedestrians on the footbridge at a given moment and maybe on the damping ratio of the footbridge as suggested by the Sétra guide [1].

If a synchronisation of 60% is considered in the transverse direction and assuming 50 pedestrians when the measurements were taken on the inclined walkway and 40 when taken on the flat walkway, then a value of $\alpha_1 = 0.374$ and $\alpha_1 = 0.201$ are obtained. These have to be compared to $\alpha_1 = \alpha_2 = \alpha_3 = 0.1$ suggested by Bachmann et al.[6]. However, notice that only the first harmonic is considered to obtain the values of α_1, if more harmonics are considered the calculated values would be slightly smaller. Besides a mean pedestrian weight of 700N is considered, the real value may be slightly different. If the same synchronisation ratio is taken in the vertical direction. A value of $\alpha_1 = 0.808$ and $\alpha_1 = 0.534$ are obtained, compared to $\alpha_1 = 0.4$ and $\alpha_2 = \alpha_3 = 0.1$ suggested by the same author for a step frequency of 2Hz.

Additionally, it is shown in [38] and [39], that the slope of the walkway has also an impact on the gait parameters of the pedestrians, such as its step frequency, step length and walking velocity. This also has a direct impact on the pedestrian load, which is already taken into account in the existing single pedestrian loading models, where the step frequency f_s appears. Unfortunately, the step frequency of the pedestrians crossing the Geierlay footbridge was not measured. Thus it is impossible to quantify the influence in this case.

To be able to suggest a new loading model more precise measurements should have been taken, by noting the exact weight of the pedestrians, their step frequency and the exact number of pedestrians on the footbridge at any time. From this analysis, we can conclude that the dynamical load factors, as well as the enhancement factor, should be increased compared to those suggested in the literature, but due to a lack of measurement precision, no exact nor general values may be given in this work.

Perspectives

As shown throughout this work the joint input-state estimation algorithm works very well to identify the dynamic component of the load induced by pedestrians on the Geierlay footbridge. The results are compared with existing loading models and improvements are suggested based on the obtained results. This is already a step towards a better understanding of loads due to groups or crowds of pedestrians on a flexible footbridge. Nevertheless, there is still work to do. Therefore, a list of possible ideas for further investigation based on the work presented in this thesis is provided.

- During the experimental campaign, we had no influence on the pedestrians crossing the bridge. It would be interesting to do some measurements with multiple groups with a fixed and known number of pedestrians and to measure their step frequency and self-weight for more accurate results. This enables also a better analysis and interpretation of them.
- Another idea is to carry out measurements with different sizes of groups, to analyse if there is a linear relation between the number of pedestrians and the identified modal load or not. This could be pushed up to a fully loaded footbridge. So far the existing loading models for groups of pedestrians consist in multiplying the load due to a single pedestrian by a constant factor depending on the number of pedestrians present at a given moment on the footbridge. However, the synchronisation rate depends on this number and it may not vary linearly. By doing these tests, the relation could easily be determined and improve understanding of synchronisation effects for example.
- For a better understanding of the pedestrian load on inclined surfaces, measurements should be taken in the ascendant, descendant and flat walkway part of the footbridge. As already mentioned, the pedestrian load will be different in these different parts, or at least for the inclined and flat surfaces. This should enable the immediate suggestion of new dynamical load factors. To avoid comparison problems as those encountered in this work, the measurements should be done under the same conditions. This can be done for a single pedestrian and groups of pedestrians to observe and identify the differences. These observations are necessary to suggest a loading model that can be applied on other footbridges with a different shape.
- The ground reaction forces on a very flexible footbridge like the Geierlay and on a rigid footbridge should be measured and compared. This would allow a better understanding of the influence of a flexible surface on the pedestrian loads in the three directions, i.e vertical, transverse and longitudinal. Only little research has focused on this topic and it would be interesting to dig a little deeper.

- To have more measurements that can be fed to the algorithm more accelerometers should be used. Additionally, at least one displacement could be measured to allow the identification of the static component of the pedestrian load.
- Here the joint input-state estimation algorithm is applied on only one single real flexible footbridge. For a better understanding and to be able to suggest improvements to existing loading models, or even suggest a new one that could be applied for every flexible footbridge, the same study should be done on other flexible footbridges. The results could then be compared in hopes of finding a trend.

Conclusion

The goal of this work was to identify pedestrian loads on a very flexible footbridge by using a dynamic inverse technique. It gives access to them with relative ease compared to other methods. The loads are then analysed for a better understanding, with the intention of designing future footbridges more accurately.

First, different existing methods used for the identification of pedestrian loads were presented. The advantages of an indirect approach based only on accurately measurable accelerations are highlighted. Particular attention was given to the joint input-state estimation algorithm which behaves well in the presence of noise and which was used in this work. It is a simple and effective method compared to other indirect or direct approaches, which are less accurate and may even be more costly and/or only feasible in the laboratory. The algorithm is an extension of the well-known Kalman filter and is based on the discrete-time state-space model in a modal basis. It was rederived in this work to obtain the definition of the four system matrices. A small modification compared to other references is introduced here, in that mode shapes normalized to a unit maximum absolute value were used. The algorithm is first validated and analysed by means of two simple one-dimensional test cases. This allowed determining its limitations. The main one is that without the knowledge of a displacement, it is impossible to capture the static component of the pedestrian load. Only the dynamical one, which is of greater interest for footbridges anyway, as it is the cause of high vibration problems, may be obtained from the algorithm. Then the algorithm was applied to the Geierlay footbridge on which vibration measurements were taken at the start of the academic year. These were analysed by standard methods as the peak picking and the covariance-driven stochastic subspace identification methods to identify the modal properties of the footbridge, such as its natural frequencies and damping ratios. The identified dynamic load was then compared to existing loading models for groups or crowds of pedestrians. This comparison showed that these tend to underestimate the load, which can be explained by various reasons related to the slope and the flexibility of the footbridge. The existing loading models are based on tests on rigid and flat structures and in this work it was shown that these are no longer valid for a footbridge like the Geierlay. The dynamical load factors and the enhancement factor should be increased compared to those suggested by various authors.

The procedure presented in this work i.e. carrying out measurements on a real footbridge, identifying its modal properties and applying the joint input-state estimation algorithm can and should be applied on other existing footbridges. The results may then be compared to those presented in this thesis to suggest a loading model applicable to any footbridge, regardless of its shape and its degree of flexibility. Thus the suggested dynamical load factors should depend at least on these two parameters.

Bibliography

[1] Service d'études techniques des routes et autoroutes (Sétra). *Technical guide - Footbridges: Assessment of vibrational behaviour of footbridges under pedestrian loading.* Sétra, Association Française de Génie Civil (AFGC), 2006.

[2] A. Archbold. "Vertical Crowd Load Models for Vibration Serviceability Assessment of Footbridges". *Proceedings of the Twelfth International Conference on Civil, Structural and Environmental Engineering Computation* 217 (2009).

[3] P. Archbold and B. Mullarney. "Interaction Between Pedestrian Loading and Vibration Response of a Laboratory-Scale FRP Composite Footbridge". *New York City Bridge Conference* (2017).

[4] P. Archbold, B. Mullarney, and M. Carrig. "Variations in vertical loading from walking due to surface vibration". *5th International Conference - Footbridges: Past, Present and Future* (2014).

[5] M. Arraigada and M. Partl. "Calculation of displacements of measured accelerations, analysis of two accelerometers and application in road engineering". *6th Swiss Transport Research Conerence* (2006).

[6] H. Bachmann and W. Ammann. *Vibrations in Structures: Induced by Man and Machine.* Structural Engineering Documents. IABSE-AIPC-IVBH, 1987.

[7] H. Bachmann et al. *Vibration problems in structures: Practical guidelines.* CEB, 1995.

[8] A. Belli et al. "A treadmill ergometer for three-dimensional ground reaction forces measurements during walking". *Journal of Biomechanics* vol. 34.1 (2001), pp. 105–112.

[9] Gulf Coast Data Concepts. "User manual: X2-5 USB Accelerometer Data Logger" (2020).

[10] A. Forner Cordero, H.J.F.M. Koopman, and F.C.T. van der Helm. "Use of pressure insoles to calculate the complete ground reaction forces". *Journal of Biomechanics* vol. 37.9 (2004), pp. 1427–1432.

[11] M. Damavandi, P. C. Dixon, and D. J. Pearsall. "Ground reaction force adaptions during cross-slope walking and running". *Human Movement Science* vol. 31 (2012), pp. 182–189.

[12] R. Delpoux, H. Sira-Ramirez, and T. Floquet. "Acceleration Feedback via an algebraic state estimation method". *52nd IEEE Conference on Decision and Control* (2013).

[13] V. Denoël. *Analyse des structures II.* URL: `http://hdl.handle.net/2268/130616`. (accessed: 24.04.2021).

[14] A. Ebrahimpour et al. “Measuring and modeling dynamic loads imposed by moving crowds”. *Journal of Structural Engineering* vol. 122.12 (1996), pp. 1468–1474.

[15] Association of Engineers et al. “Geierlay”. *Revue Technique Luxembourgeoise* (2017), pp. 48–51.

[16] A. Firus et al. “A novel method for indirect measurement of ground reaction forces on vibrating structures”. *Eurodyn* (2020), pp. 1883–1895.

[17] D. T.-P. Fong et al. “Use of pressure insoles to calculate the complete ground reaction forces”. *Journal of Biomechanics* vol. 41.11 (2008), pp. 2597–2601.

[18] Y. Fujino et al. “Synchronization of human walking observed during lateral vibration of a congested pedestrian bridge”. *Earthquake Engineering and Structural Dynamics* vol. 22.9 (1993), pp. 741–758.

[19] S. Gillijns and B. De Moor. “Unbiased minimum-variance input and state estimation for linear discrete-time systems with direct feedthrough”. *Automatica* vol. 43 (2007), pp. 934–937.

[20] Bureau Greisch. *Greisch Design with FinelG.* URL: `https://www.greisch.com/`. (accessed: 04.06.2021).

[21] P. Hawryszkow, R. Pimentel, and F. Silva. “Vibration effects of loads due to groups crossing a lively footbridge”. *X International Conference on Structural Dynamics, EURODYN* vol. 199 (2017), pp. 2808–2813.

[22] C. Heinemeyer et al. *Design of Lightweight Footbridges for Human Induced Vibrations - Background document in support to the implementation, harmonization and further development of the Eurocodes.* JRC-Scientific and Technical Report. JRC, ECCS, 2009.

[23] E.T. Ingolfsson, C.T. Georgakis, and J. Jönsson. *Pedestrian-induced lateral vibrations of footbridges: Experimental studies and probabilistic modelling.* Kgs. Lyngby, Danemark: Technical University of Danemark (DTU), 2011.

[24] N. Janberg. *Structurae: Base de donées et galerie internationale d’ouvrages d’art et du génie civil.* URL: `https://structurae.net/`. (accessed: 10.05.2021).

[25] T. Kailath, A. H. Sayed, and B. Hassibi. *Linear estimation.* Prentice Hall Information and System Sciences Series. Upper Saddle River, New Jersey, 2000.

[26] S. C. Kerr. “Human induced loading on staircases”. *PhD Thesis.* University College London, UK (1998).

[27] M. Kirchhoff. URL: `https://geierlay.de/`. (accessed: 18.04.2021).

[28] Kistler. “Product catalogue: Force plates and accessories. Biomechanics measuring systems for performance diagnostics, gait analysis, rehabilitation, and ergonomics” (2017).

[29] P. Latteur. *Calculer une structure: De la théorie à l’exemple.* Academia-Bruyant, 2011.

[30] J. Lettner. “Étude du confort vibratoire du «Geierlay», le plus long pont de singe d’Allemagne”. *Master Thesis.* University of Liège, Belgium (2017).

[31] F.L. Lewis. “Multivariable zeros of state-space systems” (2008).

[32] E. Lourens et al. “Joint input-response estimation for structural systems based on reduced-order models and vibration data from a limited number of sensors”. *Mechanical Systems and Signals Processing* vol. 29 (2012), pp. 310–327.

[33] K. Maes et al. “Design of sensors networks for instantaneous inversion of modally reduced order models in structural dynamics”. *Mechanical Systems and Signal Processing* (2014).

[34] K. Maes et al. “Joint input-state estimation in structural dynamics”. *Mechanical Systems and Signals Processing* vol. 70-71 (2016), pp. 445–466.

[35] K. Maes et al. “Verification of joint input-state estimation for force identification by means of in situ measurements on a footbridge”. *Mechanical Systems and Signal Processing* vol. 75 (2016), pp. 245–260.

[36] Y. Matsumoto, H. Shiojiri, and T. Nishioka. “Dynamic design of footbridges”. *IABSE Proceedings* vol. 2 (1978).

[37] D. McGuckian. URL: `https://www.statsprofessor.com/learn-statistics-online.php`. (accessed: 27.03.2021).

[38] A. Stuart McIntosh et al. “Gait dynamics on an inclined walkway”. *Journal of Biomechanics* vol.39 (2006), pp. 2491–2502.

[39] B. Mullarney and P. Archbold. “A study on the effect slope walking has on vertical pedestrian loading in terms of footbridge design”. *Applied Mechanics and Materials* vol. 679 (2014), pp. 217–227.

[40] A. Muro-de-la-Herran, B. Garcia-Zapirain, and A. Mendez-Zorrilla. “Gait Analysis Methods: An Overview of Wearable and Non-Wearable Systems, Highlighting Clinical Applications”. *Sensors* vol. 14.2 (2014), pp. 3362–3394.

[41] T.M. Murray, D.E. Allen, and E.E. Ungar. “Floor Vibrations Due to Human Activity”. *Steel Design Series Guide* 11 (1997).

[42] C. Dago Ngodji. “Identification des forces piétonnes sur une passerelle: Pont de singe à Trèves (Allemagne)”. *Master Thesis.* University of Liège, Belgium (2020).

[43] K. Van Nimmen et al. “Characterisation of walking loads by 3D inertial motion tracking”. *Journal of Sound and Vibration* vol. 333 (2014), pp. 5212–5226.

[44] K. Van Nimmen et al. “Inverse identification of pedestrian-induced loads”. *ISMA* (2016).

[45] K. Van Nimmen et al. “Vibration seriveability of footbridges: Evaluation of the current codes of practice”. *Engineering Structures* vol. 59 (2014), pp. 448–461.

[46] S. Niu, C. Wang, and S. Gao. “A novel crowd random loads model for pedestrians walking on footbridges”. *Archive of Applied Mechanics* vol. 86.7 (2016), pp. 1369–1381.

[47] B. Peeters. “System identification and damage detection in civil engineering”. *Doctoral Thesis.* University of Leuven, Belgium (2000).

[48] H. Pfaffen. “Statik Hängeseilbrücke über das Mörsdorfer Bachtal, Teil A: Lastannahmen, Konstruction, Materialien, Lastermittlung auf Tragsystem une Bemessung Stahlteile zur Brückenkonstruction”. *Ingenieurbüro Hans Pfaffen* (2015), p. 63.

[49] S. Qin, J. Kang, and Q. Wang. “Operational Modal Analysis Based on Subspace Algorithm with an Improved Stabilization Diagram Method”. *Shock and Vibration* (2016).

[50] V. Racic, A. Pavic, and J.M.W. Brownjohn. “Experimental identification and analytical modelling og human walking forces: Literature review”. *Journal of Sound and Vibration* vol. 326 (2009), pp. 1–49.

[51] V. Racic, A. Pavic, and J.M.W. Brownjohn. “Modern facilities for experimental measurement of dynamic loads induced by humans: A literature review”. *Shock and Vibration* vol. 20 (2013), pp. 53–67.

[52] E. de Sá Caetano. *Cable Vibrations in Cable-Stayed Bridges*. Structural Engineering Documents. International Association for Bridge and Structural Engineering (IABSE), 2007. ISBN: 978-3-85748-115-4.

[53] E. Shahabpoor et al. “Effect of group walking traffic on dynamic properties of pedestrian structures”. *Journal of Sound and Vibration* vol. 387 (2017), pp. 207–225.

[54] European Committee for Standardization. *EN 1990-A2 Eurocode 0: Basis of structural design - A2: Application to Bridges*. CEN, 2005.

[55] European Committee for Standardization. *EN 1991-2 Eurocode 1: Actions on structures - Part 2: Traffic loads on bridges*. CEN, 2003.

[56] European Committee for Standardization. *EN 1995-2 Eurocode 5: Design of timber structures - Part 2: Bridges*. CEN, 2004.

[57] *Suspension Bridge Geierlay*. URL: `https://www.waymarking.com/waymarks/wmQRJC_LARGEST_Hiking_Path_Footbridge_Geierlay_Mrsbach_Rhineland_Palatinate_Germany`. (accessed: 31.05.2021).

[58] W. Tang and D. Su. “Locomotion analysis and its applications in neurological disorders detection: state-of-art review”. *Network Modeling Analysis in Health Informatics and Bioinformatics* vol. 2 (2013), pp. 1–12.

[59] Rheinland-Pfalz Tourismus. URL: `https://www.rlp-tourismus.com/fileadmin/_processed_/f/4/csm_Hunsrueck_Geierlay_Moersdorf_Ketz_14832_b62af9a957.jpg`. (accessed: 18.04.2021).

[60] E. Turco. “A strategy to identify exciting forces acting on structures”. *International Journal for numerical methods in engineering* 64 (2005), pp. 1483–1508.

[61] R. W.Clough and J. Penzien. *Dynamics of structures*. McGraw-Hill Inc., 1975.

[62] M. Zivanovic and A. Pavic. “Dynamic response of footbridges due to vertical load models of pedestrians”. *Proceeding of the 8th International Conference on Structural Dynamics, EURODYN* (2011), pp. 1027–1034.

[63] S. Zivanovic, A. Pavic, and P. Reynolds. “Vibration serviceability of footbridges under human-induced excitation: a literature review”. *Journal of Sound and Vibration* vol. 279 (2005), pp. 1–74.

Appendix

Appendix A - Formulation of the algorithm

The formulation of the algorithm developed in more detail in this section is based on [19] and [34]. The algorithm derives from the discrete-time state-space model given by[3]:

$$\begin{cases} \mathbf{x}_{[k+1]} = \mathbf{A}\mathbf{x}_{[k]} + \mathbf{B}\mathbf{p}_{[k]} + \mathbf{w}_{[k]} & \text{(A. 12)} \\ \mathbf{d}_{[k]} = \mathbf{G}\mathbf{x}_{[k]} + \mathbf{J}\mathbf{p}_{[k]} + \mathbf{v}_{[k]} & \text{(A. 13)} \end{cases}$$

And also from the following recursive three-step filter:

$$\hat{\mathbf{x}}_{[k|k-1]} = \mathbf{A}\hat{\mathbf{x}}_{[k-1|k-1]} + \mathbf{B}\hat{\mathbf{p}}_{[k-1|k-1]} \qquad \text{Time update} \qquad \text{(A. 14)}$$

$$\hat{\mathbf{p}}_{[k|k]} = \mathbf{M}_{[\mathbf{k}]}\left(\mathbf{d}_{[k]} - \mathbf{G}\hat{\mathbf{x}}_{[k|k-1]}\right) \qquad \text{Input estimation step} \qquad \text{(A. 15)}$$

$$\hat{\mathbf{x}}_{[k|k]} = \hat{\mathbf{x}}_{[k|k-1]} + \mathbf{L}_{[\mathbf{k}]}\left(\mathbf{d}_{[k]} - \mathbf{G}\hat{\mathbf{x}}_{[k|k-1]}\right) \qquad \text{Measurement update} \qquad \text{(A. 16)}$$

Where, $\hat{\mathbf{x}}$ and $\hat{\mathbf{p}}$ are estimations of the state vector $\mathbf{x}$ and the input vector $\mathbf{p}$ respectively. $\mathbf{A}$, $\mathbf{B}$, $\mathbf{G}$ and $\mathbf{J}$ are the system matrices assumed to be known and which are defined in Chapter 2. The matrices $\mathbf{M}$ and $\mathbf{L}$ have yet to be determined such that $\hat{\mathbf{x}}$ and $\hat{\mathbf{p}}$ are minimum variance and unbiased estimators (MVUE). An estimator is unbiased when its average value is equal to the target value and the smaller is its variance, the closer its values are to the target value [37].

The initial state estimate $\hat{\mathbf{x}}_{[0|-1]}$ is assumed being unbiased and independent of the noise processes $\mathbf{w}_{[k]}$ and $\mathbf{v}_{[k]}$ for all k.

Time update

The time update step estimates the unknown state vector $\mathbf{x}_{[k]}$ based on the measured output up to time step k-1. The interest now is to know the error made by using an estimation of the state and the input. An easy way to define it is to calculate the difference between the exact vector and the estimate.

Thus, by using equations (A. 12) and (A. 14), the error on the state estimate becomes:

---

[3] Details of the development to obtain this model are given in Chapter 2: Joint input-state estimation algorithm

$$
\begin{aligned}
\tilde{\mathbf{x}}_{[k|k-1]} &\equiv \mathbf{x}_{[k]} - \hat{\mathbf{x}}_{[k|k-1]} \\
&= \left(\mathbf{A}\mathbf{x}_{[k-1]} + \mathbf{B}\mathbf{p}_{[k-1]} + \mathbf{w}_{[k-1]}\right) - \left(\mathbf{A}\hat{\mathbf{x}}_{[k-1|k-1]} + \mathbf{B}\hat{\mathbf{p}}_{[k-1|k-1]}\right) \\
&= \mathbf{A}\left(\mathbf{x}_{[k-1]} - \hat{\mathbf{x}}_{[k-1|k-1]}\right) - \mathbf{B}\left(\mathbf{p}_{[k-1]} - \hat{\mathbf{p}}_{[k-1|k-1]}\right) + \mathbf{w}_{[k-1]} \\
&= \mathbf{A}\tilde{\mathbf{x}}_{[k-1|k-1]} + \mathbf{B}\tilde{\mathbf{p}}_{[k-1|k-1]} + \mathbf{w}_{[k-1]} \qquad \text{(A. 17)}
\end{aligned}
$$

Or by using equations (A. 13) and (A. 16), it becomes :

$$
\begin{aligned}
\tilde{\mathbf{x}}_{[k|k]} &\equiv \mathbf{x}_{[k]} - \hat{\mathbf{x}}_{[k|k]} \\
&= \mathbf{x}_{[k]} - \left(\hat{\mathbf{x}}_{[k|k-1]} + \mathbf{L}_{[k]}\left(\mathbf{d}_{[k]} - \mathbf{G}\hat{\mathbf{x}}_{[k|k-1]}\right)\right) \\
&= \mathbf{x}_{[k]} - \left(\hat{\mathbf{x}}_{[k|k-1]} + \mathbf{L}_{[k]}\left(\mathbf{G}\mathbf{x}_{[k]} + \mathbf{J}\mathbf{p}_{[k]} + \mathbf{v}_{[k]} - \mathbf{G}\hat{\mathbf{x}}_{[k|k-1]}\right)\right) \\
&= \left(\mathbf{I} - \mathbf{L}_{[k]}\mathbf{G}\right)\left(\mathbf{x}_{[k]} - \hat{\mathbf{x}}_{[k|k-1]}\right) - \mathbf{L}_{[k]}\mathbf{J}\mathbf{p}_{[k]} - \mathbf{L}_{[\mathbf{k}]}\mathbf{v}_{[k]} \\
&= \left(\mathbf{I} - \mathbf{L}_{[k]}\mathbf{G}\right)\tilde{\mathbf{x}}_{[k|k-1]} - \mathbf{L}_{[k]}\mathbf{J}\mathbf{p}_{[k]} - \mathbf{L}_{[k]}\mathbf{v}_{[k]} \qquad \text{(A. 18)}
\end{aligned}
$$

The error on the input estimate is defined in the same way and by using equations (A. 13) and (A. 15):

$$
\begin{aligned}
\tilde{\mathbf{p}}_{[k|k]} &\equiv \mathbf{p}_{[k]} - \hat{\mathbf{p}}_{[k|k]} \\
&= \mathbf{p}_{[k]} - \mathbf{M}_{[k]}\left(\mathbf{d}_{[k]} - \mathbf{G}\hat{\mathbf{x}}_{[k|k-1]}\right) \\
&= \mathbf{p}_{[k]} - \mathbf{M}_{[k]}\left(\mathbf{G}\mathbf{x}_{[k]} + \mathbf{J}\mathbf{p}_{[k]} + \mathbf{v}_{[k]} - \mathbf{G}\hat{\mathbf{x}}_{[k|k-1]}\right) \\
&= \left(\mathbf{I} - \mathbf{M}_{[k]}\mathbf{J}\right)\mathbf{p}_{[k]} - \mathbf{M}_{[k]}\mathbf{G}\left(\mathbf{x}_{[k]} - \hat{\mathbf{x}}_{[k|k-1]}\right) - \mathbf{M}_{[k]}\mathbf{v}_{[k]} \\
&= \left(\mathbf{I} - \mathbf{M}_{[k]}\mathbf{J}\right)\mathbf{p}_{[k]} - \mathbf{M}_{[k]}\mathbf{G}\tilde{\mathbf{x}}_{[k|k-1]} - \mathbf{M}_{[k]}\mathbf{v}_{[k]} \qquad \text{(A. 19)}
\end{aligned}
$$

Using equation (A. 17) as well as the definition of the noise covariance matrices[4] $\mathbf{Q}$ and $\mathbf{R}$, the covariance matrix of the error on the state estimate $\tilde{\mathbf{x}}_{[k|k-1]}$ is given by:

$$
\begin{aligned}
\mathbf{P}_{x[k|k-1]} &\equiv \mathbb{E}\left[\tilde{\mathbf{x}}_{[k|k-1]}\tilde{\mathbf{x}}^T_{[k|k-1]}\right] \\
&= \mathbb{E}\left[\left(\mathbf{A}\tilde{\mathbf{x}}_{[k-1|k-1]} + \mathbf{B}\tilde{\mathbf{p}}_{[k-1|k-1]} + \mathbf{w}_{[k-1]}\right)\left(\mathbf{A}\tilde{\mathbf{x}}_{[k-1|k-1]} + \mathbf{B}\tilde{\mathbf{p}}_{[k-1|k-1]} + \mathbf{w}_{[k-1]}\right)^T\right] \\
&= \mathbb{E}\left[\left(\mathbf{A}\tilde{\mathbf{x}}_{[k-1|k-1]} + \mathbf{B}\tilde{\mathbf{p}}_{[k-1|k-1]} + \mathbf{w}_{[k-1]}\right)\left(\tilde{\mathbf{x}}^T_{[k-1|k-1]}\mathbf{A}^T + \tilde{\mathbf{p}}^T_{[k-1|k-1]}\mathbf{B}^T + \mathbf{w}^T_{[k-1]}\right)\right] \\
&= \mathbb{E}\Big[\mathbf{A}\tilde{\mathbf{x}}_{[k-1|k-1]}\tilde{\mathbf{x}}^T_{[k-1|k-1]}\mathbf{A}^T + \mathbf{A}\tilde{\mathbf{x}}_{[k-1|k-1]}\tilde{\mathbf{p}}^T_{[k-1|k-1]}\mathbf{B}^T + \mathbf{A}\tilde{\mathbf{x}}_{[k-1|k-1]}\mathbf{w}^T_{[k-1]} \\
&\quad + \mathbf{B}\tilde{\mathbf{p}}_{[k-1|k-1]}\tilde{\mathbf{x}}^T_{[k-1|k-1]}\mathbf{A}^T + \mathbf{B}\tilde{\mathbf{p}}_{[k-1|k-1]}\tilde{\mathbf{p}}^T_{[k-1|k-1]}\mathbf{B}^T + \mathbf{B}\tilde{\mathbf{p}}_{[k-1|k-1]}\mathbf{w}^T_{[k-1]} \\
&\quad + \mathbf{w}_{[k-1]}\tilde{\mathbf{x}}^T_{[k-1|k-1]}\mathbf{A}^T + \mathbf{w}_{[k-1]}\tilde{\mathbf{p}}^T_{[k-1|k-1]}\mathbf{B}^T + \mathbf{w}_{[k-1]}\mathbf{w}^T_{[k-1]}\Big] \\
&= \begin{bmatrix}\mathbf{A} & \mathbf{B}\end{bmatrix}\begin{bmatrix}\mathbb{E}\left[\tilde{\mathbf{x}}_{[k-1|k-1]}\tilde{\mathbf{x}}^T_{[k-1|k-1]}\right] & \mathbb{E}\left[\tilde{\mathbf{x}}_{[k-1|k-1]}\tilde{\mathbf{p}}^T_{[k-1|k-1]}\right] \\ \mathbb{E}\left[\tilde{\mathbf{p}}_{[k-1|k-1]}\tilde{\mathbf{x}}^T_{[k-1|k-1]}\right] & \mathbb{E}\left[\tilde{\mathbf{p}}_{[k-1|k-1]}\tilde{\mathbf{p}}^T_{[k-1|k-1]}\right]\end{bmatrix}\begin{bmatrix}\mathbf{A}^T \\ \mathbf{B}^T\end{bmatrix} + \mathbb{E}\left[\mathbf{w}_{[k-1]}\mathbf{w}^T_{[k-1]}\right] \\
&\quad + \underbrace{\mathbb{E}\left[\mathbf{A}\tilde{\mathbf{x}}_{[k-1|k-1]}\mathbf{w}^T_{[k-1]} + \mathbf{B}\tilde{\mathbf{p}}_{[k-1|k-1]}\mathbf{w}^T_{[k-1]} + \mathbf{w}_{[k-1]}\tilde{\mathbf{x}}^T_{[k-1|k-1]}\mathbf{A}^T + \mathbf{w}_{[k-1]}\tilde{\mathbf{p}}^T_{[k-1|k-1]}\mathbf{B}^T\right]}_{i}
\end{aligned}
$$

---

[4] See Chapter 2: Joint input-state estimation algorithm

In order to simplify expression (i), one have to look at the properties of the matrices $\mathbf{M}$ and $\mathbf{L}$ mentioned above. Knowing that the error on the state estimate $\tilde{\mathbf{x}}_{[k|k-1]}$ does not depend on the input $\mathbf{p}_{[k|k]}$, the state estimate $\hat{\mathbf{x}}_{[k|k-1]}$ is unbiased if and only if $\hat{\mathbf{x}}_{[k|k]}$ and $\hat{\mathbf{p}}_{[k|k]}$ are unbiased for all k.

Let us first introduce the definition of the innovation:

$$\begin{aligned}\tilde{\mathbf{d}}_{[k]} &\equiv \mathbf{d}_{[k]} - \mathbf{G}\hat{\mathbf{x}}_{[k|k-1]} \\ &= \mathbf{G}\mathbf{x}_{[k]} + \mathbf{J}\mathbf{p}_{[k]} + \mathbf{v}_{[k]} - \mathbf{G}\hat{\mathbf{x}}_{[k|k-1]} \\ &= \mathbf{J}\mathbf{p}_{[k]} + \mathbf{G}\left(\mathbf{x}_{[k]} - \hat{\mathbf{x}}_{[k|k-1]}\right) + \mathbf{v}_{[k]} \\ &= \mathbf{J}\mathbf{p}_{[k]} + \mathbf{G}\tilde{\mathbf{x}}_{[k|k-1]} + \mathbf{v}_{[k]} \\ &= \mathbf{J}\mathbf{p}_{[k]} + \boldsymbol{e}_{[k]} \qquad \text{(A. 20)}\end{aligned}$$

According to the definition of $\boldsymbol{e}_{[k]}$, if $\hat{\mathbf{x}}_{[k|k-1]}$ is unbiased, then $\mathbb{E}\left[\boldsymbol{e}_{[k]}\right] = 0$. Such that, if the expectation operator is applied to (A. 20), it yields

$$\mathbb{E}\left[\tilde{\mathbf{d}}_{[k]}\right] = \mathbf{J}\mathbb{E}\left[\mathbf{p}_{[k]}\right] = \mathbf{J}\mathbf{p}_{[k]} \qquad \text{(A. 21)}$$

which means that an unbiased estimate of $\mathbf{p}_{[k]}$ can be obtained from the innovation $\tilde{\mathbf{d}}_{[k]}$.

By introducing (A. 20) in (A. 15):

$$\begin{aligned}\hat{\mathbf{p}}_{[k|k]} &= \mathbf{M}_{[\mathbf{k}]}\left(\mathbf{d}_{[k]} - \mathbf{G}\hat{\mathbf{x}}_{[k|k-1]}\right) \\ &= \mathbf{M}_{[\mathbf{k}]}\left(\mathbf{d}_{[k]} - \left(\mathbf{d}_{[k]} - \tilde{\mathbf{d}}_{[k]}\right)\right) \\ &= \mathbf{M}_{[\mathbf{k}]}\left(\mathbf{J}\mathbf{p}_{[k]} + \boldsymbol{e}_{[k]}\right) \\ &= \mathbf{M}_{[\mathbf{k}]}\mathbf{J}\mathbf{p}_{[k]} + \mathbf{M}_{[\mathbf{k}]}\boldsymbol{e}_{[k]}\end{aligned}$$

Thus, if $\hat{\mathbf{x}}_{[k|k-1]}$ is assumed unbiased, then $\hat{\mathbf{p}}_{[k|k]}$ is unbiased as well, for all $\mathbf{p}_{[k]}$ if and only if

$$\mathbf{M}_{[k]}\mathbf{J} = \mathbf{I} \qquad \text{(A. 22)}$$

By introducing (A. 20) in (A. 16), yields:

$$\begin{aligned}\hat{\mathbf{x}}_{[k|k]} &= \hat{\mathbf{x}}_{[k|k-1]} + \mathbf{L}_{[\mathbf{k}]}\left(\mathbf{d}_{[k]} - \mathbf{G}\hat{\mathbf{x}}_{[k|k-1]}\right) \\ &= \hat{\mathbf{x}}_{[k|k-1]} + \mathbf{L}_{[\mathbf{k}]}\left(\mathbf{J}\mathbf{p}_{[k]} + \boldsymbol{e}_{[k]}\right) \\ &= \hat{\mathbf{x}}_{[k|k-1]} + \mathbf{L}_{[\mathbf{k}]}\mathbf{J}\mathbf{p}_{[k]} + \mathbf{L}_{[\mathbf{k}]}\boldsymbol{e}_{[k]}\end{aligned}$$

In the same manner, $\hat{\mathbf{x}}_{[k|k]}$ is unbiased for all $\mathbf{p}_{[k]}$ if and only if

$$\mathbf{L}_{[k]}\mathbf{J} = \mathbf{0} \qquad \text{(A. 23)}$$

By using the properties (A. 22) and (A. 23), the equations (A. 18) and (A. 19), as well as the definition of a matrix $\mathbf{N}$, given by:

$$\mathbf{N}_{[k]} = \mathbf{A}\mathbf{L}_{[k]} + \mathbf{B}\mathbf{M}_{[k]} \qquad \text{(A. 24)}$$

the term (i) becomes:

$$\begin{aligned}
&\mathbb{E}\left[\mathbf{A}\tilde{\mathbf{x}}_{[k-1|k-1]}\mathbf{w}^T_{[k-1]} + \mathbf{B}\tilde{\mathbf{p}}_{[k-1|k-1]}\mathbf{w}^T_{[k-1]} + \mathbf{w}_{[k-1]}\tilde{\mathbf{x}}^T_{[k-1|k-1]}\mathbf{A}^T + \mathbf{w}_{[k-1]}\tilde{\mathbf{p}}^T_{[k-1|k-1]}\mathbf{B}^T\right] \\
=&\mathbb{E}\Big[\mathbf{A}\left(\mathbf{I} - \mathbf{L}_{[k-1]}\mathbf{G}\right)\tilde{\mathbf{x}}_{[k-1|k-2]}\mathbf{w}^T_{[k-1]} - \cancel{\mathbf{A}\mathbf{L}_{[k-1]}\mathbf{J}\mathbf{p}_{[k-1]}\mathbf{w}^T_{[k-1]}} - \mathbf{A}\mathbf{L}_{[k-1]}\mathbf{v}_{[k-1]}\mathbf{w}^T_{[k-1]} \\
&+ \cancel{\mathbf{B}\left(\mathbf{I} - \mathbf{M}_{[k-1]}\mathbf{J}\right)\mathbf{p}_{[k-1]}\mathbf{w}^T_{[k-1]}} - \mathbf{B}\mathbf{M}_{[k]}\mathbf{G}\tilde{\mathbf{x}}_{[k-1|k-2]}\mathbf{w}^T_{[k-1]} - \mathbf{B}\mathbf{M}_{[k-1]}\mathbf{v}_{[k-1]}\mathbf{w}^T_{[k-1]} \\
&+ \mathbf{w}_{[k-1]}\left(\left(\mathbf{I} - \mathbf{L}_{[k-1]}\mathbf{G}\right)\tilde{\mathbf{x}}_{[k-1|k-2]}\right)^T\mathbf{A}^T - \cancel{\mathbf{w}_{[k-1]}\left(\mathbf{L}_{[k-1]}\mathbf{J}\mathbf{p}_{[k-1]}\right)^T\mathbf{A}^T} \\
&- \mathbf{w}_{[k-1]}\mathbf{v}^T_{[k-1]}\mathbf{L}^T_{[k-1]}\mathbf{A}^T + \cancel{\mathbf{w}_{[k-1]}\left(\left(\mathbf{I} - \mathbf{M}_{[k-1]}\mathbf{J}\right)\mathbf{p}_{[k-1]}\right)^T\mathbf{B}^T} \\
&- \mathbf{w}_{[k-1]}\left(\mathbf{M}_{[k-1]}\mathbf{G}\tilde{\mathbf{x}}_{[k-1|k-2]}\right)^T\mathbf{B}^T - \mathbf{w}_{[k-1]}\mathbf{v}^T_{[k-1]}\mathbf{M}^T_{[k-1]}\mathbf{B}^T\Big] \\
=&\mathbb{E}\Bigg[\underbrace{\mathbf{A}\left(\mathbf{I} - \mathbf{L}_{[k-1]}\mathbf{G}\right)\tilde{\mathbf{x}}_{[k-1|k-2]}\mathbf{w}^T_{[k-1]}}_{\mathbf{0}} - \underbrace{\mathbf{B}\mathbf{M}_{[k]}\mathbf{G}\tilde{\mathbf{x}}_{[k-1|k-2]}\mathbf{w}^T_{[k-1]}}_{\mathbf{0}} \\
&+ \underbrace{\mathbf{w}_{[k-1]}\left(\left(\mathbf{I} - \mathbf{L}_{[k-1]}\mathbf{G}\right)\tilde{\mathbf{x}}_{[k-1|k-2]}\right)^T\mathbf{A}^T}_{\mathbf{0}} + \underbrace{\mathbf{w}_{[k-1]}\left(\mathbf{M}_{[k-1]}\mathbf{G}\tilde{\mathbf{x}}_{[k-1|k-2]}\right)^T\mathbf{B}^T}_{\mathbf{0}}\Bigg] \\
&- \mathbf{A}\mathbf{L}_{[k-1]}\underbrace{\mathbb{E}\left[\mathbf{v}_{[k-1]}\mathbf{w}^T_{[k-1]}\right]}_{\mathbf{S}^T} - \mathbf{B}\mathbf{M}_{[k-1]}\underbrace{\mathbb{E}\left[\mathbf{v}_{[k-1]}\mathbf{w}^T_{[k-1]}\right]}_{\mathbf{S}^T} \\
&- \underbrace{\mathbb{E}\left[\mathbf{w}_{[k-1]}\mathbf{v}^T_{[k-1]}\right]}_{\mathbf{S}}\mathbf{M}^T_{[k-1]}\mathbf{B}^T - \underbrace{\mathbb{E}\left[\mathbf{w}_{[k-1]}\mathbf{v}^T_{[k-1]}\right]}_{\mathbf{S}}\mathbf{M}^T_{[k-1]}\mathbf{B}^T \\
=& - \mathbf{N}_{[k-1]}\mathbf{S}^T - \mathbf{S}\mathbf{N}^T_{[k-1]}
\end{aligned}$$

The terms that cancel each other out is because $\mathbf{w}_{[k]}$ is zero mean and both $\mathbf{w}_{[k]}$ and $\tilde{\mathbf{x}}_{[k|k]}$ are of the first order.

As a result, the covariance matrix of the error on the state estimate $\tilde{\mathbf{x}}_{[k|k-1]}$ transforms into:

$$\mathbf{P}_{x[k|k-1]} = \begin{bmatrix}\mathbf{A} & \mathbf{B}\end{bmatrix}\begin{bmatrix}\mathbf{P}_{x[k-1|k-1]} & \mathbf{P}_{xp[k-1|k-1]} \\ \mathbf{P}_{px[k-1|k-1]} & \mathbf{P}_{p[k-1|k-1]}\end{bmatrix}\begin{bmatrix}\mathbf{A}^T \\ \mathbf{B}^T\end{bmatrix} + \mathbf{Q} - \mathbf{N}_{[k-1]}\mathbf{S}^T - \mathbf{S}\mathbf{N}^T_{[k-1]} \qquad \text{(A. 25)}$$

Input estimation

This step is used to estimate the unknown input vector $\mathbf{p}_{[k]}$ given the measured output up to time step k. We just showed, the conditions for the estimators $\hat{\mathbf{x}}_{[k|k-1]}$, $\hat{\mathbf{x}}_{[k|k]}$ and $\hat{\mathbf{p}}_{[k|k]}$ to be unbiased. However, it still has to be demonstrate, that they are minimum variance.

As mentioned in [25], for a linear model of the form of (A. 20), where $\mathbf{p}_{[k|k]}$ is the unknown, an weighted least-squares estimator is given by:

$$\hat{\mathbf{p}}_{[k|k]} = \left(\mathbf{J}^T\mathbf{W}\mathbf{J}\right)^{-1}\mathbf{J}^T\mathbf{W}\tilde{\mathbf{d}}_{[k]} \qquad \text{(A. 26)}$$

where, $\mathbf{W}$ is a weighting matrix, and $\mathbb{E}[\hat{\mathbf{p}}_{[k|k]}] = \mathbf{p}_{[k|k]}$, based on (A. 21). According to the Gauss-Markov theorem, in order to minimize the corresponding force error covariance matrix $\mathbf{P}_{p[k|k]}$, the weighting matrix is chosen equal to $\tilde{\mathbf{R}}^{-1}_{[k]}$. Which is the covariance matrix of $\boldsymbol{e}_{[k]}$, such as:

$$\begin{aligned}
\tilde{\mathbf{R}}_{[k]} &= \mathbb{E}\left[\boldsymbol{e}_{[k]}\boldsymbol{e}_{[k]}^T\right] \\
&= \mathbb{E}\left[\left(\mathbf{G}\tilde{\mathbf{x}}_{[k|k-1]} + \mathbf{v}_{[k]}\right)\left(\mathbf{G}\tilde{\mathbf{x}}_{[k|k-1]} + \mathbf{v}_{[k]}\right)^T\right] \\
&= \mathbb{E}\left[\left(\mathbf{G}\tilde{\mathbf{x}}_{[k|k-1]} + \mathbf{v}_{[k]}\right)\left(\tilde{\mathbf{x}}_{[k|k-1]}^T\mathbf{G}^T + \mathbf{v}_{[k]}^T\right)\right] \\
&= \mathbb{E}\left[\mathbf{G}\tilde{\mathbf{x}}_{[k|k-1]}\tilde{\mathbf{x}}_{[k|k-1]}^T\mathbf{G}^T + \mathbf{G}\tilde{\mathbf{x}}_{[k|k-1]}\mathbf{v}_{[k]}^T + \mathbf{v}_{[k]}\tilde{\mathbf{x}}_{[k|k-1]}^T\mathbf{G}^T + \mathbf{v}_{[k]}\mathbf{v}_{[k]}^T\right] \\
&= \mathbf{G}\mathbb{E}\left[\tilde{\mathbf{x}}_{[k|k-1]}\tilde{\mathbf{x}}_{[k|k-1]}^T\right]\mathbf{G}^T + \mathbf{G}\,\underbrace{\mathbb{E}\left[\tilde{\mathbf{x}}_{[k|k-1]}\mathbf{v}_{[k]}^T\right]}_{\mathbf{0}} + \underbrace{\mathbb{E}\left[\mathbf{v}_{[k]}\tilde{\mathbf{x}}_{[k|k-1]}^T\right]}_{\mathbf{0}}\mathbf{G}^T + \mathbb{E}\left[\mathbf{v}_{[k]}\mathbf{v}_{[k]}^T\right] \\
&= \mathbf{G}\mathbf{P}_{x[k+1|k]}\mathbf{G}^T + \mathbf{R}
\end{aligned} \tag{A. 27}$$

The force error covariance matrix $\mathbf{P}_{p[k|k]}$, becomes:

$$\begin{aligned}
\mathbf{P}_{p[k|k]} &\equiv \mathbb{E}\left[\tilde{\mathbf{p}}_{[k|k]}\tilde{\mathbf{p}}_{[k|k]}^T\right] \\
&= \left(\mathbf{J}^T\tilde{\mathbf{R}}_{[k]}^{-1}\mathbf{J}\right)^{-1}\mathbf{J}^T\tilde{\mathbf{R}}_{[k]}^{-1}\tilde{\mathbf{R}}_{[k]}\tilde{\mathbf{R}}_{[k]}^{-1}\mathbf{J}\left(\mathbf{J}^T\tilde{\mathbf{R}}_{[k]}^{-1}\mathbf{J}\right)^{-1} \\
&= \left(\mathbf{J}^T\tilde{\mathbf{R}}_{[k]}^{-1}\mathbf{J}\right)^{-1}
\end{aligned} \tag{A. 28}$$

Thus, $\hat{\mathbf{p}}_{[k|k]}$ is an MVUE, also called an Gauss-Markov estimator. The definition of the matrix $\mathbf{M}_{[k]}$ can be deduced from above, as it is the least-squares (LS) solution of (A. 20), respecting condition (A. 22). The optimal gain matrix, is then given by:

$$\mathbf{M}_{[k]} = \left(\mathbf{J}^T\tilde{\mathbf{R}}_{[k]}^{-1}\mathbf{J}\right)^{-1}\mathbf{J}^T\tilde{\mathbf{R}}_{[k]}^{-1} \tag{A. 29}$$

Measurement update

Estimate of the unknown state vector $\mathbf{x}_{[k]}$ given the measured output up to time step k.

The definition of the gain matrix $\mathbf{L}_{[k]}$ has still to be determined, in order to respect the property (A. 23) ($\mathbf{L}_{[k]}\mathbf{J} = \mathbf{0}$) and such that the estimators are MVU. This matrix $\mathbf{L}_{[k]}$ can be obtained by minimizing the trace of the covariance matrix of the error on the state estimate $\hat{\mathbf{x}}_{[k|k]}$. Which is given by using (A. 18) and (A. 27):

$$\begin{aligned}
\mathbf{P}_{x[k|k]} &\equiv \mathbb{E}\left[\tilde{\mathbf{x}}_{[k|k]}\tilde{\mathbf{x}}_{[k|k]}^T\right] \\
&= \mathbb{E}\left[\left(\left(\mathbf{I} - \mathbf{L}_{[k]}\mathbf{G}\right)\tilde{\mathbf{x}}_{[k|k-1]} - \mathbf{L}_{[k]}\mathbf{v}_{[k]}\right)\left(\left(\mathbf{I} - \mathbf{L}_{[k]}\mathbf{G}\right)\tilde{\mathbf{x}}_{[k|k-1]} - \mathbf{L}_{[k]}\mathbf{v}_{[k]}\right)^T\right] \\
&= \mathbb{E}\left[\left(\left(\mathbf{I} - \mathbf{L}_{[k]}\mathbf{G}\right)\tilde{\mathbf{x}}_{[k|k-1]} - \mathbf{L}_{[k]}\mathbf{v}_{[k]}\right)\left(\tilde{\mathbf{x}}_{[k|k-1]}^T\left(\mathbf{I} - \mathbf{G}^T\mathbf{L}_{[k]}^T\right) - \mathbf{v}_{[k]}^T\mathbf{L}_{[k]}^T\right)\right] \\
&= \mathbb{E}\left[\left(\left(\mathbf{I} - \mathbf{L}_{[k]}\mathbf{G}\right)\tilde{\mathbf{x}}_{[k|k-1]}\right)\left(\tilde{\mathbf{x}}_{[k|k-1]}^T\left(\mathbf{I} - \mathbf{G}^T\mathbf{L}_{[k]}^T\right)\right) - \left(\left(\mathbf{I} - \mathbf{L}_{[k]}\mathbf{G}\right)\tilde{\mathbf{x}}_{[k|k-1]}\right)\mathbf{v}_{[k]}^T\mathbf{L}_{[k]}^T\right. \\
&\qquad \left. - \mathbf{L}_{[k]}\mathbf{v}_{[k]}\left(\tilde{\mathbf{x}}_{[k|k-1]}^T\left(\mathbf{I} - \mathbf{G}^T\mathbf{L}_{[k]}^T\right)\right) + \mathbf{L}_{[k]}\mathbf{v}_{[k]}\mathbf{v}_{[k]}^T\mathbf{L}_{[k]}^T\right] \\
&= \left(\mathbf{I} - \mathbf{L}_{[k]}\mathbf{G}\right)\mathbb{E}\left[\tilde{\mathbf{x}}_{[k|k-1]}\tilde{\mathbf{x}}_{[k|k-1]}^T\right]\left(\mathbf{I} - \mathbf{L}_{[k]}\mathbf{G}\right)^T + \mathbf{L}_{[k]}\mathbb{E}\left[\mathbf{v}_{[k]}\mathbf{v}_{[k]}^T\right]\mathbf{L}_{[k]}^T \\
&\qquad + \mathbb{E}\left[\underbrace{-\left(\left(\mathbf{I} - \mathbf{L}_{[k]}\mathbf{G}\right)\tilde{\mathbf{x}}_{[k|k-1]}\right)\mathbf{v}_{[k]}^T\mathbf{L}_{[k]}^T}_{\mathbf{0}} - \underbrace{\mathbf{L}_{[k]}\mathbf{v}_{[k]}\left(\tilde{\mathbf{x}}_{[k|k-1]}^T\left(\mathbf{I} - \mathbf{G}^T\mathbf{L}_{[k]}^T\right)\right)}_{\mathbf{0}}\right] \\
&= \left(\mathbf{I} - \mathbf{L}_{[k]}\mathbf{G}\right)\mathbb{E}\left[\tilde{\mathbf{x}}_{[k|k-1]}\tilde{\mathbf{x}}_{[k|k-1]}^T\right]\left(\mathbf{I} - \mathbf{L}_{[k]}\mathbf{G}\right)^T + \mathbf{L}_{[k]}\mathbb{E}\left[\mathbf{v}_{[k]}\mathbf{v}_{[k]}^T\right]\mathbf{L}_{[k]}^T
\end{aligned}$$

$$
\begin{aligned}
&= \left(\mathbf{I} - \mathbf{L}_{[k]}\mathbf{G}\right) \mathbf{P}_{x[k|k-1]} \left(\mathbf{I} - \mathbf{L}_{[k]}\mathbf{G}\right)^T + \mathbf{L}_{[k]}\mathbf{R}\mathbf{L}_{[k]}^T \\
&= \left(\mathbf{I} - \mathbf{L}_{[k]}\mathbf{G}\right) \mathbf{P}_{x[k|k-1]} \left(\mathbf{I} - \mathbf{L}_{[k]}\mathbf{G}\right)^T + \mathbf{L}_{[k]} \left(\tilde{\mathbf{R}}_{[k]} - \mathbf{G}\mathbf{P}_{x[k+1|k]}\mathbf{G}^T\right) \mathbf{L}_{[k]}^T \\
&= \left(\mathbf{P}_{x[k|k-1]} - \mathbf{L}_{[k]}\mathbf{G}\mathbf{P}_{x[k|k-1]}\right) \left(\mathbf{I} - \mathbf{G}^T\mathbf{L}_{[k]}^T\right) + \mathbf{L}_{[k]}\tilde{\mathbf{R}}_{[k]}\mathbf{L}_{[k]}^T - \mathbf{L}_{[k]}\mathbf{G}\mathbf{P}_{x[k+1|k]}\mathbf{G}^T\mathbf{L}_{[k]}^T \\
&= \mathbf{P}_{x[k|k-1]} - \mathbf{P}_{x[k|k-1]}\mathbf{G}^T\mathbf{L}_{[k]}^T - \mathbf{L}_{[k]}\mathbf{G}\mathbf{P}_{x[k|k-1]} + \cancel{\mathbf{L}_{[k]}\mathbf{G}\mathbf{P}_{x[k|k-1]}\mathbf{G}^T\mathbf{L}_{[k]}^T} \\
&\quad + \mathbf{L}_{[k]}\tilde{\mathbf{R}}_{[k]}\mathbf{L}_{[k]}^T - \cancel{\mathbf{L}_{[k]}\mathbf{G}\mathbf{P}_{x[k+1|k]}\mathbf{G}^T\mathbf{L}_{[k]}^T} \\
&= \mathbf{L}_{[k]}\tilde{\mathbf{R}}_{[k]}\mathbf{L}_{[k]}^T - \mathbf{L}_{[k]}\mathbf{G}\mathbf{P}_{x[k|k-1]} - \mathbf{P}_{x[k|k-1]}\mathbf{G}^T\mathbf{L}_{[k]}^T + \mathbf{P}_{x[k|k-1]}
\end{aligned}
$$

Lagrange multipliers can be used to introduce the constraint (A. 23) in the optimization problem, given by:

$$
\mathbf{L}_{[k]} = \text{arg min} \left(\text{trace}\left\{\mathbf{L}_{[k]}\tilde{\mathbf{R}}_{[k]}\mathbf{L}_{[k]}^T - 2\mathbf{L}_{[k]}\mathbf{G}\mathbf{P}_{x[k|k-1]} + \mathbf{P}_{x[k|k-1]}\right\} - 2\text{trace}\left\{\mathbf{L}_{[k]}\mathbf{J}\boldsymbol{\Lambda}_{[k]}^T\right\}\right)
$$

A linear, two equation system is obtained by saying that the derivative of the Lagrangian with respect to $\mathbf{L}_{[k]}$ and $\boldsymbol{\Lambda}_{[k]}$ have to be equal to zero:

$$
\tilde{\mathbf{R}}_{[k]}\mathbf{L}_{[k]}^T - \mathbf{G}\mathbf{P}_{x[k|k-1]} - \mathbf{J}\boldsymbol{\Lambda}_{[k]}^T = \mathbf{0}
$$

$$
\mathbf{L}_{[k]}\mathbf{J} = \mathbf{0}
$$

The solution of this system gives the optimal gain matrix, equal to:

$$
\mathbf{L}_{[k]} = \mathbf{P}_{x[k|k-1]}\mathbf{G}^T\tilde{\mathbf{R}}_{[k]}^{-1}\left(\mathbf{I} - \mathbf{J}\mathbf{M}_{[k]}\right)
$$

Or,

$$
\mathbf{L}_{[k]} = \mathbf{K}_{[k]}\left(\mathbf{I} - \mathbf{J}\mathbf{M}_{[k]}\right) \tag{A. 30}
$$

With,

$$
\mathbf{K}_{[k]} = \mathbf{P}_{x[k|k-1]}\mathbf{G}^T\tilde{\mathbf{R}}_{[k]}^{-1} \tag{A. 31}
$$

By introducing (A. 30) in the definition of $\mathbf{N}_{[k]}$ (A. 24), it becomes:

$$
\begin{aligned}
\mathbf{N}_{[k]} &= \mathbf{A}\mathbf{L}_{[k]} + \mathbf{B}\mathbf{M}_{[k]} \\
&= \mathbf{A}\mathbf{K}_{[k]}\left(\mathbf{I} - \mathbf{J}\mathbf{M}_{[k]}\right) + \mathbf{B}\mathbf{M}_{[k]} \qquad \text{(A. 32)}
\end{aligned}
$$

Equations (A. 16), (A. 15) and the definition of $\mathbf{L}_{[k]}$ (A. 30) can be used to transform the expression of the measurement update (A. 16) in:

$$
\begin{aligned}
\hat{\mathbf{x}}_{[k|k]} &= \hat{\mathbf{x}}_{[k|k-1]} + \mathbf{L}_{[\mathbf{k}]}\left(\mathbf{d}_{[k]} - \mathbf{G}\hat{\mathbf{x}}_{[k|k-1]}\right) \\
&= \hat{\mathbf{x}}_{[k|k-1]} + \mathbf{K}_{[k]}\left(\mathbf{I} - \mathbf{J}\mathbf{M}_{[k]}\right)\left(\mathbf{d}_{[k]} - \mathbf{G}\hat{\mathbf{x}}_{[k|k-1]}\right) \\
&= \hat{\mathbf{x}}_{[k|k-1]} + \mathbf{K}_{[k]}\left(\mathbf{d}_{[k]} - \mathbf{G}\hat{\mathbf{x}}_{[k|k-1]} - \mathbf{J}\mathbf{M}_{[k]}\mathbf{d}_{[k]} + \mathbf{J}\mathbf{M}_{[k]}\mathbf{G}\hat{\mathbf{x}}_{[k|k-1]}\right) \\
&= \hat{\mathbf{x}}_{[k|k-1]} + \mathbf{K}_{[k]}\left(\mathbf{d}_{[k]} - \mathbf{G}\hat{\mathbf{x}}_{[k|k-1]} - \mathbf{J}\mathbf{M}_{[k]}\left(\mathbf{d}_{[k]} - \mathbf{G}\hat{\mathbf{x}}_{[k|k-1]}\right)\right) \\
&= \hat{\mathbf{x}}_{[k|k-1]} + \mathbf{K}_{[k]}\left(\mathbf{d}_{[k]} - \mathbf{G}\hat{\mathbf{x}}_{[k|k-1]} - \mathbf{J}\hat{\mathbf{p}}_{[k|k]}\right) \qquad \text{(A. 33)}
\end{aligned}
$$

Finally, by using the definition of $\mathbf{L}_{[k]}$ (A. 30) and equation (A. 28) in the previous obtained expression of $\mathbf{P}_{x[k|k]}$ gives:

$$
\begin{aligned}
\mathbf{P}_{x[k|k]} &= \mathbf{L}_{[k]}\tilde{\mathbf{R}}_{[k]}\mathbf{L}_{[k]}^{T} - \mathbf{L}_{[k]}\mathbf{G}\mathbf{P}_{x[k|k-1]} - \mathbf{P}_{x[k|k-1]}\mathbf{G}^{T}\mathbf{L}_{[k]}^{T} + \mathbf{P}_{x[k|k-1]} \\
&= \mathbf{K}_{[k]}\left(\mathbf{I} - \mathbf{J}\mathbf{M}_{[k]}\right)\tilde{\mathbf{R}}_{[k]}\left(\mathbf{K}_{[k]}\left(\mathbf{I} - \mathbf{J}\mathbf{M}_{[k]}\right)\right)^{T} - \mathbf{K}_{[k]}\left(\mathbf{I} - \mathbf{J}\mathbf{M}_{[k]}\right)\mathbf{G}\mathbf{P}_{x[k|k-1]} \\
&\quad - \mathbf{P}_{x[k|k-1]}\mathbf{G}^{T}\left(\mathbf{K}_{[k]}\left(\mathbf{I} - \mathbf{J}\mathbf{M}_{[k]}\right)\right)^{T} + \mathbf{P}_{x[k|k-1]} \\
&= \mathbf{K}_{[k]}\left(\tilde{\mathbf{R}}_{[k]} - \mathbf{J}\mathbf{M}_{[k]}\tilde{\mathbf{R}}_{[k]}\right)\left(\mathbf{I} - \mathbf{M}_{[k]}^{T}\mathbf{J}^{T}\right)\mathbf{K}_{[k]}^{T} - \cancel{\mathbf{K}_{[k]}\left(\mathbf{I} - \mathbf{J}\mathbf{M}_{[k]}\right)\mathbf{G}\mathbf{P}_{x[k|k-1]}} \\
&\quad - \cancel{\mathbf{P}_{x[k|k-1]}\mathbf{G}^{T}\left(\mathbf{K}_{[k]}\left(\mathbf{I} - \mathbf{J}\mathbf{M}_{[k]}\right)\right)^{T}} + \mathbf{P}_{x[k|k-1]} \\
&= \mathbf{P}_{x[k|k-1]} + \mathbf{K}_{[k]}\left(\tilde{\mathbf{R}}_{[k]} - \tilde{\mathbf{R}}_{[k]}\mathbf{M}_{[k]}^{T}\mathbf{J}^{T} - \mathbf{J}\mathbf{M}_{[k]}\tilde{\mathbf{R}}_{[k]} + \mathbf{J}\mathbf{M}_{[k]}\tilde{\mathbf{R}}_{[k]}\mathbf{M}_{[k]}^{T}\mathbf{J}^{T}\right)\mathbf{K}_{[k]}^{T} \\
&= \mathbf{P}_{x[k|k-1]} + \mathbf{K}_{[k]}\left(\tilde{\mathbf{R}}_{[k]} - \tilde{\mathbf{R}}_{[k]}\left(\mathbf{J}^{T}\right)_{[k]}^{-1}\mathbf{J}^{T} - \mathbf{J}\mathbf{J}_{[k]}^{-1}\tilde{\mathbf{R}}_{[k]} + \mathbf{J}\,\underbrace{\mathbf{J}_{[k]}^{-1}\tilde{\mathbf{R}}_{[k]}\left(\mathbf{J}^{T}\right)_{[k]}^{-1}}_{\left(\mathbf{J}^{T}\tilde{\mathbf{R}}_{[k]}^{-1}\mathbf{J}\right)^{-1}}\mathbf{J}^{T}\right)\mathbf{K}_{[k]}^{T} \\
&= \mathbf{P}_{x[k|k-1]} - \mathbf{K}_{[k]}\left(\tilde{\mathbf{R}}_{[k]} - \mathbf{J}\mathbf{P}_{p[k|k]}\mathbf{J}^{T}\right)\mathbf{K}_{[k]}^{T} \qquad \text{(A. 34)}
\end{aligned}
$$

Using equations (A. 18), (A. 19), (A. 27), (A. 28) and (A. 29), as well as the properties (A. 22) and (A. 23), the error covariance matrix $\mathbf{P}_{xp[k|k]}$ is given by:

$$
\begin{aligned}
\mathbf{P}_{xp[k|k]} &\equiv \mathbb{E}\left[\tilde{\mathbf{x}}_{[k|k]}\tilde{\mathbf{p}}_{[k|k]}^{T}\right] \\
&= \mathbb{E}\left[\left(\left(\mathbf{I} - \mathbf{L}_{[k]}\mathbf{G}\right)\tilde{\mathbf{x}}_{[k|k-1]} - \mathbf{L}_{[k]}\mathbf{v}_{[k]}\right)\left(-\mathbf{M}\mathbf{G}\tilde{\mathbf{x}}_{[k|k-1]} - \mathbf{M}\mathbf{v}_{[k]}\right)^{T}\right] \\
&= -\left(\mathbf{I} - \mathbf{L}_{[k]}\mathbf{G}\right)\mathbb{E}\left[\tilde{\mathbf{x}}_{[k|k-1]}\tilde{\mathbf{x}}_{[k|k-1]}^{T}\right]\mathbf{G}^{T}\mathbf{M}^{T} - \left(\mathbf{I} - \mathbf{L}_{[k]}\mathbf{G}\right)\underbrace{\mathbb{E}\left[\tilde{\mathbf{x}}_{[k|k-1]}\mathbf{v}_{[k}^{T}\right]}_{\mathbf{0}}\mathbf{M}^{T} \\
&\quad + \mathbf{L}_{[k]}\underbrace{\mathbb{E}\left[\mathbf{v}_{[k]}\tilde{\mathbf{x}}_{[k|k-1]}^{T}\right]}_{\mathbf{0}}\mathbf{G}^{T}\mathbf{M}^{T} + \mathbf{L}_{[k]}\mathbb{E}\left[\mathbf{v}_{[k]}\mathbf{v}_{[k]}^{T}\right]\mathbf{M}^{T} \\
&= -\left(\mathbf{I} - \mathbf{L}_{[k]}\mathbf{G}\right)\mathbf{P}_{x[k+1|k]}\mathbf{G}^{T}\mathbf{M}^{T} + \mathbf{L}_{[k]}\mathbf{R}\mathbf{M}^{T} \\
&= -\mathbf{P}_{x[k+1|k]}\mathbf{G}^{T}\mathbf{M}^{T} + \mathbf{L}_{[k]}\mathbf{G}\mathbf{P}_{x[k+1|k]}\mathbf{G}^{T}\mathbf{M}^{T} + \mathbf{L}_{[k]}\mathbf{R}\mathbf{M}^{T} \\
&= -\mathbf{P}_{x[k+1|k]}\mathbf{G}^{T}\mathbf{M}^{T} + \mathbf{L}_{[k]}\tilde{\mathbf{R}}_{[k]}\mathbf{M}^{T} \\
&= -\mathbf{K}_{[k]}\tilde{\mathbf{R}}_{[k]}\mathbf{M}^{T} + \mathbf{K}_{[k]}\left(\mathbf{I} - \mathbf{J}\mathbf{M}\right)\tilde{\mathbf{R}}_{[k]}\mathbf{M}^{T} \\
&= -\mathbf{K}_{[k]}\mathbf{J}\mathbf{M}\mathbf{M}^{T} \\
&= -\mathbf{K}_{[k]}\mathbf{J}\mathbf{P}_{p[k|k]} \qquad \text{(A. 35)}
\end{aligned}
$$

Summary

The first step 'Input estimation', is formed by equations (A. 27), (A. 29), (A. 15) and (A. 28). For the second step 'Measurement update', the equations (A. 31), (A. 33), (A. 34) and (A. 35) are used. The last step 'Time update', consists of equations (A. 14), (A. 32) and (A. 25)

Appendix B - Tension force in a parabolic cable

A brief summary of how to calculate the tension force in a parabolic cable is given here, for more information the reader may refer to [29]. As a reminder a cable can be assimilated to a parabola, in the case of an inextensible cable with a big L/d ratio (> 10) under a uniformly distributed load as its self-weight for example. Or in the case of an inextensible cable with an arbitrary L/d ratio, but an uniformly distributed load much higher than the cable's self-weight.

For a parabolic cable under uniformly distributed load p and whose supports are at the same level, as shown in figure 66.

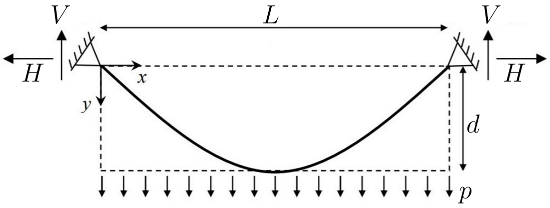

Figure 66: Scheme of a parabolic cable with supports at the same level (adapted from [29])

The horizontal support reaction can be obtained by the well-known formula:

$$H = \frac{pL^2}{8d} \tag{A. 36}$$

which is obtained by doing a rotation equilibrium relative to the lowest point on the cable (at midspan). L is the span of the cable and d is its deflection. Such that if the tension in the cable increases, its deflection decreases. Thus, it is impossible to have a perfectly straight cable, as according to equation A. 36 this would imply an infinite tension.

In this case, the vertical support reaction can easily be calculated by $V = \frac{pL}{2}$ and the tension force in the cable is equal to $T = \sqrt{H^2 + V^2}$.

In the situation, where the cable's supports are at different levels, as shown in figure 67 and as it is the case for the Geierlay footbridge, these equations need to be adapted.

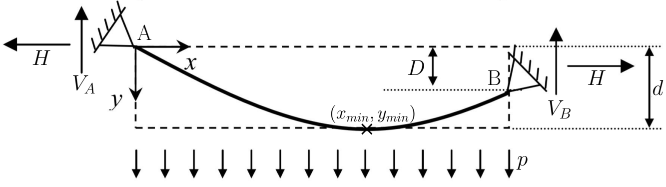

Figure 67: Scheme of a parabolic cable with supports at a level difference of D (adapted from [29])

The support reactions can be obtained by doing the three following equilibriums:

- Vertical equilibrium: $V_A + V_B = pL$
- Rotations equilibrium around A: $\frac{pL^2}{2} = HD + V_B L$
- Rotation equilibrium around the lowest point on the cable of coordinates (x_{min}, y_{min}): $\frac{px_{min}^2}{2} + Hd = V_A x_{min}$

Appendix C - Measured accelerations on the Geierlay footbridge

Three sets of measurements were carried out on the Geierlay footbridge in Germany. Four accelerometers were used and are here named a, b, c and d. Details about the experimental campaign are described in chapter 3.

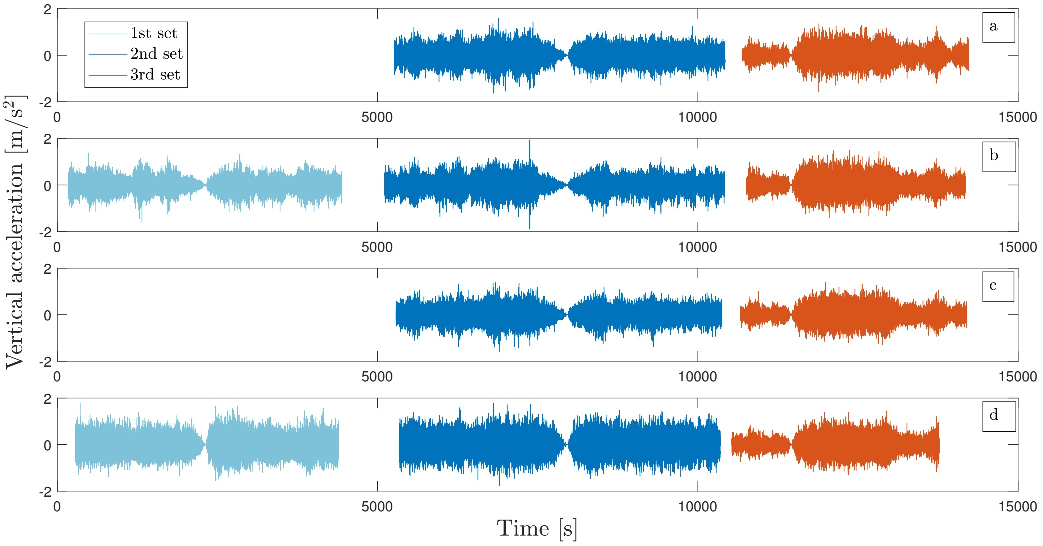

Figure 68: Vertical accelerations for the three sets and for the four sensors used

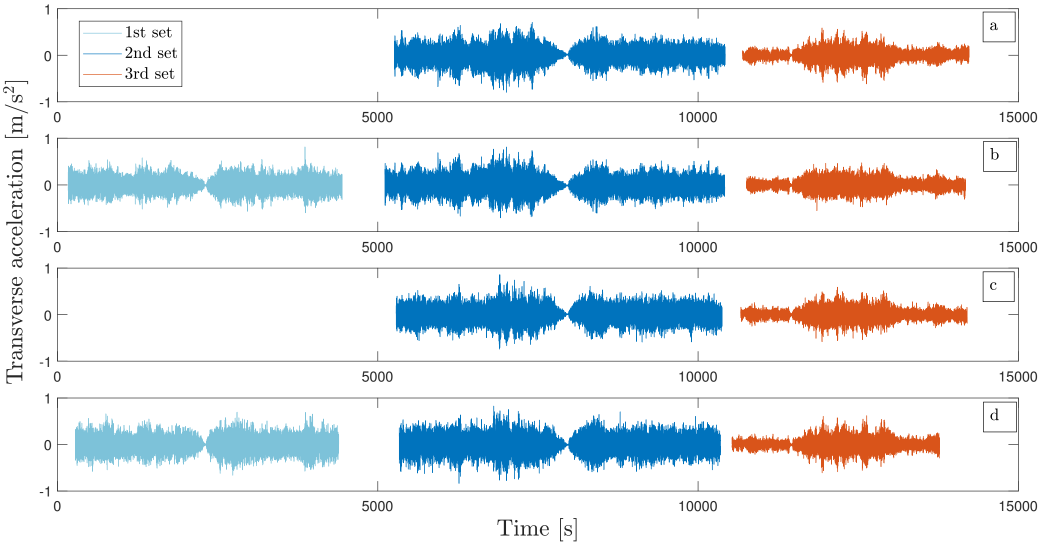

Figure 69: Transverse accelerations for the three sets and for the four sensors used

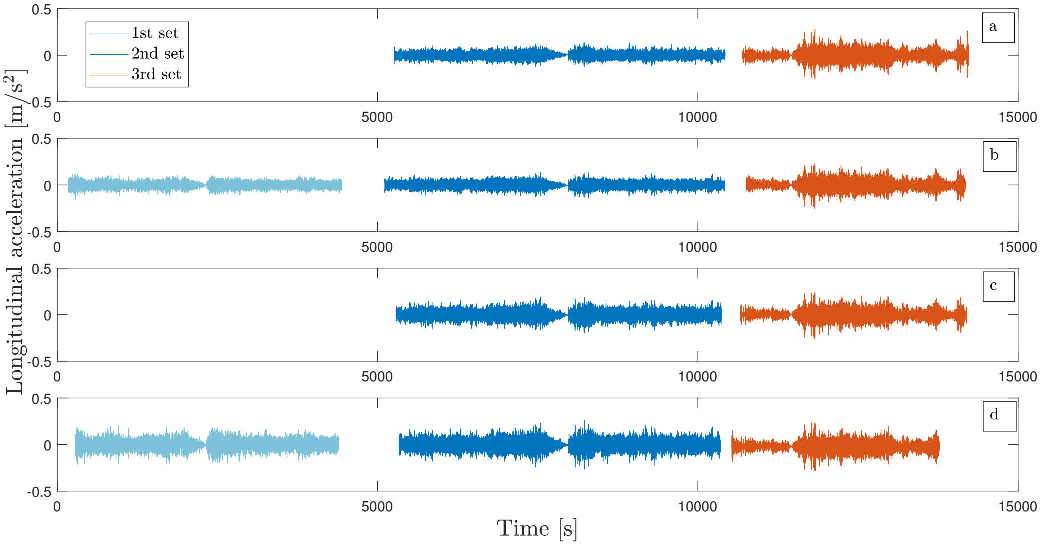

Figure 70: Longitudinal accelerations for the three sets and for the four sensors used

Appendix D - Mode shapes of the Geierlay footbridge

A model of the Geierlay footbridge has already been done in [42]. Here, the first mode shapes were simply extracted from the software *FinelG* used for the model. The various cables[5] from the walkway have been modelled by two equivalent cables. These have been calculated by following a similar procedure like the one in chapter 3 to find an equivalent single cable for the analytical identification of the natural frequencies. The wooden boards and the multiple lateral cables have been taken into account. The supports of the walkway prevent any translations in the three directions. Whereas only the rotations around the x and z-axis are blocked, allowing a rotation around the y-axis. The supports of the lateral parabolic cables are fully clamped. For more information, the reader may refer to [42]. In the following figures, the displacements have been scaled by a factor 25 for visualisation purposes.

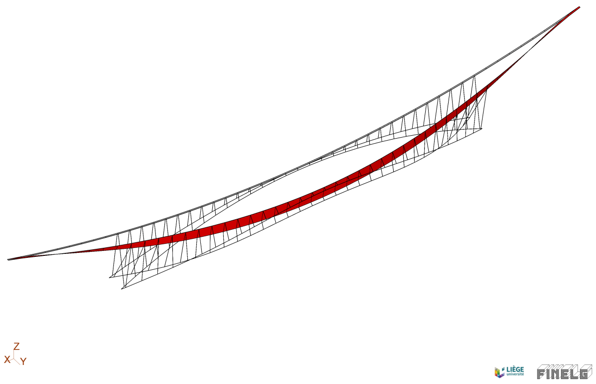

Figure 71: First mode shape at a frequency of 0.163Hz (|Disp. max|=1012mm, |Rot. max|=18.83°)

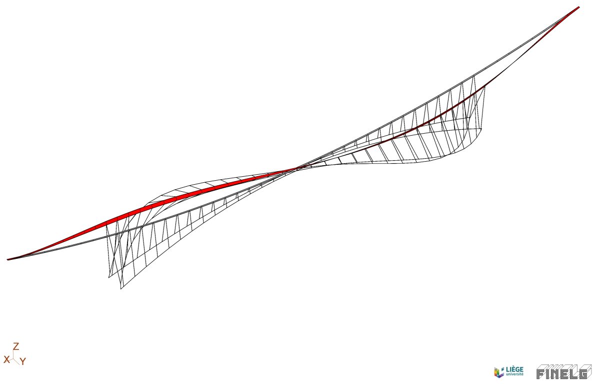

Figure 72: Second mode shape at a frequency of 0.239Hz (|Disp. max|=1008mm, |Rot. max|=5.28°)

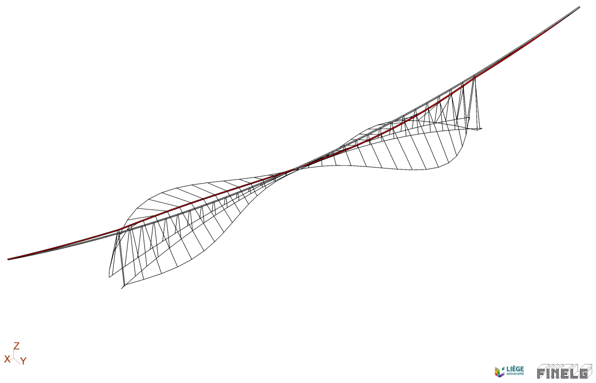

Figure 73: Third mode shape at a frequency of 0.289Hz (|Disp. max|=1056mm, |Rot. max|=0.23°)

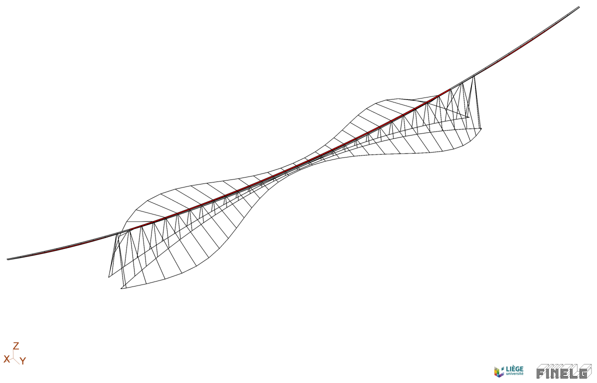

Figure 74: Fourth mode shape at a frequency of 0.290Hz (|Disp. max|=1017mm, |Rot. max|=0.06°)

---

[5] Cables 1, 2 and 3 shown in figure 5 from chapter 3.

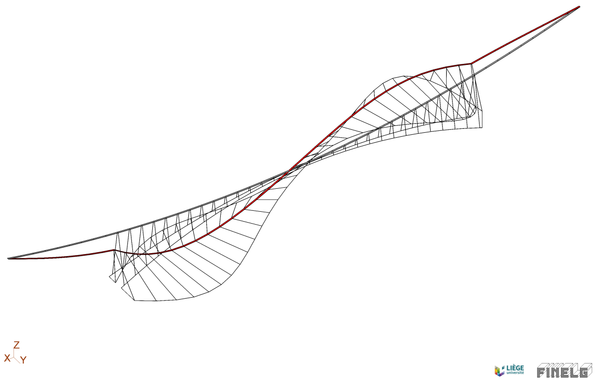

Figure 75: Fifth mode shape at a frequency of 0.312Hz (|Disp. max|=1265mm, |Rot. max|=1.06°)

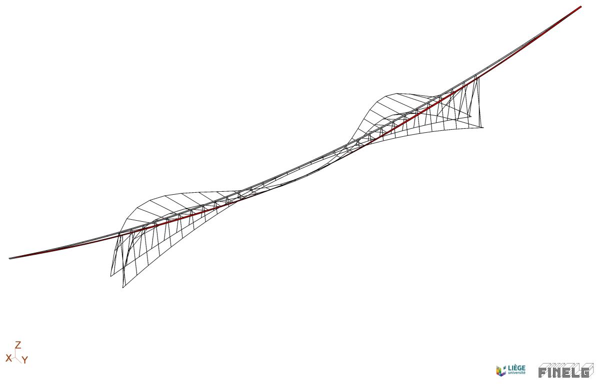

Figure 76: Sixth mode shape at a frequency of 0.323Hz (|Disp. max|=1017mm, |Rot. max|=1.93°)

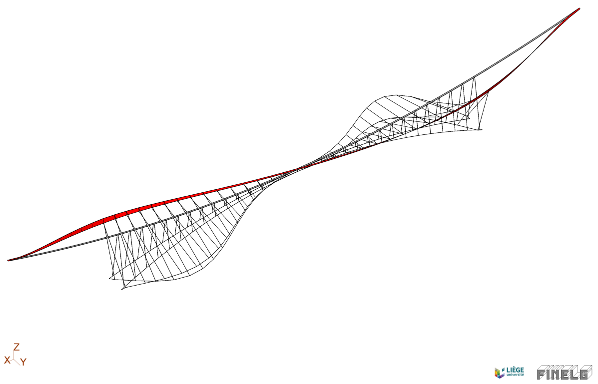

Figure 77: Seventh mode shape at a frequency of 0.352Hz (|Disp. max|=1022mm, |Rot. max|=6.84°)

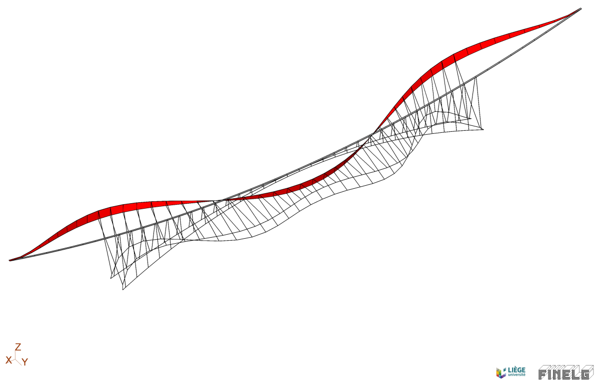

Figure 78: Eight mode shape at a frequency of 0.391Hz (|Disp. max|=1018mm, |Rot. max|=12.94°)

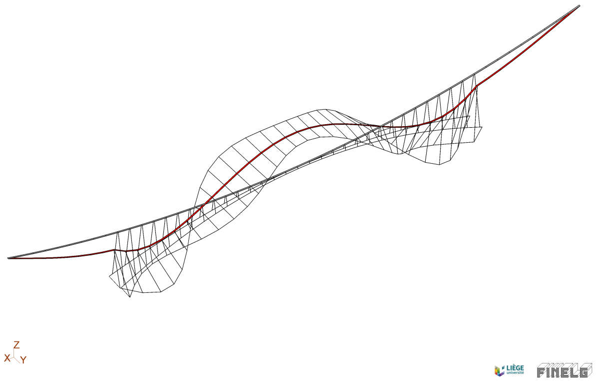

Figure 79: Ninth mode shape at a frequency of 0.443Hz (|Disp. max|=1065mm, |Rot. max|=1.39°)

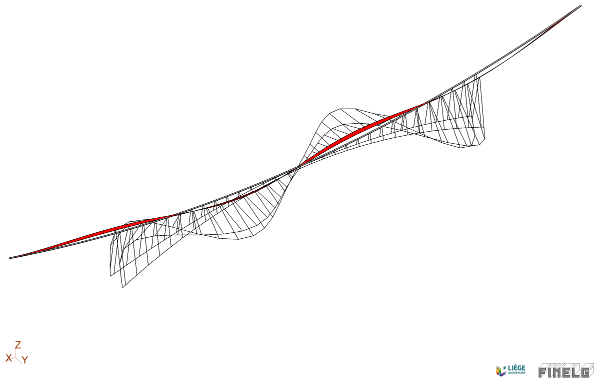

Figure 80: Tenth mode shape at a frequency of 0.461Hz (|Disp. max|=1015mm, |Rot. max|=4.97°)